Coding and Modulation for Wireless Communications with Application to Small Unit Operations [1]

Wayne Stark, Victor Cheng, Mike Chu, Tingfang Ji, Joe Kang, Paul Liang, Kurt Metzger, Do-Sik Yoo, Troy Nolan

January 26, 1999

[1]This work was supported in part by DARPA under grant SRA-588510732 and in part by the Army Research Office under grant DAAH04-96-1-0001.

Contents

1 Introduction, Motivation and Fundamental Limits

Spread-spectrum communication systems are well known for their ability to combat various sources of interference and multipath fading. In this section we demonstrate that spread-spectrum alone is actually not very good at defeating a worst-case pulsed or partial-band jammer. The performance of a spread-spectrum system (either direct-sequence or frequency-hopped) can be degraded by on the order of 30-40dB by a hostile and intelligent jammer. This severe loss in performance can be completely overcome with the appropriate use of error control coding.

In this section we will restrict our consideration to frequency-hopped spread-spectrum with partial-band interference. The case of direct-sequence with pulsed interference is the dual and similar results can be obtained. The block diagram of the transmitter and receiver are shown in Figure 1.

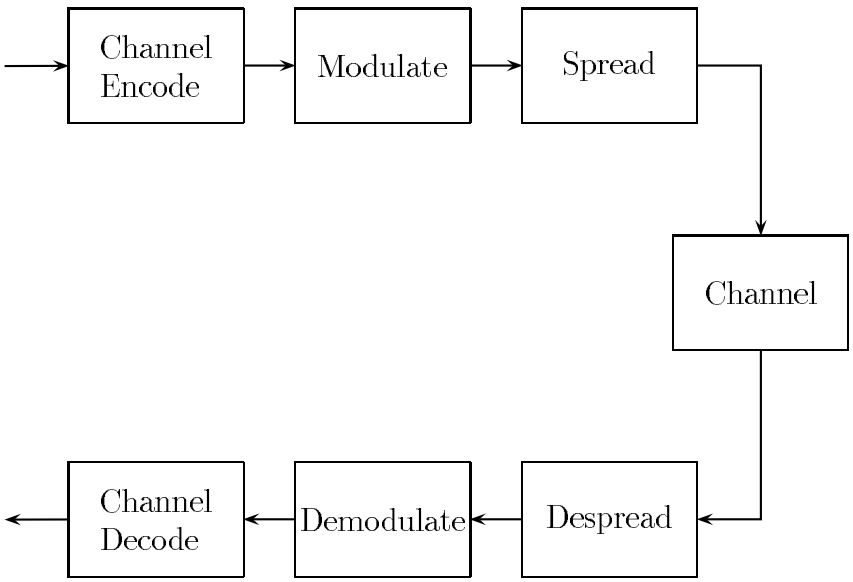

Figure 1: Transmitter and receiver block diagram

Consider a system with bandwidth W. This bandwidth is divided into q frequency slots as shown in Figure 2. The frequency slots or bins are nonoverlapping. We will assume the transmitter uses power P and modulates an R bit per second data stream using binary (orthogonal) FSK modulation. The energy per bit of information is $E_b = P/R$. The bandwidth needed is W/q which we will assume is equal to R. A jammer does not know which frequency slot or bin the communicator is using. As a result the jammer can have several strategies. The first strategy is to jam the whole bandwidth W that the transmitted signal is hopping over. We will assume that the jamming signal has no exploitable structure (like being a CW jammer). Jamming the whole bandwidth will

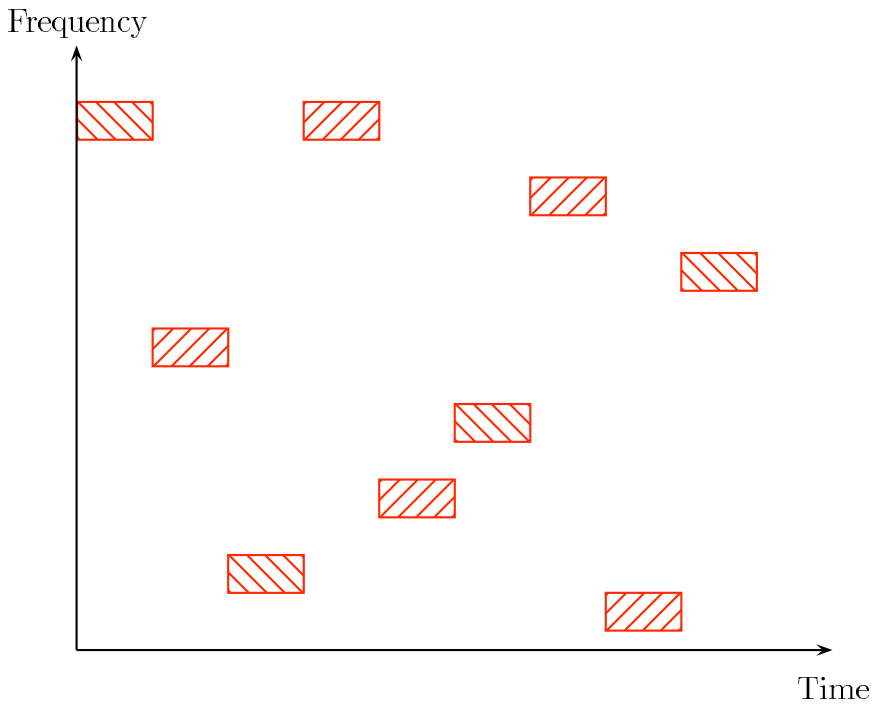

Figure 2: Time-frequency representation of frequency-hopped spread-spectrum

guarantee that some noise affects the transmitted signal no matter which frequency slot is being used. If the jammer has power J, then the power spectral density of the jammer will be $N_0/2 = J/(2W)$. This is the two-sided spectral density. It includes power at negative frequencies as well as positive frequencies. Thus $N_0 = J/W$. The bit error probability of binary FSK is given by

$$P_b = 0.5 \exp\{-E_b/2N_0\}. \tag{1}$$

This is an exponential decrease in error probability with signal-to-noise ratio E_b/N_0. To get bit error probability 10^{-5} requires 13.35dB for E_b/N_0. We can equivalently express this in terms of the ratio of transmitted power by the communicator and transmitted power by the jammer using the above relations, $E_b = P/R, N_0 = J/W$. Thus we can calculate the signal-to-noise ratio as

$$E_b/N_0 = (P/R)/(J/W) = (P/J)(W/R). \tag{2}$$

Since the ratio of bandwidth to data rate is equal to the processing gain (spreading factor) q we have that

$$E_b/N_0 = (P/J)(q). \tag{3}$$

Thus we immediately see improved performance (for fixed P/J) by spreading. This is quite obvious since a fraction $(q-1)/q$ of the jammer power is not falling into the

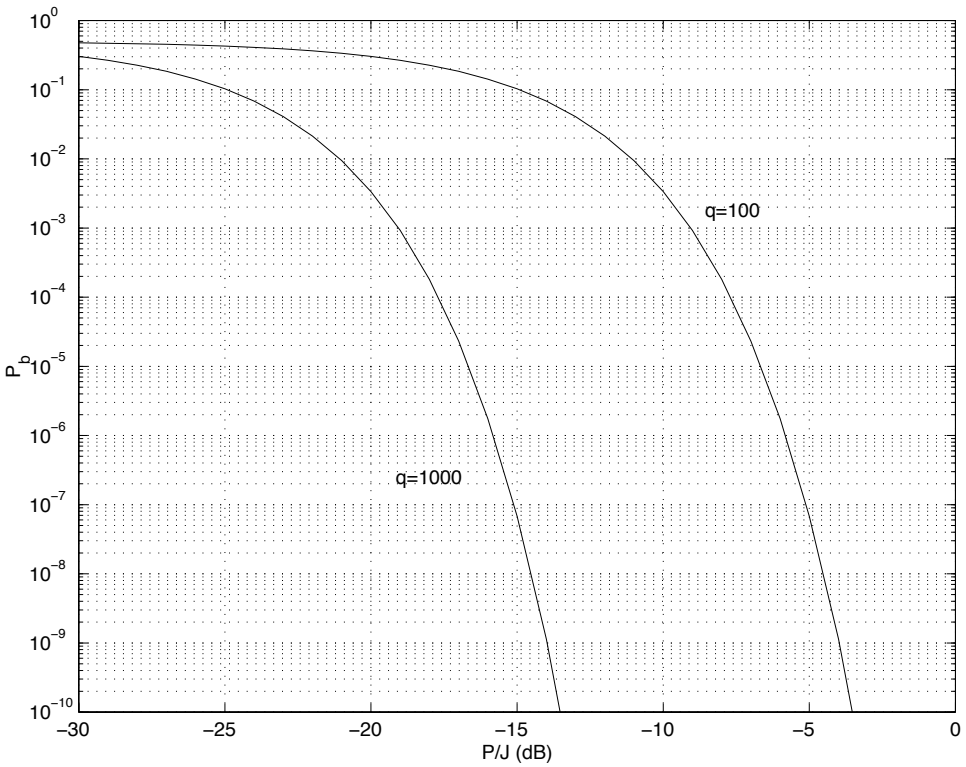

Figure 3: Error probability for full-band jamming

frequency slot used by the communicator. In fact only the fraction $1/q$ of the power is in the slot being used by the communicator and thus the effective jamming power is J/q. The error probability is thus

$$P_b = 0.5\exp\{-Pq/2J\}. \tag{4}$$

For the same bit error rate 10^{-5} with $q = 100$ we require a P/J=-6.65dB while for $q = 1000$ we require P/J=-16.65dB. The plot of error probability versus P/J for $q = 100$ and $q = 1000$ is shown below. It is clear that more spreading gives a gain of $10\log_{10}(q)$ dB in signal-to-noise ratio required for a given error probability. In Figure 3 the error probability for noncoherent demodulation of frequency-hopped binary FSK with full-band jamming is shown. Now consider an intelligent jammer. The jammer decides to jam only a fraction ρ of the slots where ρ is between 0 and 1. Thus the jammer's power is only spread over the bandwidth ρW. The rest of the bandwidth we will assume contains no interference or noise. The error probability is now calculated as follows. With probability ρ the error probability is $0.5\exp\{-(P\rho q)/2J\}$ while with probability $1-\rho$ the error probability is 0. Thus the average error probability is

$$P_b = \rho 0.5\exp\{-(P\rho q)/2J\} + (1-\rho)0.0 \tag{5}$$

$$P_b = \frac{\rho}{2}\exp\{-(P\rho q)/2J\}. \tag{6}$$

If now we look for the worst case partial-band jammer we need to maximize the right

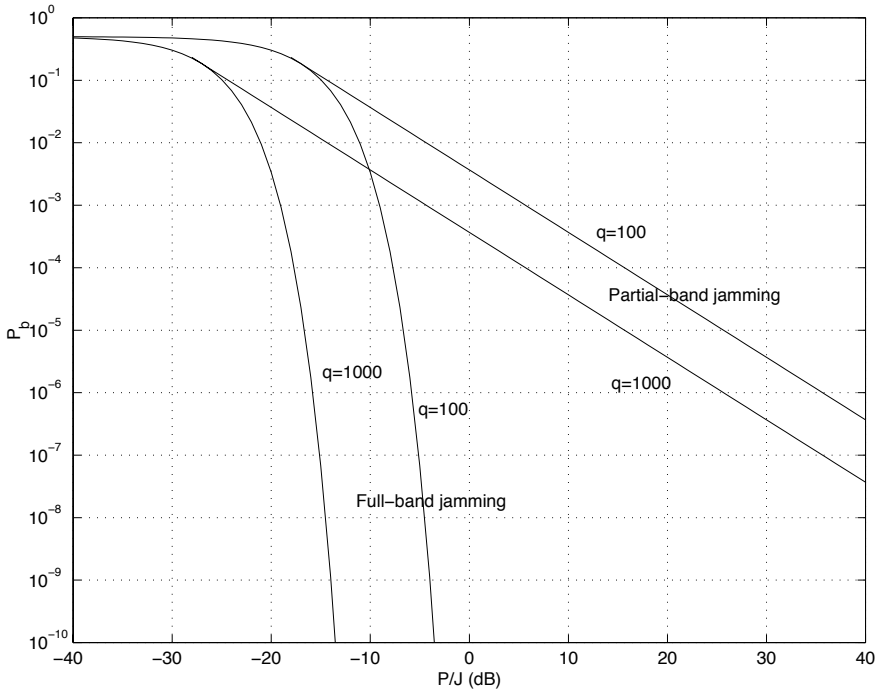

Figure 4: Error probability with worst-case partial-band jamming

q	Full-band Jamming	Worst-case partial-band jamming
100	-6.56	25.66
1000	-16.56	15.66
10000	-26.56	5.66

Table 1: P/J (dB) required for error probability 10^{-5} for different spreading factors in full-band and worst-case partial-band jamming.

hand side over the parameter ρ. This can be done easily with the following result.

$$P_b = \begin{cases} 0.5\exp\{-(Pq)/2J\} & Pq/J < 2 \\ e^{-1}/(Pq/J) & Pq/J > 2. \end{cases} \tag{7}$$

What this means is that for signal-to-noise ratio sufficiently high ($Pq/J > 2$) the error probability decreases inverse linear with signal-to-noise ratio. This is shown in Figure 4 for $q = 100$ and $q = 1000$. Now consider the P/J required for 10^{-5} error probability. For $q = 100$ we require P/J=25.66dB while for $q = 1000$ we require P/J =15.66 dB. Thus the worst case partial band jammer degrades performance relative to a full band jammer by 32.31dB for both $q = 100$ and $q = 1000$. This is a huge degradation in performance.

The conclusion is that worst-case jamming severely degrades performance of a frequency-hopped spread-spectrum communication system. Similar results apply to direct-sequence

spread-spectrum with pulsed interference. As a result a huge processing gain is required to obtain reasonable performance results. To get back to the results for $q = 100$ with full band jamming we would need to increase the processing gain by more than 22dB or by a factor of 166 (that is we would need to have q=16600).

Fortunately, there is an alternative method of recovering from the huge loss in performance without the need to spread the signal of such huge bandwidths. The method involves the use of error control coding. Error control coding works as follows in a partial-band interference environment. First the information bits are encoded and redundant bits are added. From a certain subset of the information bits and redundant bits the actual information bits can be determined. As a simple example suppose the encoder repeats each information bit three times and transmits these bits over different frequencies. Assume, for the sake of argument that the decoder knows which bits were interfered with and which were not interfered with. In order for the decoder to make an error all three of the bits must be interfered with. If one of them is not and the decoder knows it, as we have assumed, then the decoder can determine the transmitted information perfectly. Thus we are forcing the jammer to spread his signal over much of the bandwidth in order to guarantee that the information and redundant bits are interfered with. Notice that we are effectively using three times the bandwidth with this scheme because there each information bit is transmitted three times over different frequencies in the time duration of one data bit. So we can think that our overall spreading is $3q$ rather than q. With such a modest increase in the spreading factor (compared to an increase by a factor of 166) we can show a very large improvement in performance.

There are many different coding strategies that can be employed to counteract the effect of a partial-band jammer. It would be nice to know the fundamental limit on performance possible for the worst-case jammer with the best possible code and decoding algorithm. Fortunately this can be done using the fundamental results in information theory. Given a certain spreading factor and given a code rate r (information bits/coded bit) we would like to know what is the minimal ratio of P/J required for small error probability. This has been computed for various modulation schemes including binary FSK. In Figure 5 the minimum value for $E_b/N_0 = Pq/Jr$ needed for reliable communication as a function of the code rate r is shown. The lower curve in Figure 5 is the minimum E_b/N_0 needed for a full-band jammer. The upper curve is the minimum E_b/N_0 needed for a worst-case partial-band jammer. As can be seen below rate 0.5 the two curves coincide. This indicates that the worst-case jammer at code rates below 0.5 is the same as a full-band jammer. That is, the optimum jamming strategy is to spread the jamming power over the full bandwidth of the spread-spectrum signal. The minimum E_b/N_0 required for reliable communications (arbitrarily small error probability) is 6.71dB when using binary FSK with noncoherent detection. This occurs with a code rate of about 0.5 . Thus we require $P/J(q/r)$=6.71dB. If we have spreading by a factor of 50 (so that the overall spreading is q/r=100) then the P/J required is 13.29dB. This is compared to 25.66dB for an uncoded system with the same ratio of bandwidth to data rate. Thus optimal coding has bought us about 39dB improved performance. If we think of the received power decreasing as the fourth power of the distance (as it would in the case of a ground wave) then the gain is more than a factor of 9.4 in increased distance. If the propagation

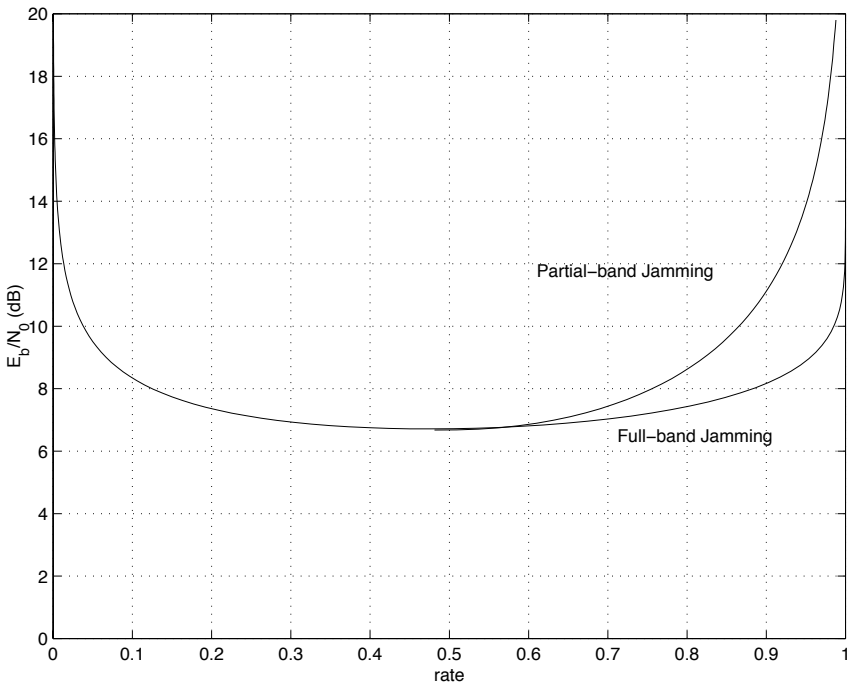

Figure 5: Minimum signal-to-noise necessary for reliable communication vs. code rate

causes the power to decrease as the second power of the distance (as it would for free space propagation) then the increase range is a factor 88. This gain is without sacrifice in data rate or bandwidth. The disadvantage is the increased complexity in the receiver and the potentially large delay required.

In Table 2 we show the required signal-to-noise ratio for error probability 10^{-5} for no coding and the corresponding signal-to-noise ratio for arbitrarily small error probability with coding. Notice that the worst-case partial-band jammer does not degrade the system performance relative to a full-band jammer since the code rate is 1/2. If we had used a higher code rate there would have been a slight degradation in performance.

In Figure 6 the minimum required signal-to-noise ratio for reliable communication is shown for coherent reception of BPSK. As in the noncoherent case there is a code rate below which the optimum jamming strategy is to jam the whole band. Unlike BFSK with noncoherent reception the optimal code rate is as small as possible with the minimum signal-to-noise ratio approaching -1.59dB.

Now consider what happens with binary frequency shift keying in a Rayleigh faded environment. Rayleigh fading occurs because of multiple paths between the transmitter and receiver. These multiple paths can either add constructively or add destructively. If the symbol duration is relatively long the different paths will have approximately the same delay (relative to the symbol duration) and will not cause any intersymbol interference. The received signal in this case is just the transmitted signal but with a Rayleigh distributed amplitude. For noncoherent demodulation the bit error probability is given

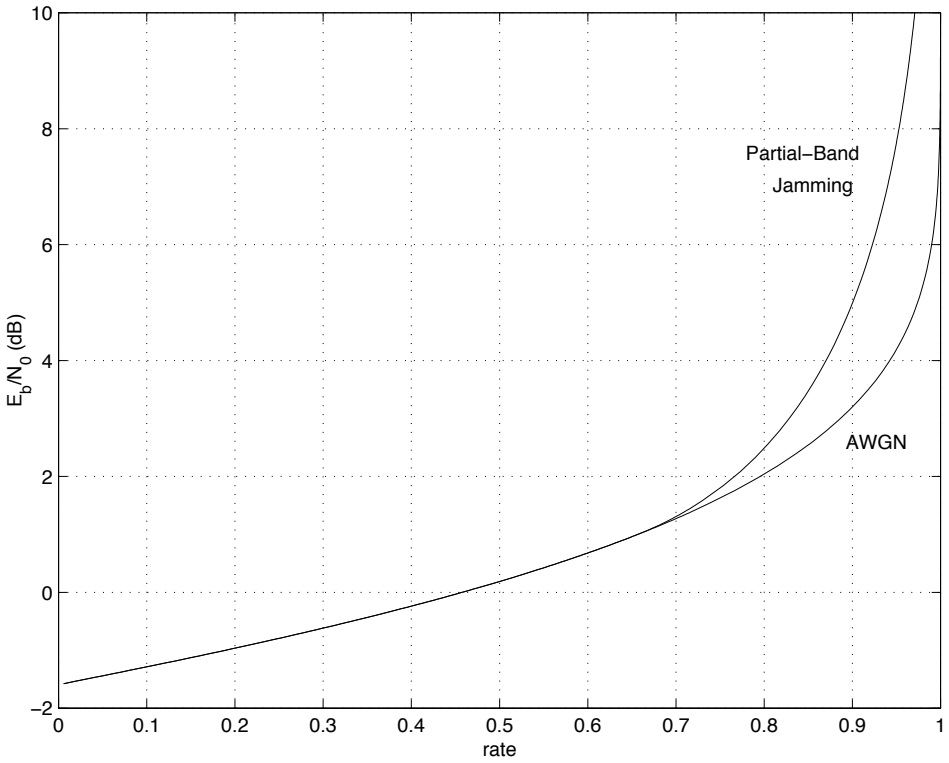

Figure 6: Minimum signal-to-noise ratio for coherent BPSK for worst-case partial-band jamming and full-band jamming

q	Code Rate	Full-band jamming	Worst-case partial-band jamming
100	$r = 1$ (no coding)	- 6.56	25.66
1000	$r = 1$ no coding	-16.56	15.66
10000	$r = 1$ (no coding)	-26.56	5.66
50	$r = 1/2$ (no coding)	-13.29	-13.29
500	$r = 1/2$ no coding	-23.29	-23.29
5000	$r = 1/2$ (no coding)	-33.29	-33.29

Table 2: P/J (dB) required for error probability 10^{-5} for different spreading factors in full-band and worst-case partial-band jamming with and without coding.

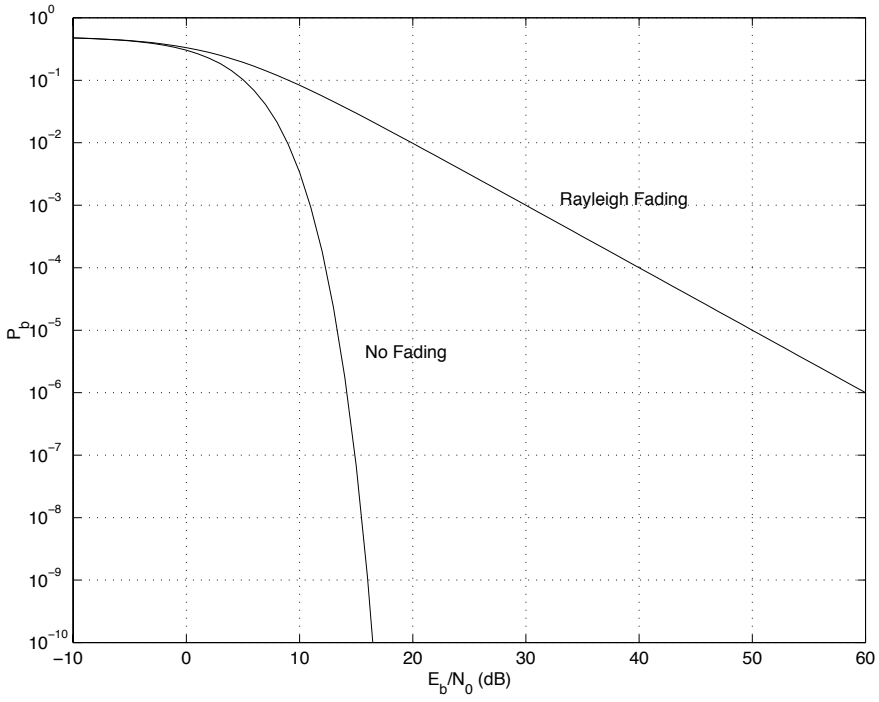

Figure 7: Error probability for noncoherent reception of BFSK in Rayleigh fading

by

$$P_b = \frac{1}{2 + E_b/N_0}. \tag{8}$$

This is plotted in Figure 7. As can be seen in the plot below the error probability decreases only inverse linearly with signal-to-noise ratio. This results in a loss in performance of 30-40dB.

One simple method to overcome this huge loss in performance is to use error control coding with frequency hopping. As a simple example consider transmitting the same information symbol three times on three different frequency hops. If we assume the frequencies are separated by more than the coherence bandwidth of the channel then the amplitude of the received signal on the different hops is independent. As such, it is unlikely that the signal will be severely attenuated on all three hops simultaneously. Thus the probability of error will be significantly improved compared to sending the information once on a single hop. There are many different codes that can be used to overcome Rayleigh fading. It would be nice to know the fundamental limit on performance with the best possible code. Fortunately this can be done using information theory. In Figure 8 we plot the minimum signal-to-noise ratio needed for reliable communication as a function of the rate of the code with Rayleigh with different assumptions about the information available and different types of decoder processing. As can be seen with the best codes the minimum signal-to-noise ratio needed is 7.37dB for Rayleigh fading with

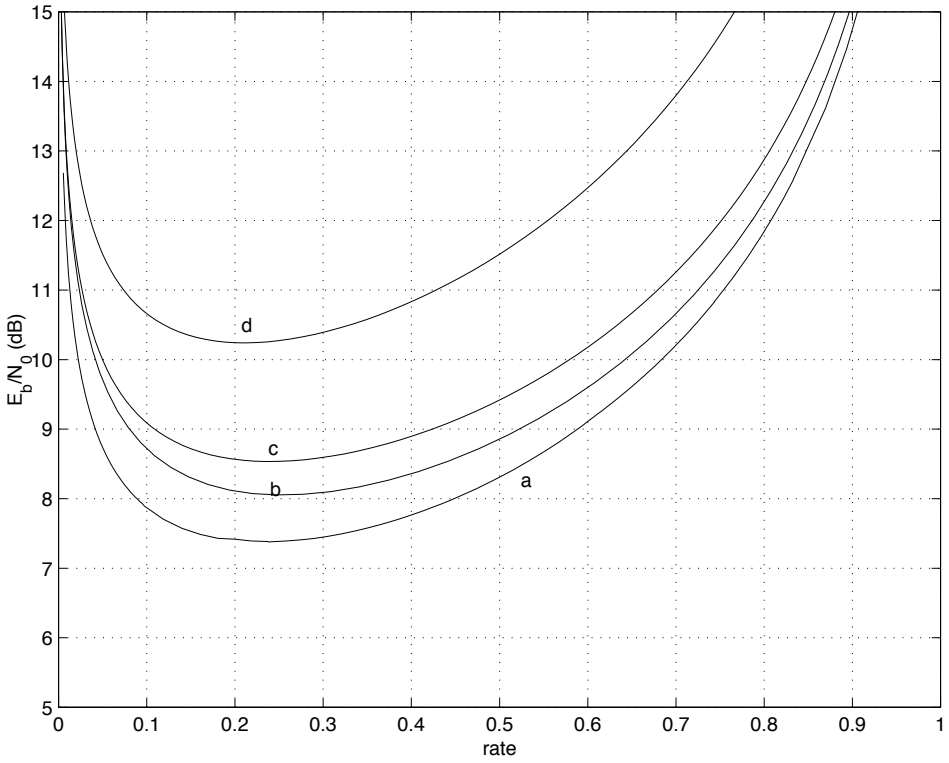

Figure 8: Minimum signal-to-noise ratio necessary for reliable communication using BFSK with noncoherent reception in Rayleigh fading; a: soft decisions, side information available, b: soft decisions, no side information, c: hard decisions side information available, d: hard decisions, no side information.

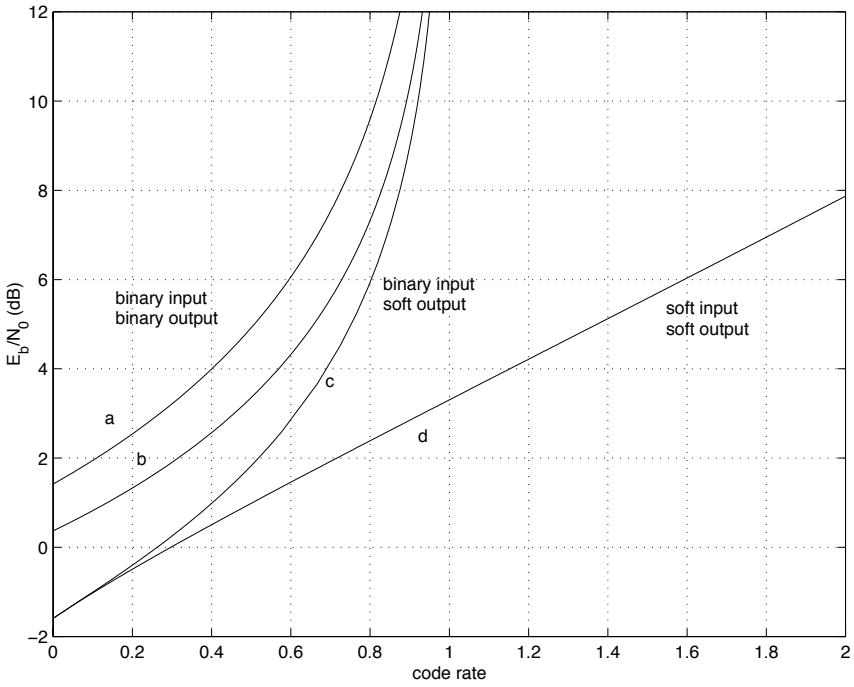

Figure 9: Minimum signal-to-noise ratio necessary for reliable communication using BPSK with coherent reception in Rayleigh fading; a: hard decisions, no side information, b: hard decisions, side information available, c: soft decisions, side information available, d: soft decisions, side information available, optimum input signal.

side information and soft decision processing. For no fading the minimum signal-to-noise ratio needed is 6.71dB. Thus the fundamental loss in performance due to Rayleigh fading is only about a 0.7dB compared to the 30-45dB loss in performance without coding. For coherent reception we show similar curves in Figure 9.

The conclusion of the above is that a well designed spread-spectrum communication system which must operate in either a jamming or fading environment must employ some form of coding to gain back the huge loss due to an intelligent (partial-band, unstructured) jammer or due to Rayleigh fading. While the discussion here has been for frequency-hop spread-spectrum similar arguments can be made for direct-sequence spread-spectrum.

Now that the fundamental limit on performance with the best possible codes (independent of complexity and processing power required) has been determined the research question becomes, how do we find codes that achieve performance close to the optimum with minimum complexity? There are many other issues that need to be considered as well. One important issue not addressed above is the channel propagation model. In a wireless environment there will time-selective, frequency-selective and space-selective fading. Selectivity offers possible advantages. The advantage with selectivity is that the whole signal is not deeply faded all the time at all antennas. As such we can average out the deep fades due to destructive interference with the situation where the fade is due to

constructive interference. This type of fading needs additional processing in order to take advantage of the selectivity. Another issue is coherent demodulation versus noncoherent demodulation. Clearly larger gains are possible with coherent demodulation compared to noncoherent demodulation. Antenna diversity is another issue. Again, larger gains are possible with multiple antennas versus a single antenna.

When multipath fading and/or partial-band interference occurs there are various issues that need to be addressed in designing a coded-modulation scheme. These include whether the receiver has estimates of the channel (faded level, jamming level) or not. Another issue is the memory of the channel. Memory can be exploited by the receiver by employing estimation schemes that allow us to determine channel parameters. Other important parameters when designing a coded-modulation scheme include delay required, packet or bit error rate desired, complexity of decoding algorithm, time variation of the channel. These issues apply to both direct-sequence spread-spectrum systems and frequency-hop spread-spectrum systems. Another issue has to do with the transmitted signal. We would like the signal to occupy the smallest possible bandwidth and require minimal energy to transmit a signal with a given power. This implies that a power efficient amplifier is important. Power efficient amplification usually is done by driving an amplifier into saturation. This may cause the signal to be distorted and may generate sidebands outside the frequency band the signal is supposed to occupy. The distortion and sideband generation increases if the envelope of the signal is not constant. Thus constant envelope signaling is important in minimizing the amount of energy consumed at the transmitter. However, constant envelope signals general require more bandwidth than nonconstant envelope signals. Thus very careful design is necessary when trying to minimize the consumed power.

2 Channel Models

The performance of environment, transmitted signals are especially prone to attenuation, distortion, and interference by the time they arrive at the desired receiver. Although many of these channel characteristics are unpredictable, they can often be accurately modeled using statistical methods.

A communication system is highly dependent upon the channel characteristics. In a mobile communication In this section we discuss various types of fading and interference that occur in a mobile communication environment. Channel fading can be classified into three types: path loss, shadowing and fast fading. We first give brief descriptions of the basic propagation mechanisms of reflection, diffraction, and scattering, followed by detailed descriptions of the statistical models. Finally, we introduce our channel simulation process.

2.1 Fading

The two main effects of fading are signal distortion and attenuation. In free space, the signal power decays with distance as $1/d^2$. However, in actual radio communication environments, there are various scatterers and reflectors such as buildings and trees, which may result in severe signal distortion and attenuation. The presence of various scatterers and reflectors also makes the received signal amplitude fluctuate very rapidly as the radio moves. Because of this uncertainty, we generally describe the signal fluctuations using statistical models. Usually, we deal with the effect of fading using three concepts: large scale path loss, shadowing, and multi-path fading.

2.1.1 Basic Propagation Mechanisms

If both the transmitter and receiver are located in free space, the received power P_r is given by

$$P_r = \frac{P_t G_t G_r \lambda^2}{(4\pi)^2 d^2 L} \tag{9}$$

where P_t is the transmitted power, G_t the transmitter antenna gain, G_r the receiver antenna gain, d the distance between the transmitter and the receiver in meters, L the system losses ($L > 1$), and λ the wavelength in meters. Hence the received signal is inversely proportional to the square of the distance in free space propagation.

However, in the practical situations, the terrain effects and the presence of radio-wave scatterers along the path further affect the received signal strength. Variations in the contour and roughness of the terrain, including any scatterers present, cause changes in propagation loss as the result of reflection, scattering and diffraction.

A. Reflection

When electromagnetic wave propagating in one medium impinges upon another medium having a different dielectric constant, permeability, or conductivity, the wave is partially

Material	Permittivity ε_r	Conductivity $\sigma(s/m)$
Poor Ground	4	0.001
Typical Ground	15	0.005
Good Ground	25	0.02
Sea Water	81	5.0
Fresh Water	81	0.01

Table 3: Permittivity and conductivit of typical terrestrial materials

reflected and partially transmitted. For the case of a plane wave in air incident normally on a perfect conductor, the wave is completely reflected without loss of energy as can be seen from the case of a perfect mirror. The ratio, called the reflection coefficient, of the electric field intensity of the reflected wave to that of the incident wave from the free space is given by the Fresnel formulas:

$$\frac{E_{hr}}{E_{hi}} = \frac{\sin\theta_i - \sqrt{(\varepsilon_r - j\frac{\sigma}{2\pi f_c \varepsilon_o}) - \cos^2\theta_i}}{\sin\theta_i + \sqrt{(\varepsilon_r - j\frac{\sigma}{2\pi f_c \varepsilon_o}) - \cos^2\theta_i}} \tag{10}$$

and

$$\frac{E_{vr}}{E_{vi}} = \frac{(\varepsilon_r - j\frac{\sigma}{2\pi f_c \varepsilon_0})\sin\theta_i - \sqrt{(\varepsilon_r - j\frac{\sigma}{2\pi f_c \varepsilon_0}) - \cos^2\theta_i}}{(\varepsilon_r - j\frac{\sigma}{2\pi f_c \varepsilon_0})\sin\theta_i + \sqrt{(\varepsilon_r - j\frac{\sigma}{2\pi f_c \varepsilon_0}) - \cos^2\theta_i}} \tag{11}$$

where $E_{vr}(E_{hr})$ is the vertical (horizontal) component of the electric field of the reflected wave, $E_{vi}(E_{hi})$ the vertical (horizontal) component of the electric field of the incident wave, ε_r the relative permittivity of the second medium, ε_o the electric permittivity of the vacuum, σ the conductivity of the second medium, f_c the frequency of the electromagnetic wave, θ_i the angle between the incident wave and the interface. Some typical values of ε_r and σ for some terrestrial materials are tabulated in Table 3. From the Fresnel formulas, we see that the ratios are close to -1 when θ_i is very small, which implies that the reflected electric field has almost the same amplitude but opposite phase compared to the incident electric field, when θ_i is very small.

B. Diffraction

Diffraction around the earth's curvature makes it possible to transmit radio signals beyond the line of sight and allows an electromagnetic wave to propagate beyond an obstruction. Although the field strength decreases rapidly as one moves deeper into the shadowed region, the field may be still finite and have sufficient strength to be useful. The phenomenon of diffraction can be easily explained using Huygen's principle, which states that all points on a wavefront can be considered as point sources for the production of secondary wavelets, and that these wavelets combine to produce a new wavefront in the

direction of propagation. Diffraction is caused by the propagation of secondary wavelets into the shadowed region.

On a propagation path dominated by a single prominent mountain or building, the received field strength is usually computed by use of the classical knife-edge diffraction theory of optics. The field strength at a point in the shadowed region, called the diffraction zone, is the vector sum of the fields due to all of the secondary Huygen sources in the plane above the knife-edge. The field strength E_d of a knife-edge-diffracted wave is given by

$$E_d = E_0 F(v) = E_0 \frac{1+j}{2} \int_v^\infty \exp(-j\frac{\pi t^2}{2})\, dt \tag{12}$$

where E_0 is the free space field strength in the absence of the knife edge and v is defined by

$$v = h\sqrt{\frac{2(d_1+d_2)}{\lambda d_1 d_2}} \tag{13}$$

with d_1 and d_2 the distances of the knife edge from the transmitter and the receiver, h the height of the knife edge and λ the wavelength of the wave. The function $F(v)$ is the complex Fresnel integral. However, in most cases of practical interest, one must consider not only the direct ray from transmitter to receiver via knife-edge, but also the rays that are reflected from the ground on either or both sides of the knife-edge.

Some examples of diffraction loss combined with propagation loss are tabulated in Table 4. We assumed the hill is smooth and the propagation loss follows the $1/d^4$ law. Antenna height is assumed to be 2m for both the receiver and the transmitter. We see that with higher frequency the loss is larger. And as the receiver moves toward the obstacle, we have more diffraction loss.

C. Scattering

The measured path loss in a mobile radio environment is often less than what is predicted by reflection and diffraction only. This is because when a radio wave impinges on a rough surface, the reflected energy is spread out (diffused) in all directions due to scattering. To test the roughness of a surface, let's define a critical height h_c by

$$h_c = \frac{\lambda}{8\cos\theta_i} \tag{14}$$

where θ_i is the angle of incidence as defined previously. Hence the critical height depends on the angle of incident. A surface is considered smooth if its minimum to maximum proturbance h is less than h_c and is considered rough otherwise. This is called the Rayleigh criterion.

For rough surfaces, the reflection coefficients need to be modified by multiplying a scattering loss factor ρ_s to account for the diminished reflected field. Ament, 1953, derived the formula

$$\rho_s = \exp[-8(\frac{\pi\sigma_h \cos\theta_i}{\lambda})^2] \tag{15}$$

f_c (MHz)	$D_T(km)$	$D_R(km)$	$h(m)$	Total Loss (dB)
38	1	1	30	141.3
38	1.9	0.1	30	146.6
38	1	1	100	150
910	1	1	30	180.4
910	1.9	0.1	30	187.6
910	1	1	100	191.3

f_c : Frequency of the signal transmitted;
D_T : Distance between transmitter and obstacle;
D_R : Distance between receiver and obstacle;
h : the height of the obstacle;
Total Loss = Transmitted Power/Received Power in dB

Table 4: Examples of Some Diffraction and Propagation Loss

which was modified by Boithias, 1987, to

$$\rho_s = \exp[-8(\frac{\pi\sigma_h \cos\theta_i}{\lambda})^2] I_o[8(\frac{\pi\sigma_h \cos\theta_i}{\lambda})^2] \tag{16}$$

where σ_h is the standard deviation of the surface height about the mean surface height and I_o is the zeroth order modified Bessel function of the first kind.

Radio waves are scattered by objects such as trees, lampposts, and moving vehicles that have dimensions comparable to the wavelength. For urban mobile radio systems, models based on the bistatic radar equation may be used to predict the scattering losses in the far field. The bistatic radar equation, as given by Skolnik, is

$$P_r = \frac{P_t G_t G_r \lambda^2 \sigma_b}{(4\pi)^3 d_T^2 d_R^2 L_p(t) L_p(r) L_s} \tag{17}$$

where

P_r = received Power $[w]$
P_t = transmitter Power $[w]$
G_t = transmitting-antenna gain in direction of target
G_r = receiving-antenna gain in direction of target
σ_b = bistatic cross section $[m^2]$
d_T = transmitter-to-target distance $[m]$
d_R = receiver-to-target distance $[m]$
$L_p(t)$ = propagation loss over transmitter-to-target path
L_p = propagation loss over receiver-to-target path
L_s = system loss
λ = wavelength $[m]$.

2.1.2 Statistical Description

The propagation loss can be predicted in principle by considering all of the above three mechanisms of propagation, namely, reflection, diffraction and scattering, given enough information about the topographical situations. The sufficiency of the information is dependent both on the complexity of terrain structure and the heights of the antennas. Combining empirical and analytical methods, we can reduce the requirement of computations. However, in the mobile radio environments, the receivers not only have low antenna height but also change their locations, which result in rapid fluctuations in the received field strength. So statistical methods are particularly required for the prediction of the propagation loss in the mobile environments.

The large-scale path loss is defined to be the average path loss over an area of radius of a few hundreds times of wavelengths. In this path loss that is called the area mean, the effects of detailed terrain structure in the immediate vicinity of the receiver is removed. The Longley-Rice model and Okumura model are among the most popular ones in the prediction of the large-scale path loss. While the Okumura model is known to be suitable for the urban and suburban areas, the Longley-Rice model is more accurate for the rural areas.

In actual radio communication environments, received field strength generally fluctuate very rapidly as the receiver moves from one place to another separated by a distance of the order of the wavelength of the transmitted signal. So we usually employ a statistical method to describe the situations. First we consider the local mean which is defined as the signal strength averaged over a distance of a few tens of wave length, typically 40 wavelengths. The fluctuation from this local mean is called the multi-path or fast fading effect. In general, this fast fading effect is modeled by wide-sense stationary uncorrelated complex Gaussian scattering (WSSUS) model[1].

In the local mean, the effect of fast fading is removed. However, as the experiments reported by Egli in 1957, for paths longer than a few hundred meters, the local-mean power fluctuates with a 'log-normal' distribution about the area-mean power. This medium scale effect is called shadowing because it is due to the presence of the topographical situations in the vicinity of the antennas. The correlation of the received amplitudes as a function of time depends on the velocity of the radio but is generally on the order of seconds or longer. In a cellular environment the shadowing and the path loss are dealt with by using power control techniques, increasing the power when the signal amplitude drops and decreasing the power when the signal amplitude increases. This implies the use of feedback to determine power levels. It also implies relatively slow time variations so that the feedback takes effect before the propagation changes.

In summary, the received signal is modeled to fluctuate statistically from the local mean, which is also assumed to fluctuate statistically from the large sale path loss.

A. Large-scale Propagation Loss

There have been various efforts to find efficient and accurate ways to predict large-scale propagation loss. Usually, both analytical and empirical methods are used. Empirical data are useful for reducing computational requirements as well as increasing the accuracy of

Environment	Path Loss Exponent, n
Free-Space	2
Urban Area Celluar Radio	2.7 - 4
Shadowed Urban Cellular Radio	5 - 6
In Building Line of Sight	1.6 - 1.8
Obstructed in Building	4 - 6
Obstructed in Factories	2 - 3

Table 5: Typical Path Loss Exponents for Various Environments

the predictions. For example, the large-scale propagation loss over seawater is vastly different from that over a rural forested area. Empirical data give comparisons for those losses and allow us to apply the results to similar situations. However, the validity of empirical models at certain frequencies and environments other than those used to derive the models can only be established by verifying them against data from those specific frequencies and environments. On the other hand, models based solely on analytical tools demand computational complexity that often exceeds practicality. Therefore, most of the propagation models for large-scale propagation loss are at least partially empirical. In the following we briefly describe some of the most popular models.

a) Log-Distance Path Loss Model

As indicated previously, average received signal power decreases with distance raised to some exponent. In the log-distance path loss model, the average path loss $PL(d)$ for transmitter and receiver with separation d is expressed as a function of d through a path loss exponent n as

$$PL(d) \propto (\frac{d}{d_0})^n \tag{18}$$

where d_0 is the free space close-in distance, and n is the path loss exponent that indicates the rate at which the path loss increases with distance. The value of n depends on the terrain structure, with some typical values given in Table 5.

b) Longley-Rice Model

One of the most well-known models for propagation loss prediction is the Longley-Rice model[2], applicable for point to point communication systems in the frequency range from 40 to 100 MHz and over various types of terrain. The median transmission loss is predicted using the path geometry of the terrain profile and the refractivity of the troposphere. A two-ray ground reflection model is used to predict signal strengths within the radio horizon. Diffraction losses over isolated obstacles are estimated using the Fresnel-Kirchoff knife-edge equations.

There have been many modifications and corrections to the original model. One important modification deals with radio propagation in urban areas, and this is particularly relevant to mobile radio communication[2]. This modification introduces an additional

term called the urban factor (UF) which has been derived by comparing the original Longley-Rice model to the Okumura model discussed below.

The Longley-Rice model cannot incorporate corrections due to environmental factors in the immediate vicinity of the vehicle. Furthermore, it does not address any factors to account for the effects of buildings and foliage, and multipath is not considered.

c) EPM-73

The Empirical Propagation Model-73 (EPM-73)[3] provides reasonable accuracy and simplicity with minimal input information. This model provides simple empirical formulas for various situations that give large-scale path loss in dB. The model can largely be divided into two groups according to the magnitude of the dimensionless parameter h/λ, where h is the antenna height and λ is the wavelength measured in the same units. Hence the model is actually a combination of high-h/λ and low-h/λ modes. These two modes are limited in their applicability to certain combinations of frequency, distance, and antenna height. For most situations, one of the two modes is clearly applicable, but in some instances a transition region will arise where one of the modes will be applicable only over certain distances. In this transition range, the mode that predicts the larger loss is generally the more accurate.

Because this is a purely empirical model, its validity can only be checked by comparison with measured data. Lustgarten and Madison [3] compared predicted and measured values over a frequency range of 20 to 10,000 MHz over approximately 7000 paths in many different areas. The results of these comparisons are given in Tables **??** through 11. Here, m is the average, over a number of paths, of the predicted loss minus the measured value, and the root mean square deviation σ_m is the standard deviation from the mean. A positive m means that the model is predicting too much loss compared with measured data. The tables also give comparisons between EPM-73 and other models. Note that TIREM (terrain-integrated rough-earth model) produces lower deviations for high values of h/λ. This model is more complex and includes terrain-data. The Longley-Rice model does not consider terrain features in detail and has accuracy similar to that of EPM-73.

d) Okumura Model

Of the models widely available, the Okumura model[7] is the one usually chosen for the analysis of mobile-radio propagation in urban and suburban areas. The modified model[8] is not as simple as the original Okumura model. Generally speaking, the Okumura model is considered to be among the best in terms of accuracy of path loss prediction for mature cellular radio systems in an urban or suburban area. It offers standard deviations of about 12 dB from measured data.

The median propagation loss L_{50} in the Okumura model can be written as

$$L_{50} = L_F + A_{mu}(f,d) + G(h_{te}) + G(h_{re}) \quad dB \tag{19}$$

where L_F is the free space propagation loss, A_{mu} is the median attenuation relative to free space, $G(h_{te})$ is the base station antenna height gain factor, $G(h_{re})$ is the mobile antenna height gain factor, h_{te} is the effective antenna height of the transmitter and h_{re} is the effective antenna height of the receiver.

Freq. (MHz)	Receiver Height (m)	No. of Paths	EPM-73 m (dB)	σ_m (dB)	IPS m (dB)	σ_m (dB)	TIREM m (dB)	σ_m (dB)	Longley-Rice m (dB)	σ_m (dB)
910	6	105	1.9	12.6	3.8	12.7	3.7	7.3	1.3	12.4
910	9	103	4.0	11.9	3.3	12.1	5.1	6.5	3.8	11.8
910	12	105	3.7	11.8	1.3	12.3	4.4	7.3	3.7	11.7
1846	6	115	-2.6	14.6	-2.3	15.7	-4.4	10.9	-3.0	14.7
1846	9	129	-2.0	15.5	-3.6	17.0	-5.0	11.7	-2.7	15.0
1846	12	129	-2.6	13.8	-5.4	15.6	-3.5	11.1	-3.6	13.5
4595	6	178	-1.4	18.1	-2.0	21.1	-5.0	13.0	-1.9	17.3
4595	9	206	-3.1	18.3	-6.5	20.7	-6.8	13.3	-3.1	18.1
4595	12	179	-3.1	18.1	-7.8	20.6	-6.4	12.4	-3.2	18.0
9190	6	213	0.7	20.5	-2.3	25.3	-3.8	14.6	1.7	20.2
9190	9	227	-0.3	20.5	-6.1	25.6	-4.9	13.9	0.3	20.2
9190	12	233	-0.9	18.8	-8.4	23.6	-4.8	13.5	-0.5	18.8

Note: These statistics in all cases are for Colorado Plains measurements taken from [4] with a horizontal polarization; transmitter antenna height of 6 m; careful siting assumed for Longley-Rice results.

Table 6: Comparison of predictions and measured data for high values of h/λ

Freq. (MHz)	Antenna Height (m)		Pola riza tion	Dist. Range (km)	Area	No. of Paths	EPM-73 m (dB)	σ_m (dB)	IPS m (dB)	σ_m (dB)	TIREM m (dB)	σ_m (dB)	Longley-Rice m (dB)	σ_m (dB)
20	3.3	3	V	1-50	col.	393	1.7	5.9	-5.1	5.9	—	—	-4.0	6.1
50	4	3	V	1-50	col.	393	-0.7	8.2	-1.7	8.3	-11.3	1.53	-4.3	8.6
100	3	6	H	1-80	col.	447	0.8	9.7	5.9	9.8	-7.2	12.5	-1.0	10.0
100	3	9	H	1-80	col.	444	1.5	10.0	5.7	10.1	-6.2	11.8	0.0	10.3
100	4	6	H	10-52	ohio	475	0.5	8.4	4.5	12.7	-3.4	11.9	-1.7	8.2

Note: These statistics are for measurements taken from [5]; Random siting assumed for Longley-Rice results.

Table 7: Comparison of predictions and measured data for high values of h/λ

EPM-73 m (dB)	σ_m (dB)	IPS m (dB)	σ_m (dB)	TIREM m (dB)	σ_m (dB)	Longley-Rice m (dB)	σ_m (dB)
-3.7	8.4	-4.0	8.8	-4.0	11.5	-3.7	8.1

Note: These statistics in all cases are for Colorado Plains measurements taken from [4] with 1000 samples; horizontal polarization; frequency=100MHz; distance range: 6.5 to 121km; random siting assumed for Longley-Rice Results.

Table 8: Comparison of predictions and measured data for intermediate values of h/λ and unequal antenna height

Approx. Freq. (MHz)	No. of Paths	EPM-73 m (dB)	EPM-73 σ_m (dB)	IPS m (dB)	IPS σ_m (dB)	TIREM m (dB)	TIREM σ_m (dB)	Longley-Rice m (dB)	Longley-Rice σ_m (dB)
230	117	9.1	12.6	11.9	13.8	7.9	7.2	11.7	12.3
410	121	4.8	15.6	7.2	16.3	5.4	11.5	9.1	15.6

Note: These statistics in all cases are for Colorado Plains measurements taken from [6] with horizontal polarization; antenna heights: 6m (transmitter) and 9m (receiver); distance range: 0.5 to 119 km; random siting assumed for Longley-Rice results.

Table 9: Comparison of predictions and measured data for intermediate values of h/λ and unequal antenna height

Area	No. of Paths	Dist. Range (km)	EPM-73 m (dB)	EPM-73 σ_m (dB)	IPS m (dB)	IPS σ_m (dB)	TIREM m (dB)	TIREM σ_m (dB)	Longley-Rice m (dB)	Longley-Rice σ_m (dB)
Washington	488	1-60	12.4	13.9	20.2	14.6	3.8	15.8	9.2	14.1
Idaho	232	10-34	-3.6	9.8	4.6	10.0	-10.8	16.3	-7.1	10.3
Wyoming	348	3-44	-2.9	11.2	4.0	11.7	-7.5	15.4	-6.1	11.4

Note: These statistics in all cases are for measurements taken from [6] with vertical polarization; frequency = 230 MHz; antenna height combinations of 0.6, 1, 2, and 3m; random siting assumed for Longley-Rice results.

Table 10: Comparison of predictions and measured data for very low antenna height

Frequency Range(MHz)	$20 \leq f \leq 100$	$100 \leq f \leq 200$	$200 \leq f \leq 400$
Standard Deviation(σ_m)	$5 \log f$	$13 \log f - 16$	14
Frequency Range(MHz)	$400 \leq f \leq 600$	$600 \leq f \leq 1000$	$1000 \leq f \leq 10,000$
Standard Deviation(σ_m)	$-20 \log f + 65$	10	$8 \log f - 14$

Table 11: Standard deviation (σ_m) of comparison between EPM-73 predictions and measured values

Okumura developed a set of curves that show the median attenuation A_{mu} relative to the free space loss, and plots of $G(h_{te})$ and $G(h_{re})$ in terms of the respective effective antenna heights are available. Generally, $G(h_{te})$ varies at a rate of $20dB$ per decade and $G(h_{re})$ at a rate of $10dB$ per decade for $h_{re} < 3m$.

Various corrections can be applied to the above formula based on terrain-related parameters such as transmitter effective antenna height h_{te}, terrain undulation height Δ_h, isolated ridge height, average slope of the terrain, and the mixed land-sea parameter. Correction factors for these parameters are also available in the form of Okumura curves.

For many situations, extrapolations of the derived curves can be made to generate values outside the range of measurements. The validity of the curves depends on the circumstances and the smoothness of the curve. This model is particularly good in urban and suburban areas but not as good in rural areas over irregular terrain.

e) Hata Model

The Hata model [9] is an empirical formulation of the graphical path loss information provided by the Okumura model. In this model, the urban area propagation loss is used as the standard loss and correction factors are considered for other situations. The standard formula for the median path loss in urban areas is given by

$$L_{50} = 69.55 + 26.16 \log_{10} f_c - 13.82 \log_{10} h_{te} - a(h_{re}) + (44.9 - 6.55 \log_{10} h_{te}) \log_{10} d \ dB \quad (20)$$

where f_c is the frequency between 150 and $1500MHz$, h_{te} is the effective transmitter antenna height from 30 to $200m$, h_{re} is the effective receiver (mobile) antenna height from 1 to $10m$, d is the distance between transmitter and receiver in kilometers, and $a(h_{re})$ is the correction factor for effective antenna height, which is a function of the size of the service area. For a small to medium sized city, the correction factor is given by

$$a(h_{re}) = (1.1 \log_{10} f_c - 0.7) h_{re} - (1.56 \log_{10} f_c - 0.8) \quad dB \quad (21)$$

and for a large city the correlation factor is

$$a(h_{re}) = \begin{cases} 8.29(\log_{10} 1.54 h_{re})^2 - 1.1 \quad dB \quad for \ f_c \leq 200MHz \\ 3.2(\log_{10} 11.75 h_{re})^2 - 4.9 \quad dB \quad for \ f_c \geq 400MHz \end{cases} \quad (22)$$

We need to modify the path loss formula as

$$L_{50} = L_{50}(urban) - 2[\log_{10}(\frac{f_c}{28})]^2 - 5.4 \quad dB \quad (23)$$

for a suburban area and

$$L_{50} = L_{50}(urban) - 4.78(\log_{10} f_c)^2 - 18.33 \log_{10} f_c - 40.98 \quad dB \quad (24)$$

for an open area.

The predictions of the Hata model are generally within 1 dB of those of the Okumura model if d exceeds $1km$. Because of this accuracy and simplicity, Hata's model has great practical significance, even though it does not have any path-specific corrections that are

available in Okumura's model.

B. Shadowing

Although we model the propagation loss as a random variable, this does not necessarily mean that the actual loss measured at a particular location fluctuates randomly. Rather, we observe the randomness as the location of the measurements from a specific point changes by a distance of λ or more. The expected value of the signal strength is the spatial average of the signal strengths. We call this the medium scale average of the local mean.

It is known that the local mean power fluctuates with a log-normal distribution as the antenna moves a distance of the order of tens or hundreds of wavelengths. More specifically, the probability distribution of the local mean power p is given by

$$f_p(p) = \frac{1}{\sqrt{2\pi}\sigma p} \exp(-\frac{1}{2\sigma^2} \ln^2 \frac{p}{\overline{p}}) \tag{25}$$

where $\overline{p}$ is the area mean power and λ is the the logarithmic standard deviation of the shadowing expressed in natural units. The standard deviation expressed in dB is 4.34 times the deviation in natural units.

Egli reported a logarithmic standard deviation of about 8.3 dB and 12 dB for VHF and UHF frequencies, respectively, for average terrain. These fluctuations are caused not only by local shadow attenuation from obstacles in the vicinity of the antenna, but also by large-scale effects leading to a coarse estimate of the area-mean power. This fluctuation reflects shadowing if the vehicle moves over several kilometers and is called the large-area shadowing.

In contrast, most papers on mobile propagation consider only the small-area shadowing; i.e., the log-normal fluctuations of the local-mean power over a distance of tens or hundreds of meters. Marsan et al reported a median of 3.7 dB for small area shadowing. Preller and Koch measured local-mean powers at $10m$ intervals and studied shadowing over $500m$ intervals. The maximum standard deviation experienced was about 7 dB, but 50% of all experiments showed shadowing of less than 4 dB.

C. Multipath Fading

In urban areas there are typically many objects that reflect, diffract, and scatter the transmitted signal to the receiver. These phenomena involve not only a change in amplitude but also a change of phase, so both constructive and destructive interference can occur. Signals arriving at the receiver within a fraction of one signaling interval can be considered to have arrived at roughly the same time. As the receiver moves, the trajectories of the multipath signals will change, which results in changes of magnitudes and phases. The result is a rapid fluctuation of power in the composite received signal.

This phenomenon of multipath fading is usually described by the Gaussian wide-sense stationary uncorrelated scattering model. If the number of signals received at roughly the same time is sufficiently large, then (through the central limit theorem) the net received signal can be modeled as a complex Gaussian random variable. The signal components received at different times are uncorrelated because they have traveled over different paths.

The magnitude of the complex Gaussian random variable is a Rayleigh random variable; hence Rayleigh fading occurs. Actual measurements show that the received signal strength may or may not follow the Rayleigh distribution[8]. This is due to the fact that in some cases only a few signals arrive at the receiver at roughly the same time.

a) Doppler Power Spectrum, Time Selectivity and Correlation Time

Due to the motion of the receiver or scatterers, the received signal along a given path can undergo a frequency shift. The actual amount of frequency shift Δf is given by

$$\Delta f = \frac{v}{c}\cos\theta \tag{26}$$

where v is the speed of the vehicle, c is the speed of the light, θ is the angle of the signal's arrival measured from the front of the vehicle, and f_c is the carrier frequency of the signal. The Doppler power spectrum measures the amount of power received at various frequency shifts, which can also be used to determine the direction from which the signals arrive at the receiver. When the Doppler power spectrum is highly localized to some specific direction, it strongly indicates that there are only a small number of paths arriving at the same time, and this may result in a departure from the Rayleigh fading model.

Although Doppler fading fluctuates, it does so smoothly as the receiver moves. Therefore, the received signal strengths measured at different locations are generally correlated in accordance with the time elapsed if the receiver moves at a constant rate. This correlation can be described as

$$E[r(t)r(t+\tau)] = r_0^2 J(\frac{2\pi v}{\lambda}\tau) \tag{27}$$

where $r(t)$ and $r(t+\tau)$ are the received signal strength at time t and $t+\tau$, v is the speed of the receiver, λ is the wavelength of the carrier, r_0^2 is the average power of the received signal, and $J(\cdot)$ is the inverse Fourier transform of the Doppler power spectrum. We observe that the correlation decreases as t increases. The threshold τ_c for which the correlation becomes small compared to a particular standard is called the correlation time to that standard. The correlation time is inversely proportional to the product of the speed of the vehicle and the carrier frequency f_c. For example, tau_c is given by

$$\tau_c \approx \frac{c}{4vf_c} \tag{28}$$

if we choose $0.5r_0^2$ as our standard of correlation with an isotropic receive antenna.

For frequencies of 1 GHz and vehicle speeds of $100km/hr$, for example, the rate of change of the fade is on the order of 100 times per second. For lower speeds and lower carrier frequencies the fade rate is lower. As a second example, for carrier frequencies of 50 MHz and vehicle velocities of $10km/hr$, time variations occur about once every two seconds. This is termed the time selectivity of the channel.

b) Delay Spread, Frequency Selectivity, and Coherence Bandwidth

In addition to time variations, fast fading also exhibits frequency selectivity. If there exists only one path for the signal transmission, then the channel impulse response $h(t)$

can be represented as a delta function, resulting in a frequency response $H(f,t)$ which is constant over the entire frequency range. However, when there are multiple routes to the receiver, the received signal arrives at different times and the impulse response $h(t)$ becomes a sum of delta functions with different amplitudes. As a result, the frequency response $H(f,t)$ is no longer a constant function of frequency. The maximum B_c such that $H(f,t)$ is roughly constant for all f in an interval of length B_c according to a particular standard is called the coherence bandwidth. The coherence bandwidth is usually defined to be

$$B_c \approx \frac{1}{8\Delta} \tag{29}$$

where Δ is the delay spread of the channel, which in turn is defined by

$$\Delta^2 = \frac{\int_0^\infty t^2|h(t)|^2}{\int_0^\infty |h(t)|^2} - (\frac{\int_0^\infty t|h(t)|^2}{\int_0^\infty |h(t)|^2})^2 \tag{30}$$

where $h(t)$ is the impulse response of the channel. The coherence bandwidths for path lengths of approximately 2 to $4km$ are typically in the range of 100 kHz to 1 MHz.

If a signal is spread over a bandwidth equal to twice the coherence bandwidth then fading can be mitigated to some extent by employing appropriate processing algorithms. Similar conclusions can be applied to time and frequency selectivity, which is how frequency-hopped and direct-sequence spread spectrum combat multipath fading.

2.2 Interference

In the case of wireless communication, two different types of interference can be experienced. Unintentional interference from other users is called multiple access interference (MAI). If the MAI is caused by a large number of users, then the cumulative effect can be approximated by an additive Gaussian noise process. Jamming is an intentional form of interference that aims to disrupt communications. Intelligent jamming signals can significantly degrade the performance of a communication system.

To design a robust communication system under hostile jamming environments, it is very important to consider worst-case scenarios. It is fairly easy to develop techniques for reliable communications when the jamming signals are highly structured, but building a robust receiver that performs well under a variety of jamming signals is much more difficult. One concept that is often employed to combat jamming is to build parallel branches in the receiver. One branch may work well for a certain subset of possible jamming scenarios and another branch may work well for another type of jamming situation. The receiver can select the correct data stream through error detection techniques.

Game theoretic methods can often be used to develop robust receivers in a jamming situation. A communication designer wants to find the best possible communication strategy for the worst possible jammer. The desire of the jammer is to find the best jamming strategy for the best possible communication system. If the performances for these two optimization problems are the same then we say the game has a saddle point solution. In what follows, we play the role of the communicator.

For certain scenarios the worst case jamming strategy is known. For example, if the communicator transmits a signal with a constraint on the average power and if the jammer has a similar constraint, then it is known that the optimal strategy for the jammer is to jam with a Gaussian distributed amplitude and that the communicator should also use a Gaussian distributed amplitude. However in many practical situations the amplitude of the communicator is constrained in peak value (as well as average value). Furthermore, receiver processing in many situations is limited by the number of quantization levels. In such cases, Gaussian jamming is no longer the worst case.

Next we describe a class of jamming strategies that closely approximate some realistic jamming scenarios. We do not, however, consider jamming strategies that attack vulnerabilities in synchronization, acquisition, and tracking.

2.2.1 Partial Time or Partial band Interference (Jamming)

One particularly useful class of jamming strategies is the class of partial-band jamming. In this strategy, the jammer is assumed to be average power constrained but not peak power constrained. Consider, for example, a frequency-hop spread-spectrum system. The jammer could place different levels of energy in different frequency bands. The jamming strategy could in fact consist of an arbitrary number of amplitude levels with different fractions of the band for each level. Realistically, the worst case jammer is actually two-valued, being either completely silent in a given band or jamming with the maximum possible power. The optimization strategy can be based on a single parameter in this case, which is the fraction of the band that is jammed. Once that is determined, the jammer distributes his total power over that bandwidth. If the jammer occupies a small fraction of the band, then the power density in that band is quite large but the probability of "hitting" the desired user is quite small. If the jammer occupies the whole band then he is guaranteed to affect the transmitted signal, but the jamming power spectral density is reduced exactly by the number of frequency slots (the processing gain) available to the transmitter. It turns out that in the absence of coding, the optimal jamming strategy (as shown above) is to jam only a small fraction of the band. With optimal coding of sufficiently small rate the worst-case jamming strategy is to jam the whole band, and thus coding allows spread-spectrum to operate with its full anti-jam processing gain. Similar arguments can be made for direct-sequence spread-spectrum with a pulsed interferer.

2.2.2 Multiple Access Interference

In addition to intentional jamming, there may exist interference due to multiple access. For a well-designed code-division multiple-access (CDMA) system, the output of a filter matched to a particular spreading sequence is small when a spreading sequence for a different user is input. This makes possible several simultaneous transmissions over a common communication channel. When the number of users transmitting signals is large, the interference can be approximated by additive Gaussian noise. However, if an undesired transmitter is located very close to the receiver, the communication quality will be significantly degraded due to the near-far phenomenon. Power control methods are generally used to mitigate multiple access interference when signals are transmitted from

multiple mobile users to a base station. However, in mobile-to-mobile communication systems, the situation is more complex and simple power control schemes may not be particularly effective.

2.3 Simulation Model

The purpose of our channel simulation is to develop models that can be used for the evaluation of various communication techniques based on actual measurements. Although our channel models are based on empirical data, we do not perfectly simulate actual situations for two reasons. First of all, it is not possible to reproduce the actual situations perfectly. Moreover, it is often not particularly useful to evaluate communication techniques for specific situations. Instead, we generate realistic models that contrast the performance of various communication techniques. Empirical data add a realistic dimension to our models.

Ideally, in a single channel simulation we should be able to generate the transmitted signal with certain power, attenuate it according to the large-scale path loss, shadow it, submit it to multipath fading, and then add it to other signals. Our simulation generates large scale propagation loss values in systems with both long and short packet duration, and then empirical data are used to develop a model for multipath fading.

2.3.1 Large-scale Propagation Loss and Shadowing

For our simulation, we use the Hata model and the EPM-73 for the prediction of large-scale path loss. EPM-73 is used for the rural situations and Hata model is used for suburban and urban areas. The root mean square deviations of the predictions from the actual measurements in various situations were introduced earlier. These deviations constrain the standard deviation of the log-normal distribution which we use to account for shadowing. We approximate these two values as equivalent.

A. Systems with short packet duration

Whether it is necessary to combine shadowing with multipath fading depends on the duration of a packet in the communication system. If the packet duration is sufficiently small so that the change of shadowing effect is negligible during its transmission, then we use only multipath fading in the simulation. In this case we combine large-scale propagation loss and shadowing to predict the performance of the system.

For example, if the large-scale path loss is L and if the standard deviation of the log-normal distribution is σ, then we can say that 99% (or 95%) of all possible situations the large-scale path loss combined with the shadowing loss does not exceed $L + 2.58\sigma(L + 1.96\sigma)$. So if the error rate is found to be Pe at the specific loss of $L + 2.58\sigma(L + 1.96\sigma)$ from our multipath fading channel model, then we can say with 99% (95%) of certainty that the error rate is within P_e.

B. Systems with long packet duration

When the packet duration is large enough that the vehicle can move through areas where the shadowing effect changes, then the situation is more complicated. In this

Excess Delay(μs)	0	0.3	0.7	1.0	1.6	2.5	3.0	3.7	6.3	8.0	9.5	10.2
Relative Average Amplitude	0.75	0.56	0.81	0.96	1.0	0.76	0.63	0.87	0.25	0.65	0.45	0.16

Table 12: Relative Average Amplitude on Pine Street (NY)

Excess Delay(μs)	0	1.1	4.15	4.8	5.4
Relatvie Average Amplitude	1.0	0.8	0.447	0.282	0.282

Table 13: Relative Average Amplitude in American Legion Drive (Suburban)

case we need to combine the effects of shadowing and multipath fading to simulate our communication system. Although the effect of shadowing can be described by a log-normal distribution, approximations must be used to model how it changes as the receiver moves. We do this by dividing the packet duration into subintervals such that the effect of shadowing is different from one subinterval to another, but within each subinterval the shadowing follows a log-normal distribution. In this way, we incorporate shadowing into our multipath fading channel simulation model.

2.3.2 Multipath Fading

The wide-sense stationary complex Gaussian uncorrelated scattering (WSSUS) channel model and the empirical data from the measurements performed by D. C. Cox [8, 10] are the theoretical and empirical bases for our multipath fading channel models. Specifically, we used the data measured on "Pine Street (New York)" [10] and in "American Legion Drive (Suburban)" [8]. For those two environments, both the average delay profiles and the Doppler spread power spectra are provided. The observed Doppler power spectrum at some particular delay may be highly localized around some frequency, indicating that the signals arriving at that particular delay mostly came from one specific direction. Because the reflection coefficients are highly dependent upon the angle of incidence, this implies that the distribution of received power should diverge from the Rayleigh distribution; this has been verified.

For the simulations, we first simplified the average delay profiles as shown in Tables 12 and 13.

The maximum excess delay on Pine Street is about $10\mu s$, with a delay spread of about $2.5\mu s$. Observations performed at other places also indicate that the maximum excess delay can reach $5 - 10\mu s$ in an urban area and that the delay spread is on the order of $2\mu s$, making the Pine Street data typical for urban areas. On the other hand, the data from American Legion Drive do not represent typical suburban situations. Usually the delay spread in a suburban area is on the order of $0.25\mu s$ while that of American Legion Drive is about $2\mu s$. However, this discrepancy is not a defect because we can introduce a scale parameter to the excess delays and observe the performance variations of the communication techniques as a function of the scale parameter. We expect that

the performance of a direct-sequence spread-spectrum (DSSS) system is not affected by the change of the scale parameter as long as the excess delays are resolvable, while that of a frequency hopping spread spectrum (FHSS) system may be affected by this parameter.

In our simulations, the Doppler delay power spectra are approximated by piecewise constant functions. As explained in sec. 2.1.2-C-a), the Fourier transforms of these functions give correlations between the received amplitudes at different times. To create the correlated Rayleigh fadings, we first generate complex white Gaussian random sequences with mean zero and unity variance, take their Fourier transforms, multiply them by the square roots of the Doppler delay spectra, and then take the inverse Fourier transforms. This gives complex correlated Gaussian random sequences whose amplitudes are Rayleigh random sequences. The correlated Rayleigh random sequences are used to evaluate the DSSS systems.

The complex correlated Gaussian random sequences combined with information about excess delays give the time variant impulse response $h(\tau, t)$ whose Fourier transform $H(f, t)$ is the time variant frequency response of the multipath fading channel. $H(f, t)$ and $H(f + \Delta f, t)$ are correlated in general, but the correlation decreases as Δf become larger. The coherence bandwidth for our system is about 100 kHz.

We divided the frequency range of interest into q non-overlapping slots so that the frequency response of the channel is roughly constant over each of these slots. The values of the frequency response at the central frequencies of the slots are used for the fading parameters of the frequency hopping systems. We choose q large enough that the slot bandwidth is smaller than the coherence bandwidth. The coherence bandwidth is inversely proportional to the delay spread Δ as shown above. This is why we expect the performance of the FHSS system will depend on the scale parameter for the excess delays.

Cox used 910 MHz signals in his measurements, but we use these simulation models for a carrier frequency of 30-2000 MHz. Although the data may not be accurate for frequencies different from 910 MHz, the general characteristics of the channel will be roughly the same.

3 Coded Modulation With Multicast Schemes for Communication Using Convolutional Code and Nonorthogonal Signals

In this section, we describe a technique for getting improved coded-modulation performance in communication system using orthogonal and nonorthogonal signals. The signals are bit interleaved convolutionally coded using the orthogonal code or nonorthogonal Nordstrom-Robinson code or one of the Kerdock codes. This combination allows for either coherent or noncoherent demodulation, and obtains large distance between coded waveforms. Since it is nearly as easy to demodulate the nonlinear Nordstrom-Robinson code as a standard orthogonal modulation, the gain is achieved without significant increase in complexity.

Furthermore, multi-rate data can be transmitted simultaneously through joint modulation or multiplexing schemes. This suggests a multicast strategy and adaptive coding can be applied with significant gain in signal-to-interference ratio for low rate input data over high rate data.

3.1 Introduction

This section is concerned with communication systems operating at low rate and low signal-to-noise ratio. Low rate convolutional codes combined with standard binary phase shift keying (BPSK) modulation do not have any advantage over moderate rate (rate 1/3-1/2) convolution codes concatenated with a repetition code and BPSK modulation. However, if a binary convolutional code is bit interleaved and concatenated with an orthogonal code/modulation then significantly larger distances are possible. This is possible provided sufficient interleaver depth is available or equivalently sufficient delay is allowed. Moreover, with an orthogonal code the receiver can demodulate the signal without knowledge of the phase of the received signal (noncoherent demodulation). In this section we consider the combination of bit interleaved convolutional codes with orthogonal and nonorthogonal modulation techniques such that noncoherent demodulation is still possible. Of specific interest is replacing the orthogonal modulation with a Nordstrom-Robinson code or a Kerdock code and determining the performance. We will show that such combinations allow for increase distance (at the same rate) as the combination of convolutional code and orthogonal modulation. The demodulation and decoding can be done in several ways. The optimum bit error probability algorithm, and a simplified algorithm (similar to the dual-max algorithm) are both derived.

The modulation schemes considered in this section are nonorthogonal. Here we use the terms modulation and code interchangeably. A code (or modulation signal set) is just a set of M vectors of length n with components from a common alphabet. In this section the alphabet is $\{\pm 1\}$. The orthogonal code is a set of M vectors of length $n = M$ such that any two distinct vectors have zero for their inner product. This code (signal set) can be doubled by adding the negative of each vector. This is called the biorthogonal code or biorthogonal modulation. Specifically, the 32-ary biorthogonal signal set $BO(16, 5)$ con-

sists of 32 vectors of length 16 such that distinct vectors are either orthogonal or antipodal. Another example is the *Nordstrom-Robinson* code $NR(16,8)$ [11] for which there are 256 vectors of length 16. The $NR(16,8)$ code is composed of the 32-ary biorthogonal code of length 16, $BO(16,5)$, plus seven of its proper translates. This code $NR(16,8)$ is a member of the Kerdock family of codes [11]. The code has 256 codewords while the $BO(16,5)$ has 32 codewords only. The complexity of the demodulation of the $NR(16,8)$, however, does not significantly exceed that of the $BO(16,5)$ under the dual-max algorithm.

Figure 10: Block Diagram of Transmitter

Figure 11: Block Diagram of Receiver

Coding is a crucial element of many communication systems. Convolutional coding generally performs better than hard-decision decoded block codes. Low rate convolutional codes have distance properties that are no better than a medium rate convolutional code concatenated with a repetition code. In order to achieve low rates with better distance properties, many times medium rate (e.g. rate 1/2) codes are concatenated with orthogonal codes. This not only allows for better distance properties but also gives the flexibility of allowing noncoherent demodulation. However, when combined with the M-ary modulation schemes, the resulting channel as seen by the decode becomes bursty. This can be mitigated by employing a bit interleaver of sufficiently large size as shown in Figure 10. The output of the convolutional encoder is interleaved and then used as the input to the M-ary modulation. At the receiver the demodulator (soft) output is deinterleaved and then decoded as shown in Figure 11. This method of coding and modulation achieves fairly large Hamming distance between codewords. For example, the concatenation of the constraint length 5 and rate 1/2 convolutional code with $BO(16,5)$ modulation achieves an overall Hamming distance of 56 provided there is sufficient interleaving depth. In this section we show that the orthogonal code can be replaced by a higher rate code (e.g. a Kerdock code or a Reed-Muller code) whereby a lower rate convolutional code for the same overall rate is possible. In this case the overall code achieves a larger distance and lower error rate in certain cases.

Multi-rate data can be transmitted through this new coded modulation scheme. One way of doing this multicast scheme is to jointly modulate data of different rates after a proper pre-spreading on the low rate data. The other way is to encode data of different rates separately and combine the output with a multiplexer. Adaptive coding for this multicast scheme can be applied at the receiver side based on channel condition, and significant gain in signal-to-interference ratio (SIR) can be obtained for low rate data over high rate data.

3.2 Modulation

In this section we derive the optimal and sub-optimal modulation/demodulation algorithms on M-ary orthogonal or nonorthogonal code.

3.2.1 Biorthogonal Code

The 32-ary biorthogonal code of length 16, $BO(16,5)$, has 32 codewords $\underline{v}_0, \underline{v}_1, ..., \underline{v}_{31}$ with minimum distance 8. Five bits b_1, b_2, b_3, b_4, b_5 can be transmitted in every 16 channel chips of $BO(16,5)$ and thus the rate is 5/16. Assume a codeword $\underline{v}_n$ corresponds to b_1, b_2, b_3, b_4, b_5 with $n = 16b_1 + 8b_2 + 4b_3 + 2b_4 + b_5$. When a codeword is transmitted and $\underline{r}$ is the received signal, conventional demodulation at the receiver is to find the maximum of all the output of the 32 correlators. However, if we focus on only one single bit [12] (e.g. b_1) among all b_1, b_2, b_3, b_4, b_5, then the optimal decision under MAP rule of b_1 is to compare the likelihood of $b_1 = 0$ and $b_1 = 1$ given $\underline{r}$, i.e., to compare $p(\underline{r}|b_1 = 0)Pr(b_1 = 0)$ and $p(\underline{r}|b_1 = 1)Pr(b_1 = 1)$. We know that

$$p(\underline{r}|b_1 = 0) = \sum_{b_2,b_3,b_4,b_5} p(\underline{r}|b_1 = 0, b_2, b_3, b_4, b_5)Pr(b_1 = 0, b_2, b_3, b_4, b_5) \quad (31)$$

$$p(\underline{r}|b_1 = 1) = \sum_{b_2,b_3,b_4,b_5} p(\underline{r}|b_1 = 1, b_2, b_3, b_4, b_5)Pr(b_1 = 1, b_2, b_3, b_4, b_5). \quad (32)$$

Assuming b_1, b_2, b_3, b_4, b_5 are equally likely, the optimal decision on b_1 is thus to compare

$$\sum_{b_2,b_3,b_4,b_5} p(\underline{r}|b_1 = 0, b_2, b_3, b_4, b_5) = \sum_{i=0}^{15} p(\underline{r}|\underline{v}_i) \quad (33)$$

and

$$\sum_{b_2,b_3,b_4,b_5} p(\underline{r}|b_1 = 1, b_2, b_3, b_4, b_5) = \sum_{i=16}^{31} p(\underline{r}|\underline{v}_i). \quad (34)$$

The above indicates that b_0 is optimally demodulated by the probability density functions (p.d.f.) of two disjoint cosets in $BO(16,5)$, $\{\underline{v}_0, \underline{v}_1, ..., \underline{v}_{15}\}$ and $\{\underline{v}_{16}, \underline{v}_{17}, ..., \underline{v}_{31}\}$. Obviously from (33) and (34) the log-likelihood $U_0 = \ln(p(\underline{r}|b_1 = 0)Pr(b_1 = 0)), U_1 = \ln(p(\underline{r}|b_1 = 1)Pr(b_1 = 1))$ of b_1 can be equivalently written as

$$U_0 = \ln(\sum_{i=0}^{15} p(\underline{r}|\underline{v}_i)) \quad (35)$$

$$U_1 = \ln(\sum_{i=16}^{31} p(\underline{r}|\underline{v}_i)). \quad (36)$$

In addition, a sub-optimal algorithm, dual-max, is to look at the maximum log-likelihood only in the two cosets. Then U_0, U_1 of b_1 can be rewritten as

$$U_0 = \ln(\max_{i=0}^{15}\{p(\underline{r}|\underline{v}_i)\}) = \max_{i=0}^{15}\{\ln(p(\underline{r}|\underline{v}_i))\} \quad (37)$$

$$U_1 = \ln(\max_{i=16}^{31}\{p(\underline{r}|\underline{v}_i)\}) = \max_{i=16}^{31}\{\ln(p(\underline{r}|\underline{v}_i))\}. \quad (38)$$

This dual-max algorithm can significantly reduce complexity while its error performance is only marginally worse than that of the optimal algorithm. Throughout, we assume dual-max demodulation unless otherwise specified. The above demodulation can be applied on b_2 through b_5 as well. The error performance of all the five bits b_1, b_2, b_3, b_4, b_5 is identical because of the symmetry of $BO(16,5)$.

3.3 Orthogonal Code

Four bits b_1, b_2, b_3, b_4 are transmitted in a 16-ary orthogonal code of length 16, $O(16,4)$, with 16 codewords $\underline{v}_0, \underline{v}_1, ..., \underline{v}_{15}$. Following the similar procedure in Subsection 3.2.1, under optimal demodulation the log-likelihood U_0, U_1 of b_1 is as follows:

$$U_0 = \ln(\sum_{i=0}^{7} p(\underline{r}|\underline{v}_i)) \tag{39}$$

$$U_1 = \ln(\sum_{i=8}^{15} p(\underline{r}|\underline{v}_i)) \tag{40}$$

and under dual-max demodulation

$$U_0 = \max_{i=0}^{7}\{\ln(p(\underline{r}|\underline{v}_i))\} \tag{41}$$

$$U_1 = \max_{i=8}^{15}\{\ln(p(\underline{r}|\underline{v}_i))\}. \tag{42}$$

Again, parallel demodulation can be also applied on b_2 through b_4. The error performance of all the four bits b_1, b_2, b_3, b_4 is identical because of the symmetry of $O(16,4)$.

3.4 Nonorthogonal Code

If we start with biorthogonal code $BO(16,5)$, we can increase the number of codewords by adding seven carefully selected translates of $BO(16,5)$, with the number of codewords increasing from 32 to 256 while the minimum distance decreasing from 8 to 6. By doing so we get the nonlinear Nordstrom-Robinson code $NR(16,8)$ [11]. Eight bits $b_1, b_2, b_3, b_4, b_5, b_6, b_7, b_8$ are transmitted in the $NR(16,8)$. Following the similar procedure in Subsection 3.2.1, the log-likelihood U_0, U_1 of b_1 under optimal demodulation is as follows:

$$U_0 = \ln(\sum_{i=0}^{127} p(\underline{r}|\underline{v}_i)) \tag{43}$$

$$U_1 = \ln(\sum_{i=128}^{255} p(\underline{r}|\underline{v}_i)) \tag{44}$$

and under dual-max demodulation

$$U_0 = \max_{i=0}^{127}\{\ln(p(\underline{r}|\underline{v}_i))\} \tag{45}$$

$$U_1 = \max_{i=128}^{255}\{\ln(p(\underline{r}|\underline{v}_i))\}. \tag{46}$$

Again, parallel demodulation can also be applied on b_2 through b_8. However, the performance of the eight bits in $NR(16,8)$ is almost but not exactly identical with each other. To be more specific, b_1, b_2, b_3 have same error behavior while the other five bits b_4, b_5, b_6, b_7, b_8 have the same behavior, and the former is slightly worse than the latter.

Biorthogonal code cannot be employed in a noncoherent demodulator. If only the orthogonal subcode of the $BO(16,5)$ and its seven translates in $NR(16,8)$ are used, we have a *modified Nordstrom-Robinson* code $NR^*(16,7)$ with 128 codewords. Seven bits $b_1, b_2, b_3, b_4, b_5, b_6, b_7$ are transmitted in the $NR^*(16,7)$. The log-likelihood U_0, U_1 of b_1 under optimal demodulation is as follows:

$$U_0 = \ln(\sum_{i=0}^{63} p(\underline{r}|\underline{v}_i)) \tag{47}$$

$$U_1 = \ln(\sum_{i=64}^{127} p(\underline{r}|\underline{v}_i)) \tag{48}$$

and under dual-max demodulation

$$U_0 = \max_{i=0}^{63}\{\ln(p(\underline{r}|\underline{v}_i))\} \tag{49}$$

$$U_1 = \max_{i=64}^{127}\{\ln(p(\underline{r}|\underline{v}_i))\}. \tag{50}$$

Again, parallel demodulation can also be applied on b_2 through b_7. Similar to $NR(16,8)$, b_1, b_2, b_3 of $NR^*(16,7)$ have same error behavior while b_4, b_5, b_6, b_7 have the same behavior, and the former is slightly worse than the latter.

The number of vectors can be expanded from 256 to 2048 to obtain the linear Reed-Muller code of order 2 and of length 16, $RM(16,11)$. Here the distance decreases further from 6 to 4. The number of vectors can be expanded from 2048 to 32768 to obtain the Reed-Muller code of order 3 and of length 16, $RM(16,15)$. Here the distance decreases further from 4 to 2 [11]. Following a similar procedure as above, we obtain modified Reed-Muller code of order 2, $RM^*(16,10)$, as a subcode of $RM(16,11)$ with half the codewords, and modified Reed-Muller code of order 3, $RM^*(16,14)$, as a subcode of $RM(16,15)$ with half the codewords. The relationships between all the orthogonal and nonorthogonal codes mentioned so far is [11]

$$BO(16,5) \subset NR(16,8) \subset RM(16,11) \subset RM(16,15) \tag{51}$$

$$O(16,4) \subset NR^*(16,7) \subset RM^*(16,10) \subset RM^*(16,14). \tag{52}$$

Similar demodulation scheme can be also used on $RM(16,11)$, $RM^*(16,10)$, $RM(16,15)$, and $RM^*(16,14)$. However, complexity increase is expected due to large numbers of codewords.

$NR(16,8)$ is actually one example of the *Kerdock* code of length 16 [11]. At length 64, we can also find biorthogonal code $BO(64,7)$, orthogonal code $O(64,6)$, Kerdock code of length 64, $KR(64,12)$, and modified Kerdock code of length 64, $KR^*(64,11)$. Similar modulation/demodulation can also be applied on all these codes of length 64.

3.5 Coding

In this section the modulation schemes in Section 3.2 are concatenated with convolutional coding. When a convolutional code with minimum Hamming distance d_{min} is followed by a very long interleaver and then followed by $O(16,4)$ modulation of rate 1/4, the overall squared Euclidean distance is $32d_{min}$. The overall rate of communication in bits/chip is $1/4n$ where $1/n$ is the rate of the convolutional code. In practice a rate 1/2 convolutional code is used making the overall rate 1/8. Following this idea we can combine a rate 2/5, 2/7, or 1/4 convolutional code with $BO(16,5)$, $NR^*(16,7)$, or $NR(16,8)$ whose rate is 5/16, 7/16, or 1/2 to make overall rate also 1/8, and thus a fair comparison can be made. The constraint length of the convolutional code in this research is assumed 5 unless otherwise specified. Here we need to point out that most numerical results in this section are mainly based on simulations.

As has been stated in Section 3.2, $O(16,4)$, $BO(16,5)$ has distance 8, $NR^*(16,7)$, $NR(16,8)$ has distance 6, $RM^*(16,10)$, $RM(16,11)$ has distance 4, and $RM^*(16,14)$, $RM(16,15)$ has distance 2. As an example we consider the $NR^*(16,7)$ code with a low rate convolutional code which is a rate 1/4 code punctured appropriately to make the rate 2/7. The combination then has rate $(2/7) \times (7/16) = 1/8$ which is the same as the $O(16,4)$ scheme with a rate 1/2 convolutional code. The distance of the scheme is calculated as follows. The $NR^*(16,7)$ has squared Euclidean distance of $6 \times 4 = 24$ while $O(16,4)$ has squared Euclidean distance of $8 \times 4 = 32$. The rate 2/7 punctured convolutional code has distance 13 while the rate 1/2 convolutional code with distance 7. Thus, with sufficient interleaving the convolutionally coded $NR^*(16,7)$ has overall distance $24 \times 13 = 312$ while the convolutionally coded $O(16,4)$ has overall distance $32 \times 7 = 224$. This would correspond to a 1.44dB gain in AWGN channel at high SNR. The following table shows the various combinations of coding and modulation and the overall distance achieved of convolutionally coded $O(16,4)$, $NR^*(16,7)$, $O(64,6)$ (with distance 32), and $KR^*(64,11)$ (with distance 28) [13]. For length 16 modulation vectors, the optimum combination for memory 7 is $NR^*(16,7)$ followed by a rate 2/7 convolutional code. This has coding gain of $10\log_{10}((4\times114)/(4\times80)) = 1.54$dB in AWGN. For length 64 and convolutional codes with memory 7, $KR^*(64,11)$ show a $10\log_{10}((4\times868)/(4\times512)) = 2.3$dB gain in overall distance over $O(64,6)$. However, we must point out that the above again is merely in the aspect of minimum overall distance with no consideration of number of neighbors in codewords or paths in the trellis, which dominate error performance at low or medium SNR.

Length	Rate	Distance/4	Memory	Rate	Distance	Overall Rate	Overall Distance
16	4/16	8	4	1/2	7	1/8	56
16	7/16	6	4	2/7	13	1/8	78
16	10/16	4	4	1/5	20	1/8	80
16	14/16	2	4	1/7	28	1/8	56
16	4/16	8	5	1/2	8	1/8	64
16	7/16	6	5	2/7	15	1/8	90
16	10/16	4	5	1/5	22	1/8	88
16	14/16	2	5	1/7	32	1/8	64
16	4/16	8	6	1/2	10	1/8	80
16	7/16	6	6	2/7	16	1/8	96
16	10/16	4	6	1/5	25	1/8	100
16	14/16	2	6	1/7	36	1/8	72
16	4/16	8	7	1/2	10	1/8	80
16	7/16	6	7	2/7	19	1/8	114
16	10/16	4	7	1/5	28	1/8	112
16	14/16	2	7	1/7	40	1/8	80
64	6/64	32	4	1/3	12	1/32	384
64	11/64	28	4	2/11	21	1/32	588
64	6/64	32	5	1/3	13	1/32	416
64	11/64	28	5	2/11	24	1/32	672
64	6/64	32	6	1/3	15	1/32	480
64	11/64	28	6	2/11	28	1/32	784
64	6/64	32	7	1/3	16	1/32	512
64	11/64	28	7	2/11	31	1/32	868

Table: Code and modulation parameters and overall distance.

In general, under the same overall rate, the error rate of convolutionally coded $BO(16,5)$ is lower than that of convolutionally coded $O(16,4)$, and the error rate of convolutionally coded $NR(16,8)$ is lower than that of convolutionally coded $NR^*(16,7)$. This is because $BO(16,5)$ and $O(16,4)$ have the same minimum distance, or $NR(16,8)$ and $NR^*(16,7)$ have the same minimum distance, but the former can always be combined with a lower rate convolutional code and thus higher error correcting capability. This suggests $BO(16,5)$ or $NR(16,8)$ should be employed whenever coherent demodulation is possible.

The performance can be further improved by concatenating the convolutional code with an outer Reed-Solomon (RS) code, if extra complexity is allowed. A symbol interleaver of the coded RS symbols should be provided, if possible, to overcome the effect of bursty errors of the convolutional code.

3.6 Results of Coded Modulation Schemes

In this section we show simulation results of different coding and channel conditions. The bandwidth is 10MHz(33-43 MHz), the chip rate is 160 kbps, and the channel is divided into 62 subchannels, and assumed frequency hopped. In the simulation we assume the

coded modulation scheme is $BO(16,5)$, the signal is with power P, and there is Gaussian-like jamming with power J but no background noise. The jamming strategy is always all-band unless otherwise specified.

In Figure 12 we show the error performance of input rate 256/30 bps over a slow Rayleigh faded frequency-hopped channel with ideal channel interleaving.

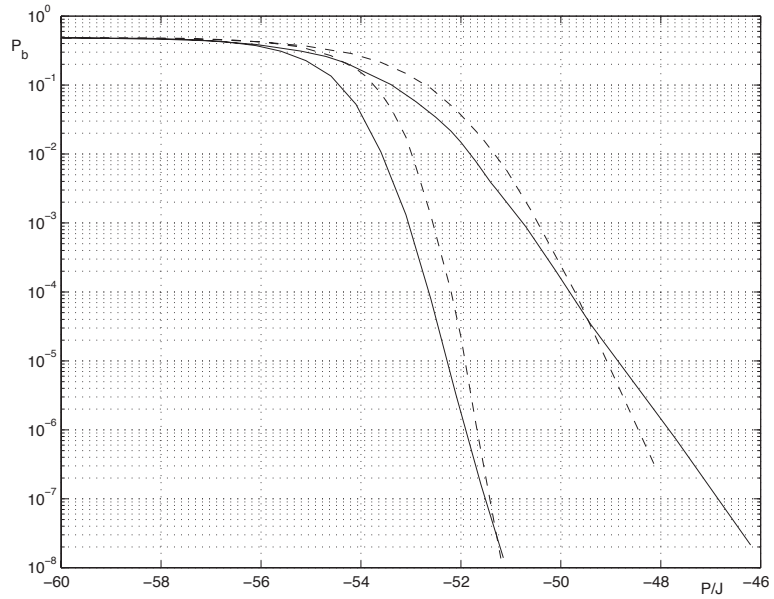

Figure 12: Slow Rayleigh Fading Channel. Solid Line: RS(31,25) Code Total Number of Information Bits: 250 Pre-Spreading Factor: 2363 Hopping Rate: 10kHz(left) and 4.23Hz(right) Dashed Line: RS(63,43) Code Total Number of Information Bits: 258 Pre-Spreading Factor: 2000 Hopping Rate: 10kHz(left) and 5Hz(right)

In Figure 13 we show the error performance of input rate 256/30 bps over a realistic fading channel with vehicle velocity 30 m/s.

In Figure 14 we show the bit error rate of input rate 256/30 bps coded with RS(31,25) code over a realistic fading channel with different vehicle velocities 30 m/s and 0.

In Figure 15 we compare the input rate 256/30 bps coded with RS codes under realistic fading channel at vehicle velocity 30m/s, and under slow Rayleigh fading channel with ideal channel interleaving. The hopping rate is 10kHz.

In Figure 16 we show the bit error rate of input rate 9600 bps coded with RS(62,24) code over a realistic fading channel with different vehicle velocities 30 m/s and 0. The hopping rate is 10kHz. No pre-spreading for this high input rate.

In Figure 17 we show the effect a partial-band jamming channel on input rate 9600 bps coded with RS(63,25) code over a realistic fading channel with different vehicle velocities 0. The channel is either being jammed at probability ρ by Gaussian interference with power spectrum density N_J/ρ, or with negligible background noise at probability $(1-\rho)$. Although we find out that ρ has little effect on the code with low input rate and high pre-spreading factor, for a high input rate with no or low pre-spreading, e.g. 9600bits/s,

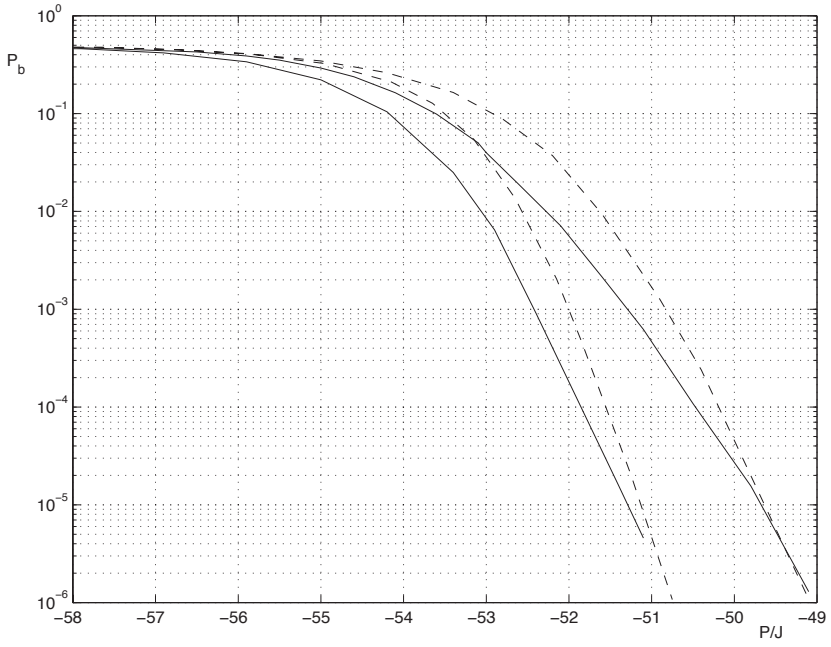

Figure 13: Realistic Fast Fading Channel. Solid Line: RS(31,25) Code Total Number of Information Bits: 250 Pre-Spreading Factor: 2363 Hopping Rate: 10kHz(left) and 4.23Hz(right) Dashed Line: RS(63,43) Code Total Number of Information Bits: 258 Pre-Spreading Factor: 2000 Hopping Rate: 10kHz(left) and 5Hz(right)

$\rho = 1$, full-band jamming, is always the best strategy of the jammer.

3.7 Multicast Schemes

Input data streams of different rates can be transmitted simultaneously through the above coded modulation scheme. One way of doing this multicast scheme is to jointly modulate data of different rates after a proper pre-spreading on the low rate data. The other way is to encode data of different rates separately and combine the output with a multiplexer. Adaptive coding for the multicast schemes can be applied at the receiver side based on channel condition.

3.8 Multiplexing

Input data of two different rates can be combined through a multiplexer as illustrated in Figure 18. In this multiplexing scheme, each date stream is coded and modulated separately and then combined through a multiplexer with a pre-spreading on the lower rate data.

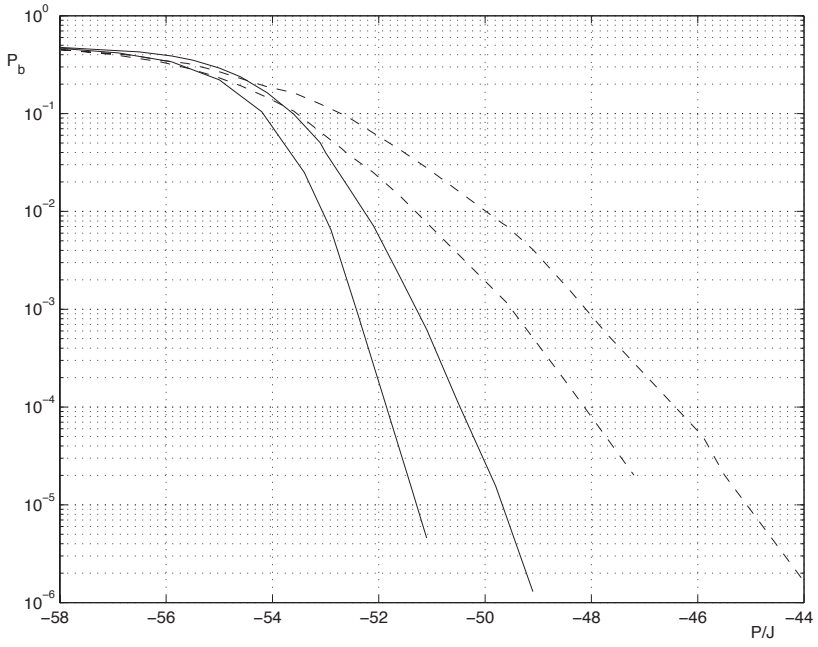

Figure 14: Realistic Fading Channel with Different Vehicle Velocities. Solid Line: Vehicle Velocity: 30m/s Hopping Rate: 10kHz(left) and 4.23 Hz(right) Dashed Line: Vehicle Velocity: 0 Hopping Rate: 10kHz(left) and 4.23 Hz(right)

For example, under $BO(16,5)$ modulation and $r_1 = 10$bps, $r_2 = 10$kbps, $R_c = 160$kbps, n is 2000 when $R_1 = 1/2$ and $R_2 = 1$(uncoded) and n is 500 when $R_1 = 1/2$ and $R_2 = 1/4$. This large number of pre-spreading length n indicates a significant gain in signal-to-interference ratio for the 10bps stream over 10kbps stream. In these two cases, the low rate stream occupies 80% of the channel chips when $n = 2000$, and 20% of the channel chips when $n = 500$.

3.9 Joint Modulation

Instead of multiplexing, another way to combine data streams is bit allocation in the $\log_2(M)$ bits in the M-ary modulation as illustrated in Figure 19. Multiplexer is substituted by a modulator, whose input is decided jointly by the two coded date streams.

Given that both modulators Figure 19 are $BO(16,5)$, if 4 of the 5 bits in $BO(16,5)$ are allocated to rate r_1 data and 1 bit to rate r_2 data, r_1, r_2, R_1, R_2, n have the following relationship

$$(r_1/R_1)(16/5)n = \frac{4R_c}{16} \tag{53}$$

$$r_2/R_2 = \frac{R_c}{16} \tag{54}$$

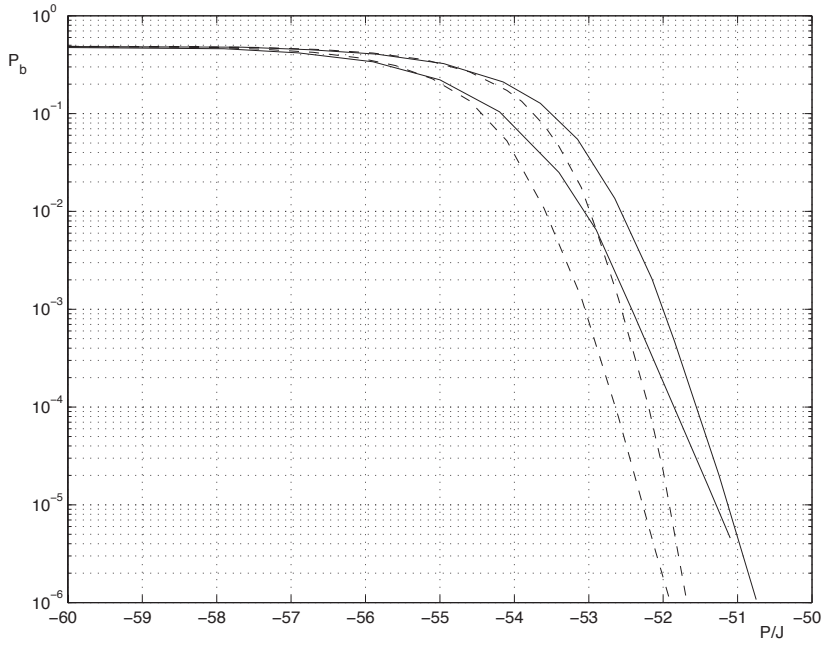

Figure 15: Comparison of Slow Rayleigh Fading Channel and Realistic Channel Solid Line: RS(31,25)(left) and RS(63,43)(right) Code Realistic Fading Channel Dashed Line: RS(31,25)(left) and RS(63,43)(right) Code Slow Rayleigh Fading Channel

and the following relationship if 1 bit to rate r_1 data and 4 bits to rate r_2 data,

$$(r_1/R_1)(16/5)n = \frac{R_c}{16} \tag{55}$$

$$r_2/R_2 = \frac{4R_c}{16} \tag{56}$$

For example, for $r_1 = 10$bps, $r_2 = 10$kbps, and $R_c = 160$kbps, $n = 625$ in (53) when $R_1 = 1/2$ and $R_2 = 1$(uncoded), and $n \simeq 156$ in (55) when $R_1 = 1/2$ and $R_2 = 1/4$. A significant gain in signal-to-interference ratio is also observed for the 10bps stream over 10kbps stream in the joint modulation scheme.

3.10 Results

In Figure 20 we show the performance of the two input streams at different data rates $r_1 = 10$bps, $r_2 = 10$kbps, and $R_c = 160$kbps under $BO(16, 5)$ modulation with power P over a full-band Gaussian jamming channel with jamming power J. The convolutional code is of memory 4, and the size of the interleaver is assumed very large. Both multicast schemes of multiplexing and joint modulation are shown and compared. We can see that multiplexing works better than joint modulation on low data rate, while joint modulation works better on high data rate.

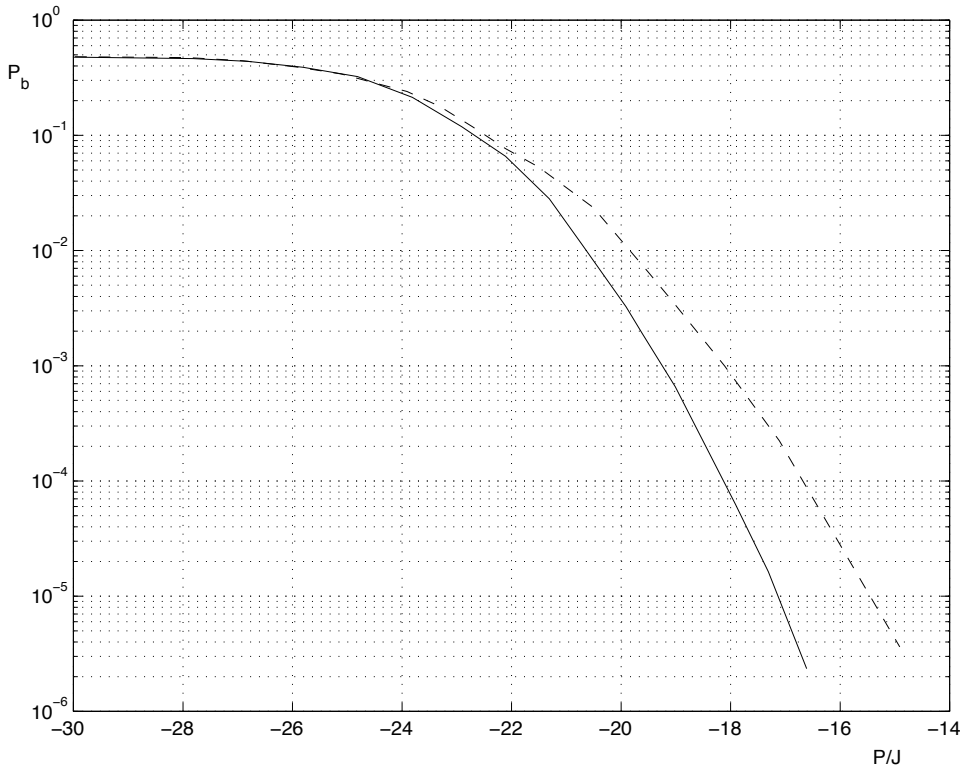

Figure 16: Realistic Fading Channel with Different Vehicle Velocities. Solid Line: Vehicle Velocity: 30m/s Dashed Line: Vehicle Velocity: 0 Total Number of Information Bits: 9600

3.11 Conclusion

A new approach to M-ary orthogonal, biorthogonal, and nonorthogonal modulation schemes has been examined. The new modulation scheme can provide good distance properties when combined with orthogonal coding. Besides, since in the new scheme each bit in the M-ary modulation is decided individually, the new scheme can be regarded as binary, memoryless, if interleaving of very large size is provided when necessary. This new coded modulation can also be applied on multicast schemes.

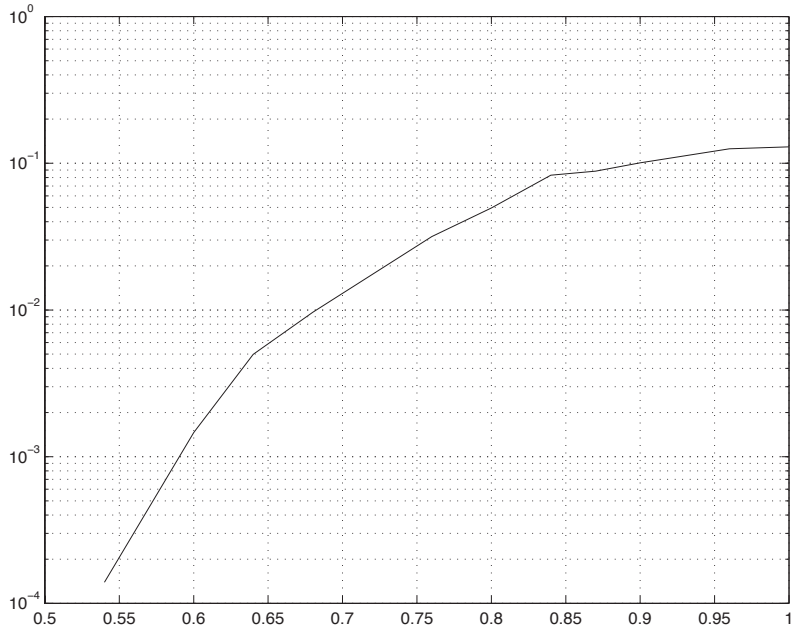

Figure 17: Partial-band Jamming Channel

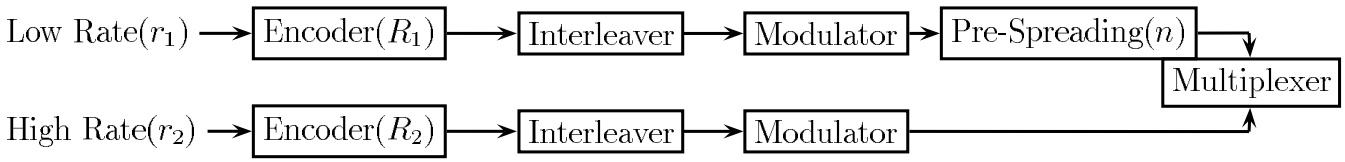

Figure 18: Block Diagram of Multiplexing Scheme

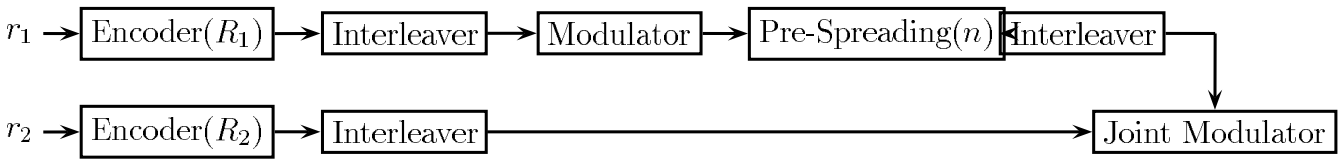

Figure 19: Block Diagram of Joint Modulation Scheme

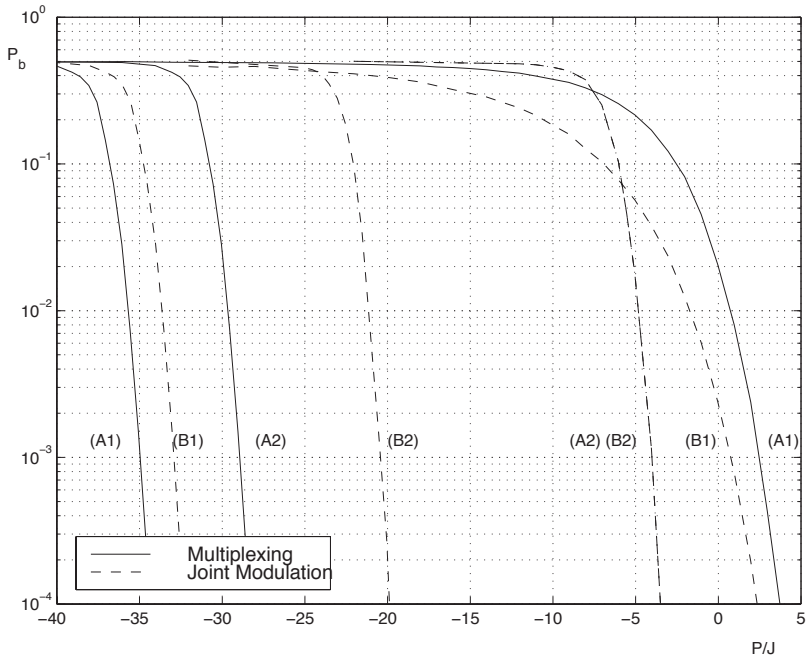

Figure 20: Multicast Schemes

$$(A1) \quad : \quad R_1 = 1/2, n = 2000; R_2 = 1 \tag{57}$$

$$(A2) \quad : \quad R_1 = 1/2, n = 500; R_2 = 1/4 \tag{58}$$

$$(B1) \quad : \quad R_1 = 1/2, n = 625; R_2 = 1 \tag{59}$$

$$(B2) \quad : \quad R_1 = 1/2, n \simeq 156; R_2 = 1/4 \tag{60}$$

4 Turbo codes for FH-SS with partial-band jamming

Turbo codes are an exciting new channel coding scheme that achieve data communication at signal-to-noise ratios close to the Shannon limit. The results published in the inaugural paper by Berrou (Berrou et al, 1993) were so good that they were met with much skepticism by the coding community. Since then, however, these results have been reproduced and even improved. Consequently, much of the present research is focused on applying turbo codes to different systems.

The encoder is a parallel concatenation of two or more systematic constituent codes separated by interleavers. The key element of the encoder are the interleavers which yield improved performance for larger interleaver lengths. This phenomena is called interleaver gain. The turbo decoder uses an iterative decoding algorithm which makes use of MAP decoders matched to each of the constituent encoders. Essentially, each MAP decoder computes likelihood estimates, L_k, of the data bits.

$$L_k = \frac{p(d_k = 1|\underline{y})}{p(d_k = 0|\underline{y})}$$

where $\underline{y}$ represents the vector of channel outputs.

Each MAP decoder generates these likelihoods and then passes this information to the next MAP decoder. These likelihood estimates are used as a priori information by which new likelihood estimates are computed. This process is iterated several times, eventually converging to some low bit error rate.

Our research has focused on the application of turbo codes to slow frequency-hopped spread-sprectrum (FH-SS) with partial-band interference. We also consider FH-SS with partial-band interference and slow Rayleigh fading. Our approach is to exploit the memory of the channel by estimating which hops have been jammed and in the case with fading, what the faded amplitudes are. It was mentioned above that the turbo decoder iteratively improves log-likelihood ratios. An alternative way to view this is that the turbo decoder iteratively improves $p(d_k|\underline{y})$, the information bit estimates. In our work, the memory in the channel is used to estimate unknown channel parameters. If these channel estimates are computed using an iterative structure similar to that of the turbo decoder, perhaps these estimates can also be improved. Thus in our work, iterative estimation and decoding is performed.

In order to gauge the accuracy of these estimation procedures, we compare their results to cases where side information is available. By side information (SI), we refer to the perfect knowledge of which hops have been jammed (jamming SI – J SI) and the exact values of the fade amplitudes (fading SI – F SI).

For our simulations, we consider coherent (BPSK modulation) and noncoherent reception (BFSK modulation); variable number of bits per hop (1 bit per hop case is called 'IID',

multiple bits per hop cases are called 'Memory'); and cases with varying levels of side information. For all simulations, each constituent code was a rate 1/2, memory 4 recursive systematic convolutional code and each packet contained 1760 information bits.

Figure 21 shows the performance of turbo codes in coherently received FH-SS with partial-band interference. Plotted is the minimum signal-to-noise ratio (SNR) required to achieve a packet error rate (PER) of 10^{-2}. The 'Memory' case had 3 bits per hop (BPH).

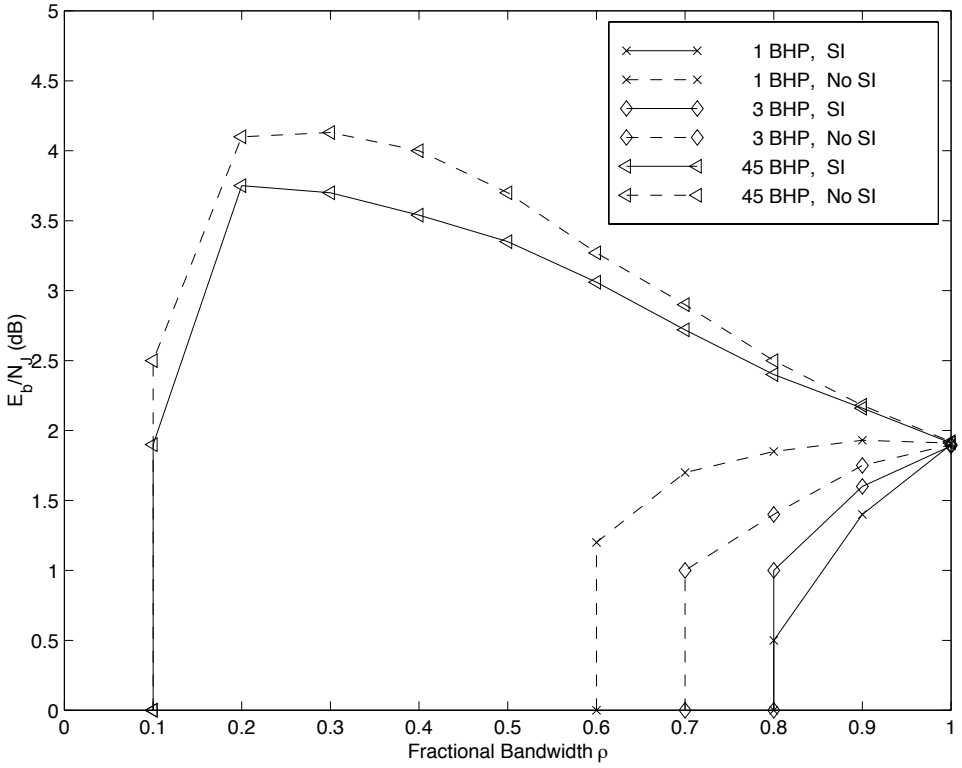

Figure 21: Coherent Reception of Turbo Codes in FH-SS with Partial-Band Jamming

Figure 22 shows turbo codes in noncoherently received FH-SS with partial-band interference. Plotted is the minimum signal-to-noise ratio (SNR) required to achieve a PER of 10^{-3}. In the legend, the acronym "NSI" denotes "No Side Information".
The primary result of Figures 21 and 22 is exhibited by noticing the tradeoff in performance as the number of bits per hop is varied. Because channel state estimates will improve if the number of bits per hop increases, performance differences between corresponding SI and no SI cases become smaller as the number of bits per hop increase. Notice, however, that the performance of SI cases degrades as the channel memory increases. This occurs because a fewer total number of hops are used.

Figures 23 and 24 show the performance of turbo codes in FH-SS with both partial-band interference and Rayleigh fading. Figure 23 shows the simulation results for coherent reception; Figure 24 has the results for noncoherent reception. The desired PER is 10^{-3}.

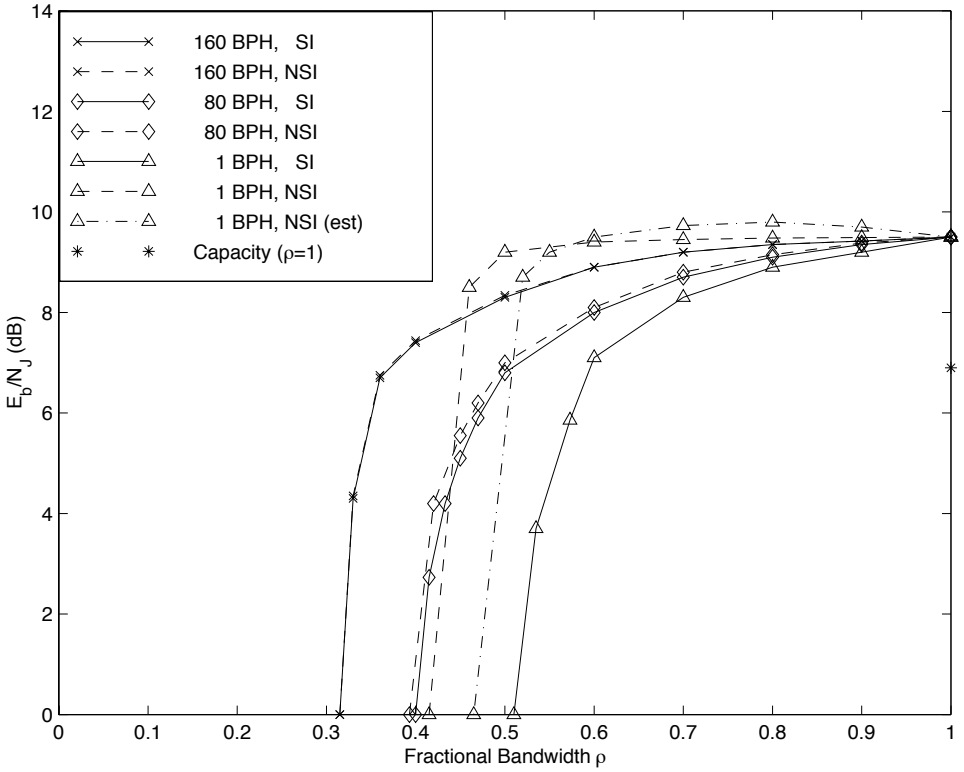

Figure 22: Noncoherent Reception of Turbo Codes in FH-SS with Partial-Band Jamming

When estimating the fade amplitudes (for cases where fading SI is unavailable), we optimally quantized the amplitudes to Q levels. The results shown below have similar form to the ones discussed above.

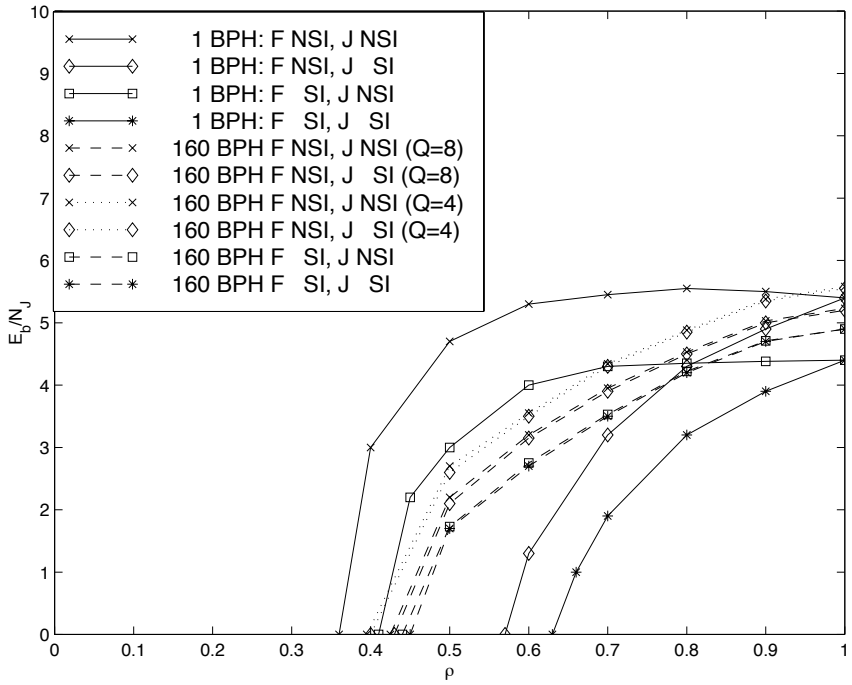

Figure 23: Turbo Codes in Coherent FH-SS with Partial-Band Jamming and Rayleigh Fading

In previous sections, we spoke of the the fundamental limit on performance with the best code. This limit is called capacity. Looking at Figures 22 and 24, we can compare the coding results of turbo codes with capacity. In the absence of fading, turbo codes are a little more than 2 dB from capacity. With fading, turbo codes are less than 3 dB from capacity. Note, however, that due to interleaver gain, this gap can be narrowed significantly with the use of larger interleaver lengths.

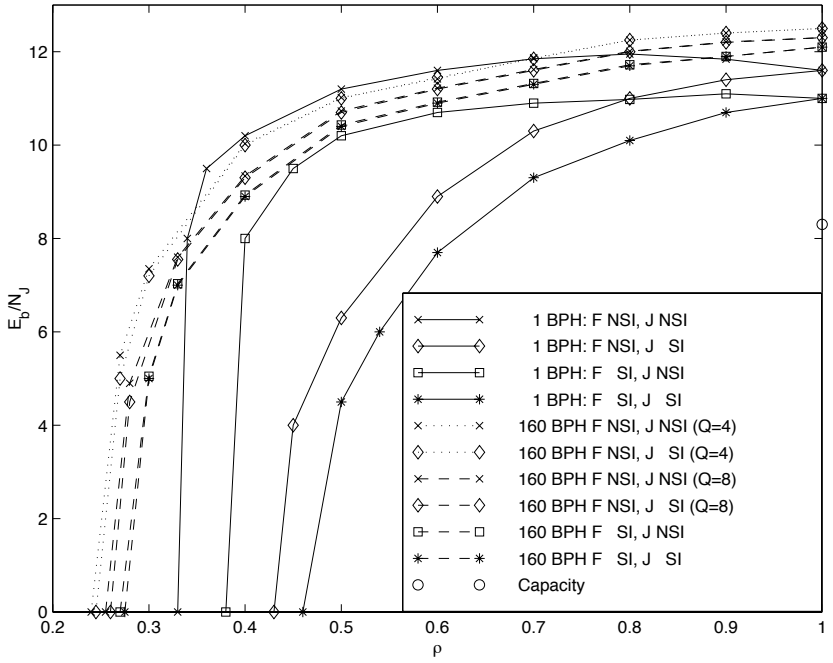

Figure 24: Turbo Codes in Noncoherent FH-SS with Partial-Band Jamming and Rayleigh Fading

5 Performance of Reed-Solomon Codes in AWGN and Rayleigh Fading

In this section we consider a system which transmits all of its information in a single data stream. The stream can be modulated in a number of different ways, but the data rate of the stream comes from only one source, at only one rate. We consider different channel conditions that impair detection of the transmitted data, and we employ different coding and modulation schemes to combat these impairments.

We consider a very low rate data source, one that generates only 250 bits every 30 seconds. It is desired to transmit this data over a wireless data link in a reliable fashion. More specifically we answer the question of what transmit power is required to achieve a 10^{-8} packet error probability for various coding and modulation schemes in different channel conditions.

The source data is grouped into K groups of $\log_2(M)$ bit symbols and redundancy is added by encoding this data using (N,K) Reed-Solomon (RS) with error correcting power of $t = \lfloor \frac{N-K}{2} \rfloor$. The encoded symbols are then transmitted using an M-ary modulation scheme. The transmitted symbols are corrupted by channel noise (either additive, multiplicative or both) and demodulated at the receiver. The receiver uses a hard symbol-by-symbol detection scheme and passes its best guess to the decoding section. The decoder evaluates the possibly corrupted received data and makes a decision as to which K symbols were originally sent.

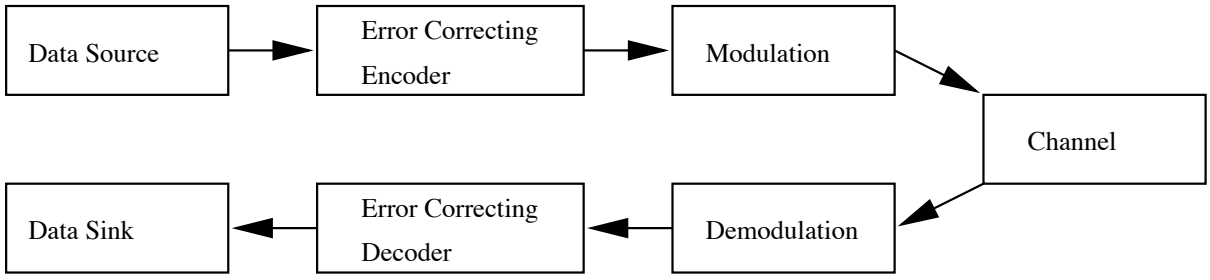

Figure 25: System block diagram

5.1 Biorthogonal Modulation

For the following two subsections we examine the system from Figure 25, with biorthogonal modulation and a singly extended [2] RS code for the error correcting code . The biorthogonal signal set consists of M signals in $\frac{M}{2}$ dimensional space. The first $\frac{M}{2}$ signals in this set are orthogonal, while the remaining signals are each a signed opposite of

[2] A singly extended RS code is an RS code where $N = M$. It is still a maximum distance separable (MDS) code whose distance and error correcting power can be computed in the same fashion as a standard RS code.

a signal from the first $\frac{M}{2}$. Because the transmission of this data requires knowledge of the sign of the transmitted signal, coherent reception is used. The RS decoder has three possible outputs: correct decoding, incorrect decoding, or decoding failure. We treat a packet error as the union of the incorrect and failure events. Thus the probability of a packet error is the probability that we do not decode correctly. For independent noise, efficient expressions for this probability measure can be found in [14], and only require knowledge of the symbol transition probability in the channel.

5.1.1 Biorthogonal Modulation in AWGN

The first channel model under consideration is the AWGN channel with two sided noise power density $\frac{N_0}{2}$. We assume independent noise between symbols and coherent, hard symbol-by-symbol demodulation. Thus, the expression for the symbol error probability for this set can be expressed as:

$$P_{e,s} = (M-2)\int_0^\infty \Phi(z - \sqrt{\frac{2E}{N_0}}(2\Phi(z)-1)^{\frac{M}{2}-2}\frac{1}{\sqrt{2\pi}}e^{\frac{z^2}{2}}dz \tag{61}$$

where E is the energy in one symbol and F is the lower tail Gaussian integral function. Once the transition probability for each symbol is obtained, we obtain packet error probabilities from [14] and show the results in Figure 26.

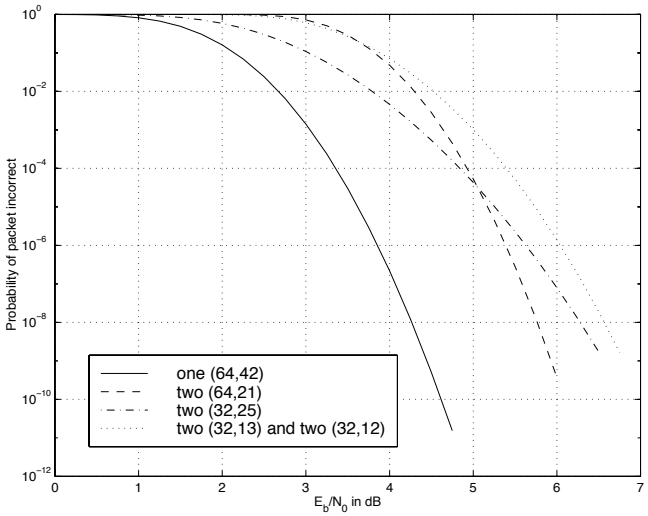

Figure 26: Packet error probability of biorthogonal RS symbols in AWGN.

To examine the bit error probability (BER) of the system, we must examine what happens when a vector of received symbols fails to decode. If we use the bad received vector as our decoded vector we are assured of at least t symbol errors. There are two different types of symbol error: one that errors to an adjacent orthogonal symbol (with probability P_{e1}) and one that errors to an antipodal signal (probability P_{e2}). Without

loss of generality, we can concentrate on the first bit of the first symbol. We make a bit error every time we error to an antipodal symbol ($e2$), and a fraction $\frac{M-2}{2}$ of the time when we make an error of the first kind ($e1$). We can see that $P_{e1} = \frac{P_{e,s}-P_{e2}}{M-2}$, and the overall bit error probability is derived as follows:

$$\begin{aligned} P_{e,b} &= P\{\text{First bit in error} \cap \text{at least } t \text{ symbols of remaining } n-1 \text{ in error}\}, \\ &= P_{fb} P\{t \text{ of } n-1 \text{ in error}\}, \\ &= P_{fb} \sum_{e=t}^{n-1} \left(\begin{array}{c} n-1 \\ e \end{array} \right) (P_{e,s})^e (1-P_{e,s})^{n-1-e}. \end{aligned} \tag{62}$$

where

$$\begin{aligned} P_{fb} &= P_{e,s}(\tfrac{M-2}{M} P_{e1} + P_{e2}), \\ &= P_{e,s}(\tfrac{P_{e,s}}{2} + \tfrac{P_{e2}}{2}). \end{aligned} \tag{63}$$

The expression for P_{e2} for the biorthogonal signal set is as follows:

$$P_{e2} = (M-2) \int_0^\infty F_s(-r)[F_n(r) - F_n(-r)]^{\frac{M}{2}-2} f_n(r) dr, \tag{64}$$

with

- $f_s(x) = \frac{1}{\sigma\sqrt{2\pi}} e^{-\frac{1}{2\sigma^2}(x-\sqrt{E})^2}$,
- $F_s(s) = 1 - Q(\frac{x-\sqrt{E}}{\sigma})$,
- $f_n(x) = \frac{1}{\sigma\sqrt{2\pi}} e^{-\frac{1}{2\sigma^2}(x)^2}$,
- $F_n(x) = 1 - Q(\frac{x}{\sigma})$.

This analysis allows us to examine the bit error probability for the considered system, as shown in Figure 27.

We note that at the desired 10^{-8} BER, the best code is one that transmits all the data bits in a single codeword. While the single transmission may be the best scheme for our error requirement, we must also note that the lines for the scheme that transmits 2 (64,21) codewords and the scheme that transmits a single (64,42) codeword are converging. In fact they cross at an error probability that is below our range.

To make a fair comparison we must note that the above codes have different bandwidth requirements. For a fixed bandwidth comparison we add a spreading factor, q, to make the system bandwidth $W_s = 10^7$Hz, and we illustrate the results in the P/J plot of Figure 28.

We observe that for a bandwidth constrained system, the scheme which transmits a single (64,42) codeword also has better performance than the other schemes. We note that these traces look remarkably similar to the previous comparison. In fact they are merely shifted by a constant. While the system of 2 (64,21) codes may have a higher un-spread bandwidth requirement, by selecting $q = \frac{10^7}{W}$, where W is the un-spread signal set bandwidth, we force the P/J modifications to merely be a constant multiplier: $\frac{P}{J} = \frac{E_b}{N_0}\frac{R}{W_s} = \frac{E_b}{N_0}\frac{R}{Wq} = \frac{E_b}{N_0}\frac{R}{10^7}$.

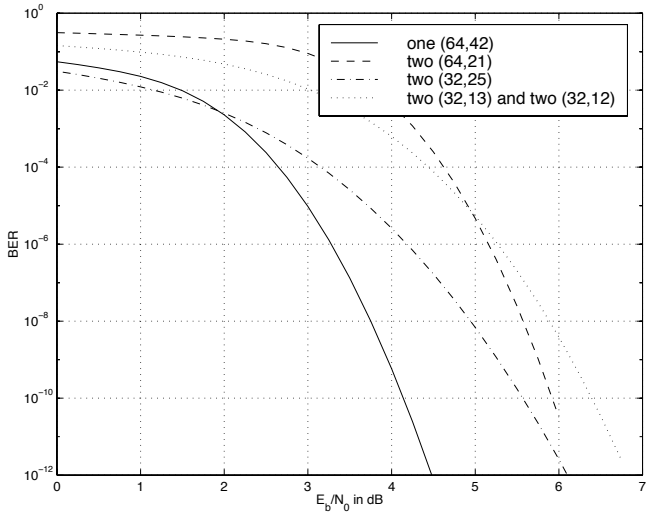

Figure 27: Bit error probability for biorthogonal modulated RS symbols in AWGN.

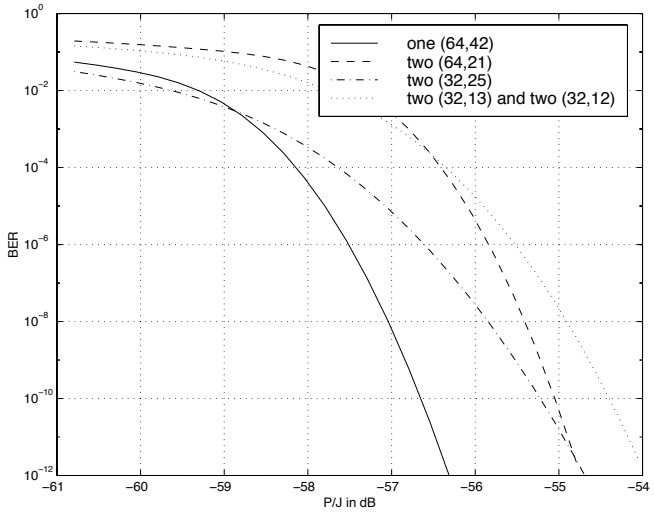

Figure 28: Bit error rate for biorthogonal modulated RS symbols in AWGN (bandwidth normalized).

5.1.2 Biorthogonal Modulation in Rayleigh Interference

The next channel model under consideration is that of a slowly fading channel, modeled in Figure 29. This channel contains a multiplicative, fading element in addition to the additive noise of the previous section. We assume the channel is slowly varying, that is the fading element, α, is constant over a modulation symbol interval.

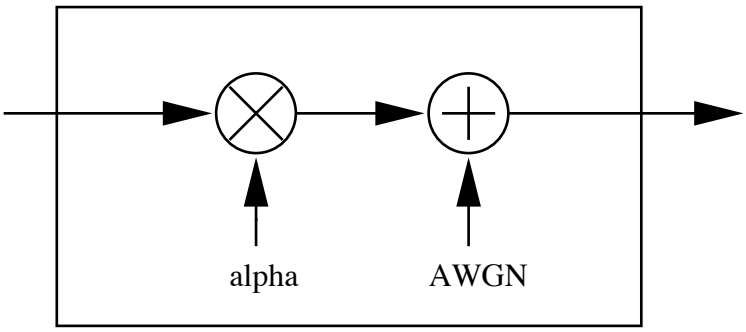

Figure 29: Rayleigh faded channel

For a known fading level, α, the distribution of the output is Gaussian. To derive the average symbol error probability, we examine the output of the energy correlators in the receiver. In the optimum receiver, there are $\frac{M}{2}$ energy correlators, corresponding to the possible $\frac{M}{2}$ dimensions, where the remaining $\frac{M}{2}$ outputs are differentiated by their sign. We denote the output of correlator j to be r_j. Thus, the decision rule is to select the signal whose energy correlator is of largest magnitude. We choose the sign of the transmitted signal to be the same sign as the selected energy correlator's output. The event that we choose correctly is the event that the output of the correct correlator is of the correct sign and largest amplitude, averaged over the distribution of α. For our system we let α be Rayleigh distributed, although other fading models exist the Rayleigh distribution is perhaps the most commonly used. The probability of the incorrect event is

$$P_{e,s} = 1 - \int_{\alpha=0}^{\infty} \int_{r_0=0}^{\infty} f_s(r_0)[F_n(r_0) - F_n(-r_0)]^{\frac{M}{2}-1} dr_0 f_\alpha(\alpha) d\alpha, \tag{65}$$

where the following are defined:

- $f_s(x) = \frac{1}{\sigma\sqrt{2\pi}} e^{-\frac{1}{2\sigma^2}(x-\alpha\sqrt{E})^2}$,
- $F_s(s) = 1 - Q(\frac{x-\alpha\sqrt{E}}{\sigma})$,
- $f_n(x) = \frac{1}{\sigma\sqrt{2\pi}} e^{-\frac{1}{2\sigma^2}(x)^2}$,
- $F_n(x) = 1 - Q(\frac{x}{\sigma})$,
- $f_\alpha(x) = \frac{\alpha}{a^2} e^{\frac{-\alpha^2}{2a^2}}$.

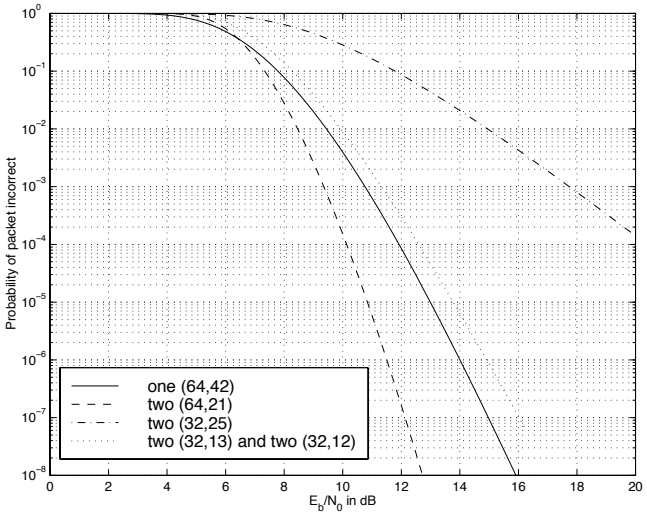

Figure 30: Packet error rate for biorthogonal modulated RS symbols in Rayleigh fading.

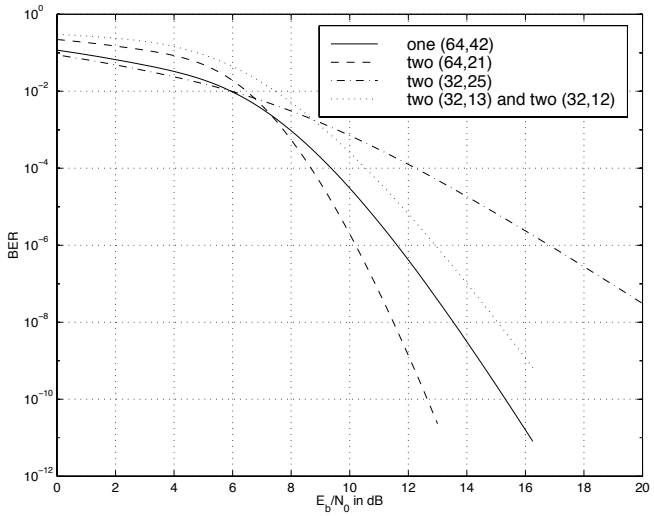

Figure 31: Bit error rate for biorthogonal modulated RS symbols in Rayleigh fading.

We obtain the results in Figure 30 for our 250 information bit packet, and we do a similar conversion as was done in the AWGN case to examine the bit error rate in the Rayleigh channel (Figure 31).
It is interesting to note that the convergence and crossover alluded to in the AWGN only case has occurred in this case, and the 2 (64,21) codewords have the best performance. This phenomenon will be examined in Section 5.3. Again, if we desire a fair comparison in a bandwidth sense, we must examine the P/J results with a fixed system bandwidth of $W_s = 10^7$Hz, of Figure 32.

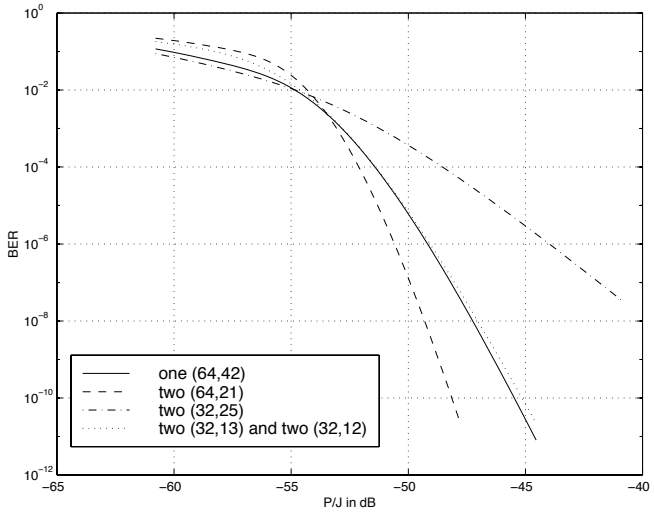

Figure 32: Bit error rate for biorthogonal modulated RS symbols in Rayleigh (bandwidth normalized).

5.2 Orthogonal Modulation with Coherent Detection

For the next two subsections we examine the system from Figure 25, with orthogonal modulation and singly extended RS coding for the error correcting code. Because the transmission of this data does not require knowledge of the sign of the transmitted signal, coherent or non-coherent reception can be used. The RS decoder has three possible outputs: correct decoding, incorrect decoding, or decoding failure. We treat a packet error as the union of the incorrect and failure events. Thus the probability of a packet error is the probability that we do not decode correctly. For independent noise, expressions for this probability measure can be found in [14], and only require knowledge of the symbol transition probability.

5.2.1 Orthogonal Modulation with Coherent Demodulation in AWGN

We consider the case where we transmit orthogonal signals in AWGN (with 2 sided noise power density $\frac{N_0}{2}$), demodulate coherently, and make symbol-by-symbol hard decisions. The expression for the symbol error probability for this signal set can be expressed as:

$$P_{e,s} = 1 - \int_{-\infty}^{\infty} (F_n(r))^{M-1} f_s(r) dr, \tag{66}$$

where

- $F_n(x) = 1 - Q(\frac{x}{\sigma})$,
- $f_s(x) = \frac{1}{\sigma\sqrt{2\pi}} e^{-\frac{1}{2\sigma^2}(x-\sqrt{E})^2}$,

E is the energy in one symbol, and Q is the upper tail Gaussian probability function. Once the transition probability for each symbol is obtained, we obtain packet error probabilities from [14] and show the results in Figure 33. As in previous sections, the bit error

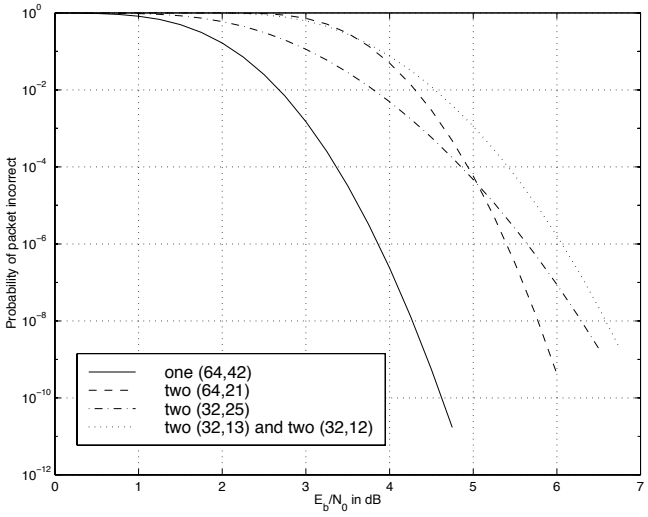

Figure 33: Packet error rate for orthogonal RS modulated symbols in AWGN with coherent demodulation.

conversion, shown in Figure 34, follows:

$$\begin{aligned} P_{e,b} &= P\{\text{First bit in error} \cap \text{at least } t \text{ symbols of remaining } n-1 \text{ in error}\}, \\ &= P_{fb} P\{t \text{ of } n-1 \text{ in error}\}, \\ &= (P_{e,s} \tfrac{M}{2(M-1)}) \sum_{e=t}^{n-1} \begin{pmatrix} n-1 \\ e \end{pmatrix} (P_{e,s})^e (1-P_{e,s})^{n-1-e}. \end{aligned} \tag{67}$$

For a fair comparison we spread to a bandwidth of 10^7Hz, with the results in Figure 35.

5.2.2 Orthogonal Modulation with Coherent Demodulation in Rayleigh Fading

Next we examine the effects of transmitting orthogonal signals in the Rayleigh channel with coherent demodulation. To determine the performance of the system in this case, we

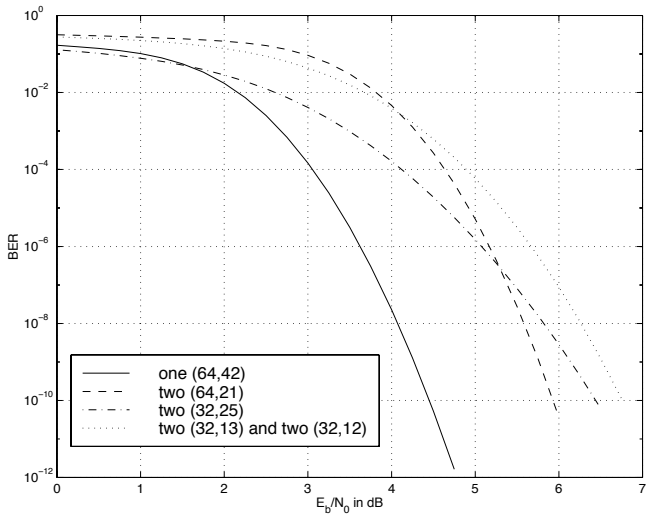

Figure 34: Bit error rate for orthogonal modulated RS symbols in AWGN with coherent demodulation.

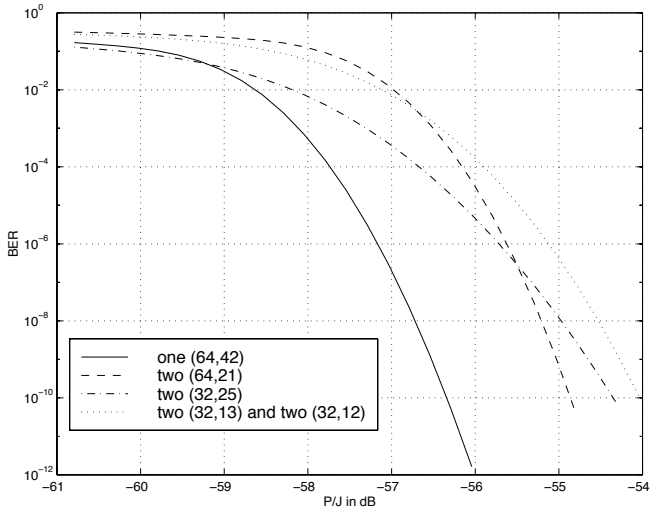

Figure 35: Bit error rate for orthogonal modulated RS symbols in AWGN with coherent demodulation (bandwidth normalized).

note that the channel provides a Rayleigh distributed multiplier, α. If we know the value of α, the system can be analyzed as if it were AWGN with the result being averaged over the distribution of α.

The event that the symbol is incorrect is the event that the magnitude of the output of any of the $M-1$ energy detectors for the non-transmitted signals is greater in magnitude than the detector for the transmitted signal. The probability of this event is

$$P_{e,s} = 1 - \int_{\alpha=0}^{\infty} \int_{-\infty}^{\infty} (F_n(r))^{M-1} f_s(r) dr f_\alpha(\alpha) d\alpha, \tag{68}$$

where the following are defined:

- $f_s(x) = \frac{1}{\sigma\sqrt{2\pi}} e^{-\frac{1}{2\sigma^2}(x-\alpha\sqrt{E})^2}$,
- $F_n(x) = 1 - Q(\frac{x}{\sigma})$.
- $f_\alpha(x) = \frac{\alpha}{a^2} e^{\frac{-\alpha^2}{2a^2}}$.

For the results of this analysis we have the packet error rate in Figure 36 and the bit error rate in Figures 37 and 38. We also note that the scheme that transmits the data bits in 2 (64,21) codewords is the best performer. This is the same phenomenon noted in the discussion of biorthogonal signals in the Rayleigh channel.

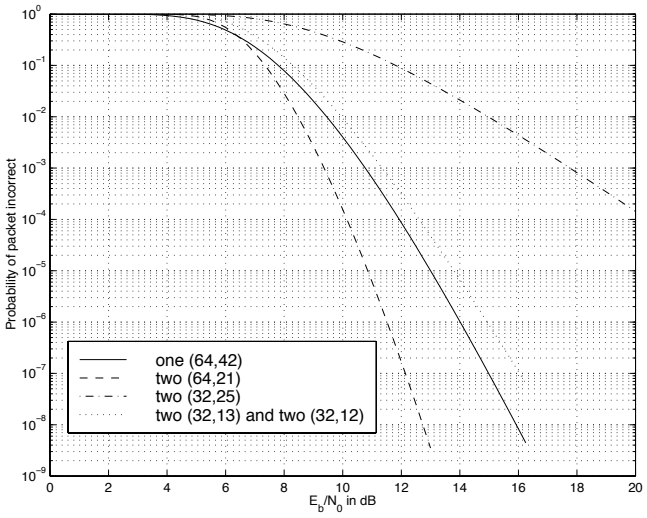

Figure 36: Packet error rate for orthogonal modulated RS symbols with coherent demodulation.

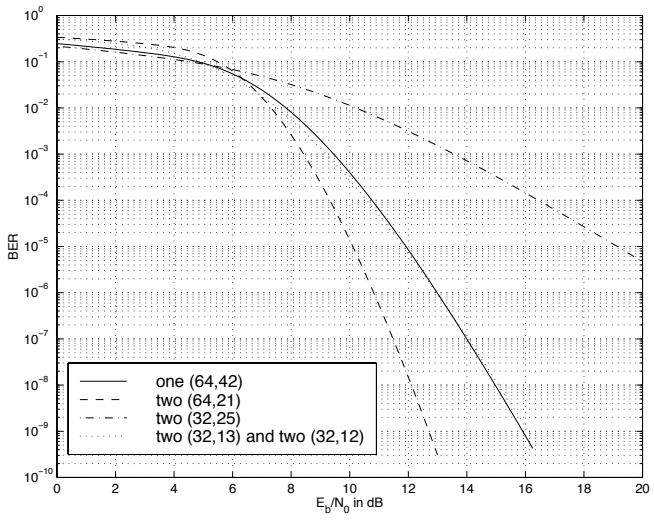

Figure 37: Bit error rate for orthogonal modulated RS symbols with coherent demodulation

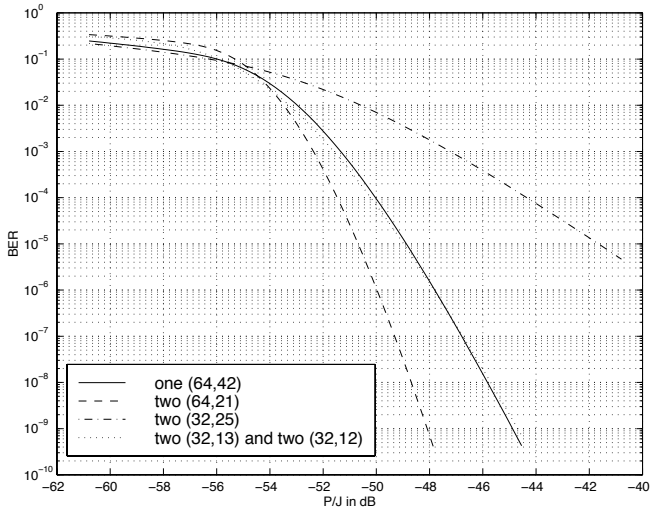

Figure 38: Bit error rate for orthogonal modulated RS symbols with coherent demodulation (bandwidth normalized)

5.3 Optimum Transmission Rates in AWGN and Rayleigh Channels

In Sections 5.1.2 and 5.2.2 we noted that there was a crossover in performance curves between a single (64,42) codeword and 2 (64,21) codewords. We can find an explanation for this phenomena by examining the power required for a given BER for different rates. By examining Figure 39, it is obvious that the best rate choice to minimize power consumption for biorthogonal signals exists at different rates for different channels. We can see that for the AWGN channel the choice of rate $\frac{42}{64}$ is nearly optimal, and this rate does not perform as well as a rate $\frac{42}{128}$ in the Rayleigh channel. Similar results hold true for orthogonal signals. This leads to the conclusion that it is the channel model, not the required BER, that determines the best encoding rate.

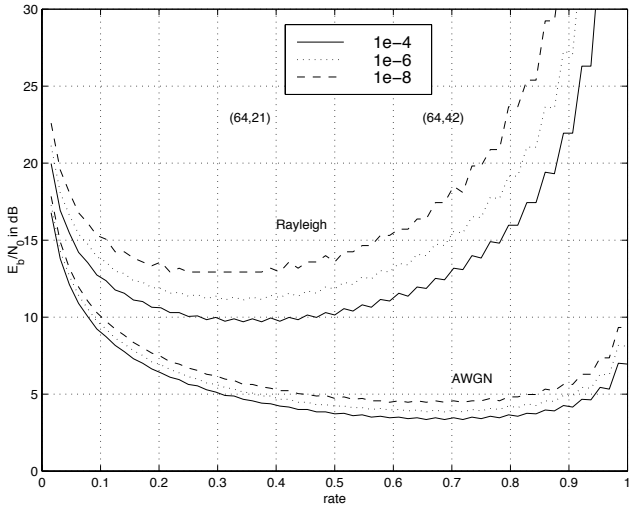

Figure 39: Optimum RS coding rates in AWGN and Rayleigh for biorthogonal modulation

6 Concatenated Reed-Solomon/Convolutional Coding in DS-CDMA for Fading Channel

In this section we consider concatenated coding schemes for the reliable transmission over a fading channel. This scheme is also employed by the U.S. NASA standard and uses outer Reed-Solomon (RS) codes and inner convolutional codes. In this system, the convolutional decoder outputs hard quantized code symbols with bursty errors to the RS decoder. Though, the RS decoder is undisturbed by the burst errors within an symbol, the concatenated system is severely degraded by correlated errors among successive symbols. Hence the interleaving between codes needs to take place at the symbol level (not at bit level) to improve performance.

6.1 Single Transmission Coding Schemes

We first consider transmission of a single stream of data.

6.1.1 System Model

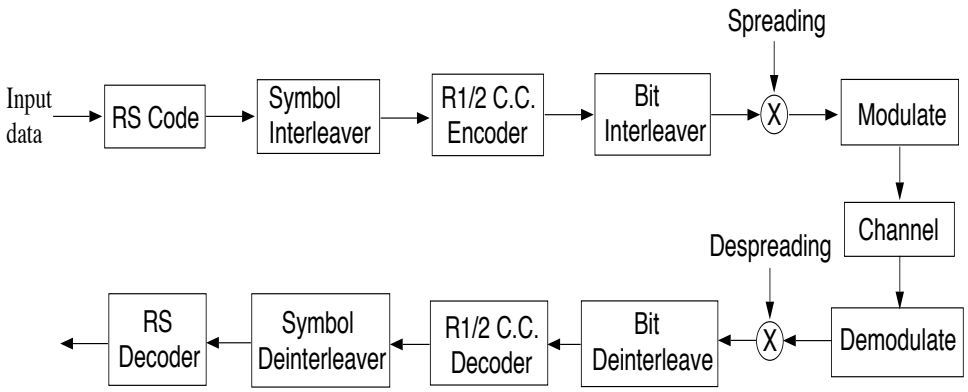

Figure 40: System Model

The data stream here is 256 bits/packet and has to be transmitted within 30 seconds. The bit error rate is down to the 10^{-8}. In other words, the signal requires high reliability, low data rate and a delay of 30 seconds is acceptable. Thus we can use very low rate code to protect the signal. An outer (63,43)RS code and a rate 1/2 convolutional code with constraint length 5 is employed. In this case, symbol interleaver is redundant but bit interleaver can significantly improve the performance. Spreading is made to achieve a 10MHz chip rate and then transmit the signal through the channel.

If a (32,26)RS code and a (31,25)RS code are used for the outer code, the symbol interleaver would break up the correlation between symbols and would improve the performance compared to the one without symbol interleaver. Different rates of coding schemes can be used as long as the total transmition bandwidth is fixed at 10MHz.

6.1.2 Simulation Approach

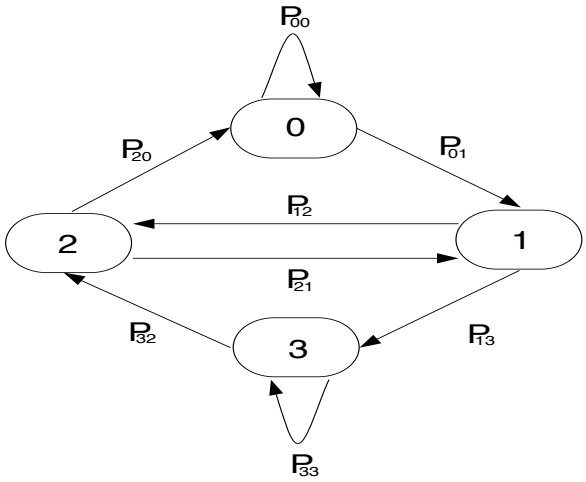

Figure 41: Markov model for (2,1,3) code

The bit error probability under investigation is down to 10^{-8}. Which means that at least 10^{11} bits must be transmitted through the channel. The process of generating the fading channel variables needs two FFTs and also the Viterbi decoding algorithm is very time consuming. It is almost impossible or too costly to do this kind of simulation. A Markov model, proposed by Chao and McEliece [15], is applied to approximate the burst error statistics of the output of the Viterbi decoder. The model proposed by Chao and McEliece is only good for discrete memoryless channel. A modification of the model is proposed here to make it applicable for memoryless channel, fast fading channel and slow fading channel.

6.1.3 Markov Chain Model for the output Statistics of Viterbi Decoder

The output of the Viterbi algorithm is a maximum-likelihood path through the trellis diagram. The Markov model developed by Chao and McEliece is a approximation of the convolutional code's state diagram. An example of rate 1/2 and constraint length 3 convolutional code is shown in fig 41. As we know, if K is the constraint length, this model has the same 2^{K-1} states as the encoder and it grows exponentially as the memory of the encoder increases. In our system, a rate 1/2 convolutional code of constraint length 5 is employed. This convolutional code encoder has 16 states and thus the parameters needed for our Markov model are as follows:

$$\begin{bmatrix}
P_{0,0} & 0 & 0 & 0 & 0 & 0 & 0 & 0 & P_{0,8} & 0 & 0 & 0 & 0 & 0 & 0 & 0 \\
P_{1,0} & 0 & 0 & 0 & 0 & 0 & 0 & 0 & P_{1,8} & 0 & 0 & 0 & 0 & 0 & 0 & 0 \\
0 & P_{2,1} & 0 & 0 & 0 & 0 & 0 & 0 & 0 & P_{2,9} & 0 & 0 & 0 & 0 & 0 & 0 \\
0 & P_{3,1} & 0 & 0 & 0 & 0 & 0 & 0 & 0 & P_{3,9} & 0 & 0 & 0 & 0 & 0 & 0 \\
0 & 0 & P_{4,2} & 0 & 0 & 0 & 0 & 0 & 0 & 0 & P_{4,10} & 0 & 0 & 0 & 0 & 0 \\
0 & 0 & P_{5,2} & 0 & 0 & 0 & 0 & 0 & 0 & 0 & P_{5,10} & 0 & 0 & 0 & 0 & 0 \\
0 & 0 & 0 & P_{6,3} & 0 & 0 & 0 & 0 & 0 & 0 & 0 & P_{6,11} & 0 & 0 & 0 & 0 \\
0 & 0 & 0 & P_{7,3} & 0 & 0 & 0 & 0 & 0 & 0 & 0 & P_{7,11} & 0 & 0 & 0 & 0 \\
0 & 0 & 0 & 0 & P_{8,4} & 0 & 0 & 0 & 0 & 0 & 0 & 0 & P_{8,12} & 0 & 0 & 0 \\
0 & 0 & 0 & 0 & P_{9,4} & 0 & 0 & 0 & 0 & 0 & 0 & 0 & P_{9,12} & 0 & 0 & 0 \\
0 & 0 & 0 & 0 & 0 & P_{10,5} & 0 & 0 & 0 & 0 & 0 & 0 & 0 & P_{10,13} & 0 & 0 \\
0 & 0 & 0 & 0 & 0 & P_{11,5} & 0 & 0 & 0 & 0 & 0 & 0 & 0 & P_{11,13} & 0 & 0 \\
0 & 0 & 0 & 0 & 0 & 0 & P_{12,6} & 0 & 0 & 0 & 0 & 0 & 0 & 0 & P_{12,14} & 0 \\
0 & 0 & 0 & 0 & 0 & 0 & P_{13,6} & 0 & 0 & 0 & 0 & 0 & 0 & 0 & P_{13,14} & 0 \\
0 & 0 & 0 & 0 & 0 & 0 & 0 & P_{14,7} & 0 & 0 & 0 & 0 & 0 & 0 & 0 & P_{14,15} \\
0 & 0 & 0 & 0 & 0 & 0 & 0 & P_{15,7} & 0 & 0 & 0 & 0 & 0 & 0 & 0 & P_{15,15}
\end{bmatrix}$$

Different training sequences are needed for different E_b/N_0. And a reasonable long sequence of training data is necessary for the Markov model to reach saturation.

Though, this model is not strictly accurate, computer simulation result shows that this approximation is good for concatenated coding scheme with Reed-Solomon code as outer code.

In the fast fading channel, if the coherent time is so small that we can treat this channel as memoryless channel. Than, this model is applicable. But, if the coherent time is large, which is the case for slow fading channel. Both error and correct sequence come in burst. The problem with the first order Markov model is that the transition only depends on the present state regardless of the highly correlated channel characteristics. The model obtained by the training sequence is the average of the error bursts and makes no effort in describing the bursty errors caused by deep fade. The model would under estimate the bit error rate owing to the outer Reed-Solomon have the capability to correct most of the errors if the model fail to reflect the deep fade caused by the slow fading channel.

To preserve the deep fade effect caused by the slow fading channel. We can do some modification by referring to the trellis diagram in fig 42. Let's assume all zero sequence is transmitted. Once the received sequence deviated from the all zero path, a variable is justified to prevent it from merging back so quickly. In other word, the probability of staying in error burst once it deviates from the correct path is larger than the previous model. In this way, the model can more faithfully describe the slow fading channel characteristics. And this variable is a function of the velocity between transmitter and receiver.

6.2 Performance in AWGN and Rayleigh fading channel

Fig 43 and fig 44 are the simulation results of the AWGN channel and Rayleigh fading channel. For AWGN channel, there is a cross over at BER=$2 * 10^{-4}$, and for Rayleigh fading channel the cross over occurs at BER=$3*10^{-3}$. It is obvious that the Reed Solomon outer code has a significant effect on the Rayleigh fading channel. It brings down the bit error rate much faster then using the convolutional code alone.

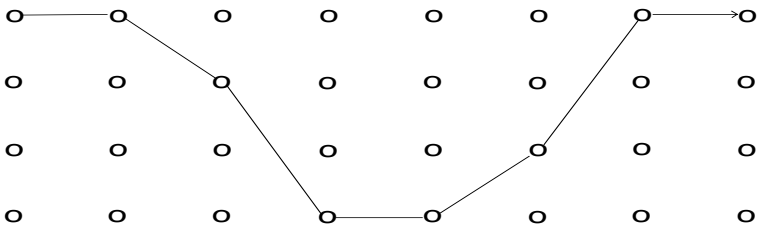

Figure 42: Trellis diagram

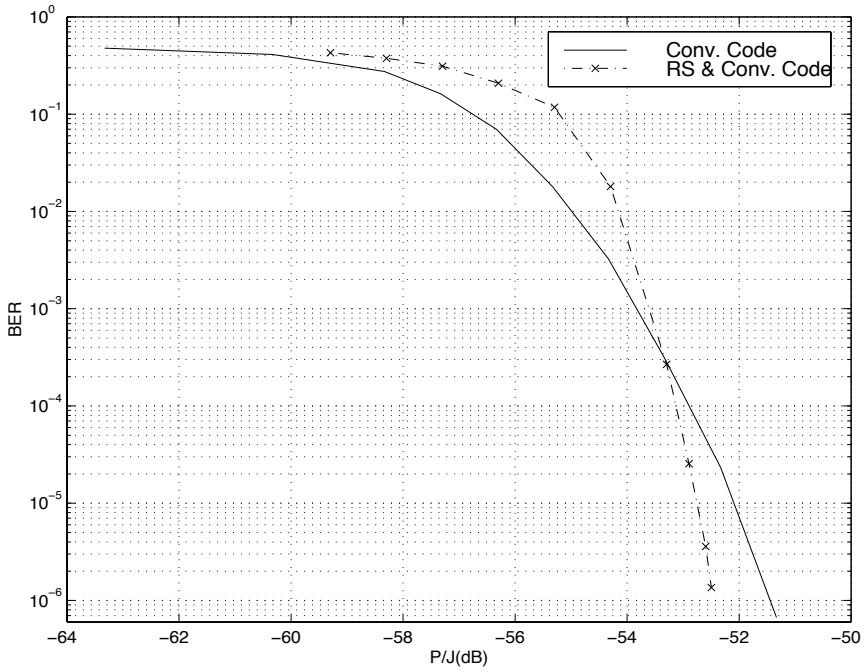

Figure 43: Performance in AWGN Channel

6.3 Performance over frequency selective fast fading channel with Rake receiver

The bandwidth for the DS spread spectrum is much greater than the coherence bandwidth ($\triangle f_c$) of the channel. This kind of wide-band signal will have the ability to resolve the multi-path components and, thus, provide the receiver with several independently fading path signals. If the bandwidth of the signal is W, then, the time resolution is $1/W$. Consequently, with multipaths that have a separation of $1/W$ seconds would be resolvable by the Rake receiver and thus the diversity techniques can be employed to overcome the severe consequences of fading. This kind of frequency selective channel can be modeled as tapped delay line model with statistically independent time-variant tap weights.

Let's assume that we have the Lth-order diversity and perfect channel information, i.e., we are able to estimate the fading level(tap weight) in each tap with no error. The optimum receiver for this wide-band signal is Rake receiver with maximal ratio combining.

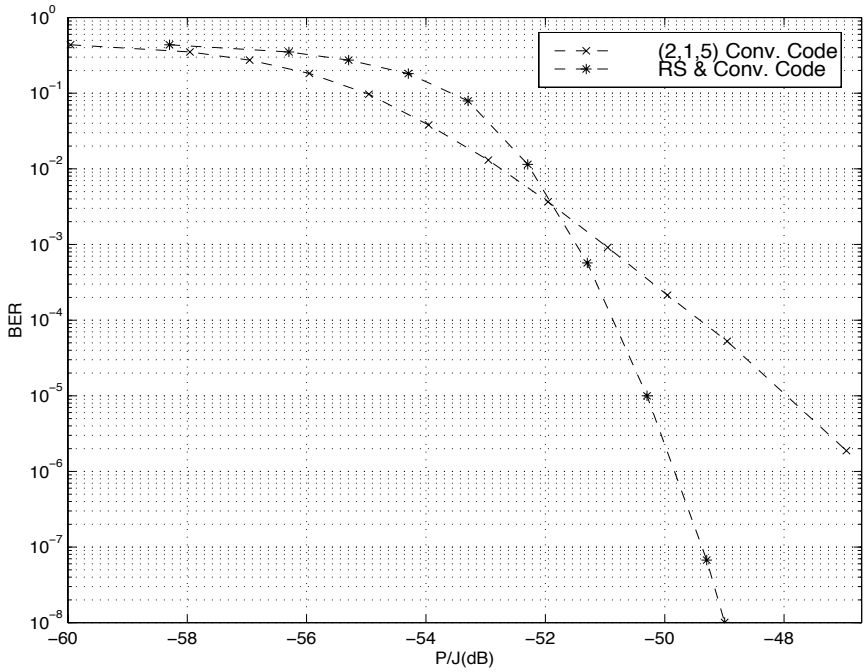

Figure 44: Performance in Rayleigh fading Channel

In our simulation, two empirical channel models are used. Where ALD stands for American Legion Drive, and it is a suburban area with 5 independent fading paths. And PINEST stands for Pine Street in New York City, and it contains 12 independent fading paths. The carrier frequency (f_c) is 33MHz, transmition bandwidth(W) is 10MHz and the vehicle velocity is 108 km/h. The coherence time is inversely proportional to the relative velocity between transmitter and receiver. While the relative velocity is 108 km/h, the coherence time is approximately 0.05 second. As you can see in fig 45, interleaving gain for ALD channel at bit error rate 10^{-6} is about 0.5 dB. For PINEST channel at the same error rate, a gain of 0.3 dB is observed.

In fig 46, the Rayleigh fading channel can be considered as a single path fading model. The ALD and PINEST model can be considered as 5 and 12 paths model. From the graph, we can see that the diversity technique does improve the performance. For the Rayleigh fading channel, it takes less than 3.2 dB for the concatenated coding to bring the bit error probability from 10^{-2} to 10^{-8}. While it takes only approximately 2.1 dB for the ALD and PINEST channel to bring down the same amount of the error rate with diversity technique. For the PINEST 12 paths model with concatenated coding scheme, a 0.7 dB gain is observed relative to the ALD channel model at bit error rate equal to 10^{-8}, while the ALD 5 paths channel model also has a 1.5 dB gain over the single path model.

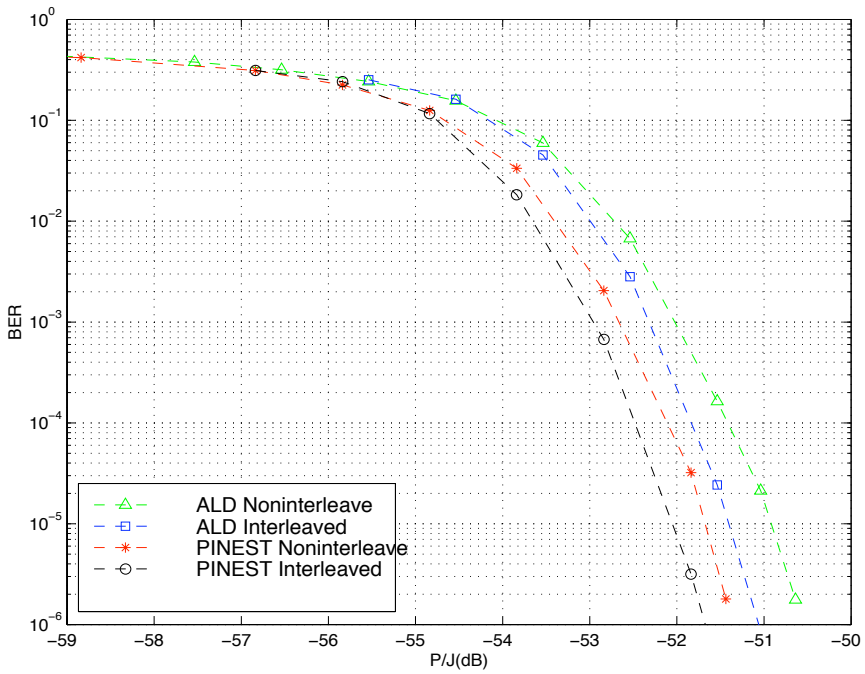

Figure 45: Gain Achieved by Interleaver

6.4 Performance over frequency selective slow fading channel with Rake receiver

In the slow fading channel, the coherence time is much larger than a symbol duration. The fading level would remain the same for a significant long period and has a devastating effect on the outer Reed-Solomon code. Let's consider the extreme case where the relative velocity between transmitter and receiver is 0 m/s. The assumption made here is that the fading level is a constant through the whole packet duration, but is independent from the next packet.

It is obvious from fig 47 and fig 48 that the performance of the concatenated coding in the slow fading channel without power control is significantly worse than the performance in the fast fading channel. This is easily understand by the diversity offered by the fast fading which gives the receiver more information about the transmitted signal. But if we take a careful look both in fig 47 and fig 48, we can find out that in the relative low signal to noise ratio(SNR), the slow fading channel outperformance the fast fading channel. This is because in the relative low SNR, if the packet happens to go through a good channel condition, the whole packet gets through. And thus greatly improve the error probability in the low SNR region. On the contrast, in the relative high SNR region. If the slow fading channel jumps into a deep fade, the whole packet is gone. While for the fast fading channel, the deep fades are scattered all over the transmition interval and thus corrected by the outer Reed-Solomon code.

fig 47 and fig 48 are made in same scale, it is easy to tell that the PINEST channel with 12 multipaths quickly brings down the error probability even in the slow fading channel. While the ALD channel with 5 multipaths still suffers from the deep fade effect caused

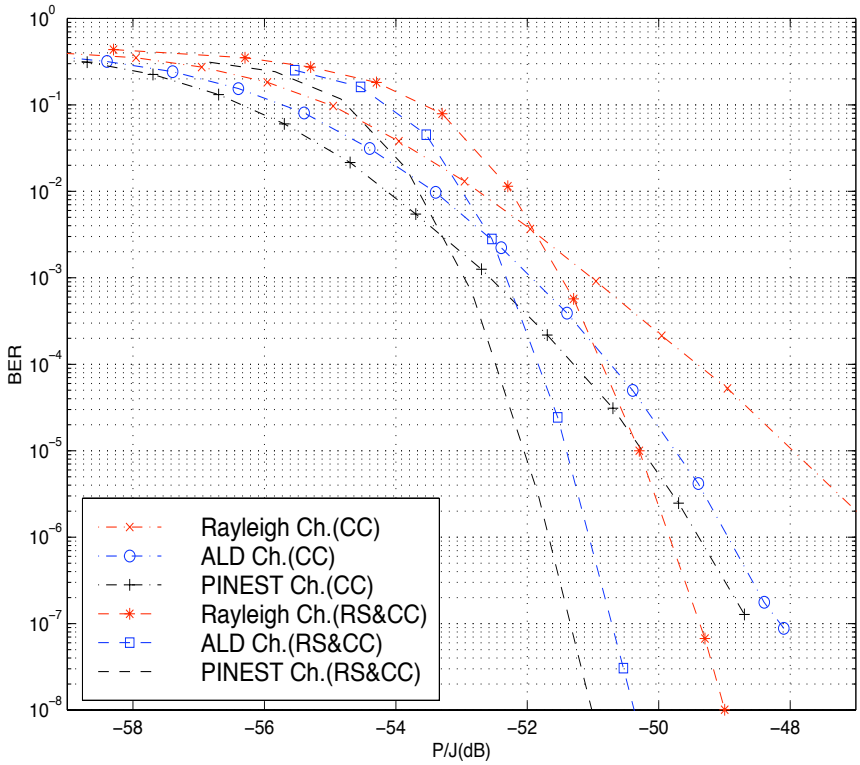

Figure 46: Performance over multipaths fast fading channel with Rake receiver

by the slow fading effect.

Now, let's compare the convolutional code alone with the concatenated coding. In the PINEST channel, if the convolutional code is the only coding scheme used. We can tell from fig 47 that the performance for the fast fading channel and slow fading channel is almost the same. Why is that so ? Let's take a look at the multipath strength of this channel.

	1st	2nd	3rd	4th	5th	6th	7th	8th	9th	10th	11th	12th
PINEST(dB)	-5.8	-11.6	-4.2	-0.8	0	-5.5	-9.2	-2.8	-27.7	-8.6	-16	-36.7
ALD (dB)	0	-4.5	-16.1	-25.3	-25.3							

In the PINEST channel, the signal strength is evenly distributed among the 12 paths. Unlike the ALD channel, only the 1st and the 2nd path dominate. Owing to this characteristic, the multipath diversity has overcome the slow fading effect. In other words, it is not likely that the twelve paths will go through the same deep fade simultaneously. Thus the performance in slow fading channel is only slightly worse than the fast fading channel. But for the ALD channel, this is not the case. As mentioned above, only the first path and the second path in this channel are not enough to overcome the deep fades caused by the slow fading effect. And thus the convolutional code in the fast fading channel has a gain of approximately 3.5 dB over the slow fading channel at the bit error rate of 10^{-6}.

Now, let's take a look on the concatenated coding scheme. Both fig 47 and fig 48 show

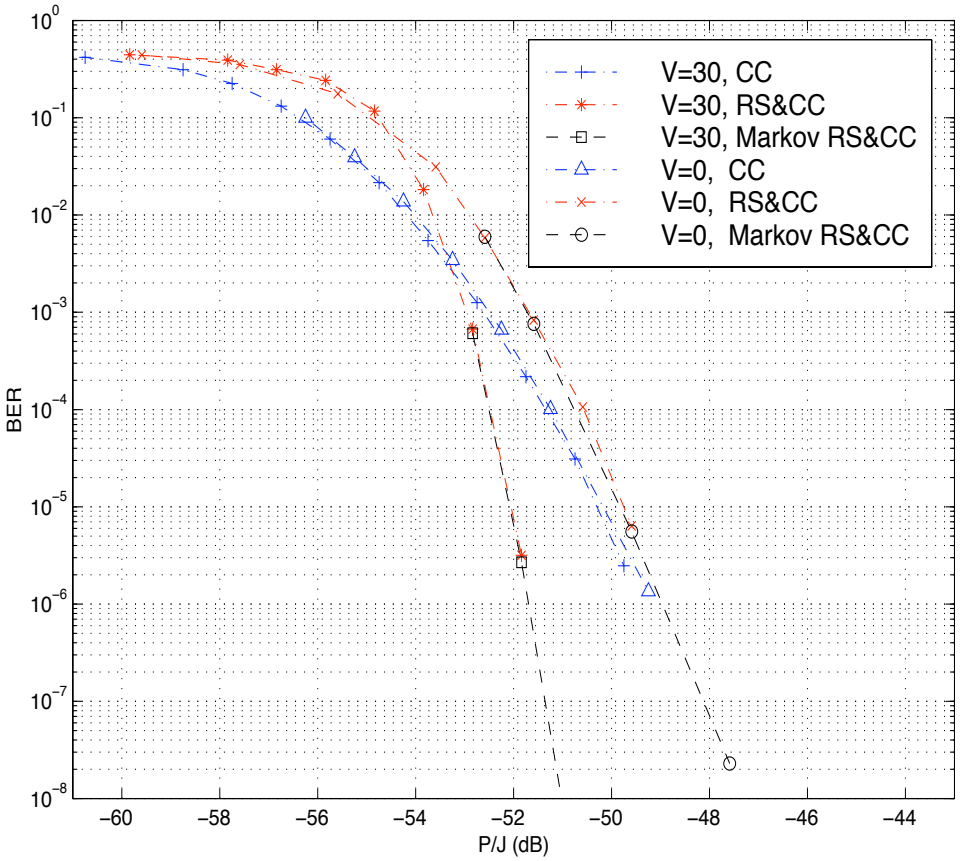

Figure 47: PINEST channel

that the concatenated coding scheme performs well in fast fading channels but is worse than the convolutional code alone in slow fading channel. For the PINEST channel, an expected cross over will occur at around 10^{-6} dB and thus results in the concatenated coding outperform the convolutional code alone.

The Markov model proposed accurately estimated the bit error rate of both the fast fading and slow fading channel. A slight problem arise in the slow fading model. As shown in fig 47, the model performs well in both cases in PINEST channel. But in fig 48 shows that the analysis can't go any further than the 10^{-6} bit error rate in slow fading channel. The main reason for this is that the model is based on the output statistics of the Viterbi decoder. And it is trained directly from the output sequence of the Viterbi decoder. The advantage of this model is that while the outer Reed-Solomon code brings down the bit error rate probability, the inner convolutional code is still in relatively high bit error rate. Thus the model can be trained with much less data then necessary for direct simulation. This is the case in both fast fading channels and slow fading channel in PINEST model. But in ALD channel model, while the concatenated coding reaches the bit error rate of 10^{-6}, the inner convolutional code also gets down to approximately $4 * 10^{-6}$. While the concatenated coding reaches BER of $2 * 10^{-7}$, the convolutional code also reaches BER of $4 * 10^{-7}$. Because the bit error rate for the convolutional code in ALD

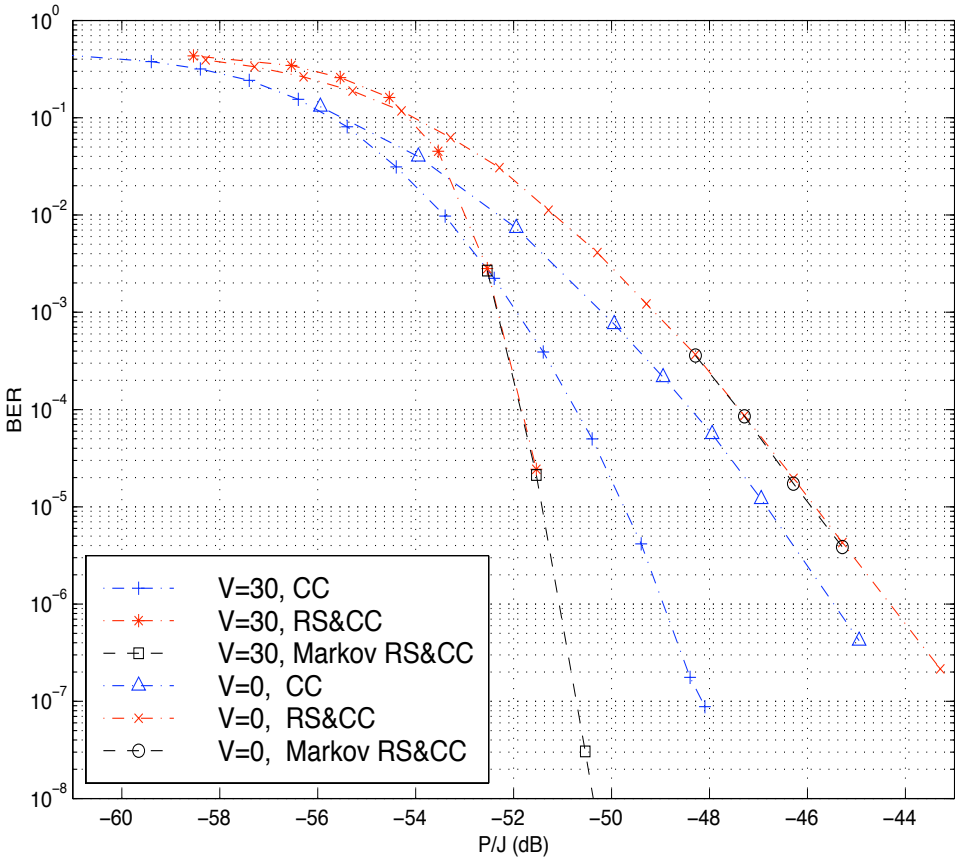

Figure 48: ALD channel

channel almost goes down simultaneously with the concatenated coding scheme. Thus not enough training data can make the model to reach the saturation point. Thus the model can't do any further analysis than a BER of 10^{-6}.

7 Multicast Coding Schemes

Multicast transmission will find increased prominence in future mobile, wireless environments in which different types of data with different quality of service requirements are efficiently transmitted while conserving the limited resources of bandwidth and energy. One major difficulty for this system is transmitter nonlinearities. If a non-constant envelope signal is used, spectral regrowth, intermodulation distortion and amplifier backoff will cause the system to be either bandwidth inefficient or power inefficient. In this report, a comprehensive approach is taken in designing a communication system. Different modulation schemes, device nonlinearities, adjacent channel interference (ACI), and intermodulation distortion will be considered while presenting a means of measuring the total power needed per transmitted bit. This approach will also help determine the optimal amplifier backoff and a bandwidth efficient modulation scheme.

In this report, a brief introduction about the multicast transmission system will be presented in Section 7.1. Transmitter nonlinearities are then discussed in Section 8. In Section 9, modulation schemes and transmitter nonlinearities are considered in comparing total power needed per transmitted bit for a non-constant envelope and a constant envelope system.

7.1 Multicasting

In future mobile communications, there will be various data with different requirements. For example, control data have low data rates and tolerate delays on the order of seconds. However, they are sensitive to errors and hence, require very low error probability. On the other hand, voice information is delay sensitive (e.g. on the order of 20-50ms), but can operate at fairly high error rates (e.g. 10^{-2}). Table 14 is an example of different data types with different service requirements.

Packet Size (Bits)	256	9600	$8 * 10^6$
Bit Error Rate	10^{-8}	10^{-6}	10^{-4}
Packet Duration	30 sec	1 sec	5min
Availability (%)	99	95	90
$R_b(bps)$	8.5333	9.6k	26.7k

Table 14: Different data with various requirements

7.2 System Design

In Fig.49, three different data, $b_i(t)$ where $i = \{1, 2, 3\}$, are to be multicast through the channel. Because of different quality of service requirements, individual levels of protection (forward-error-control (FEC)) are imposed on each data string. Furthermore, orthogonal spreading sequences ($a_1(t)$, $a_2(t)$ and $a_3(t)$) are employed among the different

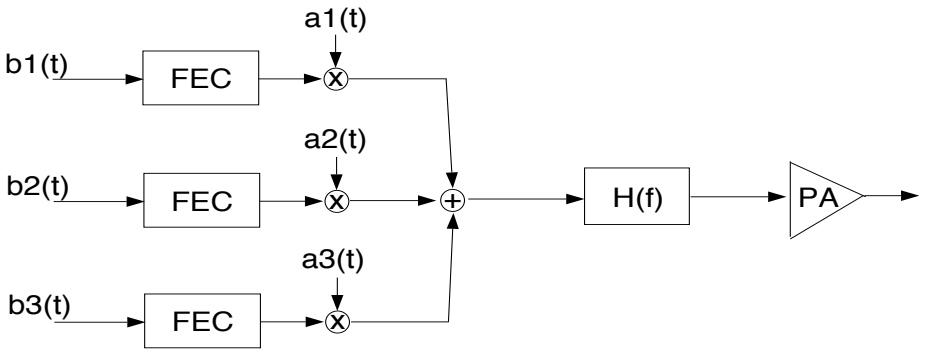

Figure 49: CDMA Multicasting Model

data so that the various data strings can merge into a single carrier without interfering with each other. After combining the different data strings, the signal is then passed through a raised-cosine pulse-shaping filter and a nonlinear power amplifier.

Binary phase-shift keying (BPSK) modulation is chosen to simplify the problem of combining data strings in the multicast transmission. The disadvantage of this modulation scheme is that it is a non-constant envelope signal. Spectral regrowth and intermodulation are expected with transmitter nonlinearities. Furthermore, the amplifier backoff will force the transmitter to operate in a less energy efficient way. In the following section, a way of measuring the total power needed per transmitted bit while taking into account the device nonlinearity is proposed, where total power encompasses both the radiated power (P_r) and the power that has been converted into heat (P_{heat}).

$$P_{total} = P_r + P_{heat}. \tag{69}$$

Before measuring the total power needed per transmitted bit, the transmitter nonlinearities are introduced in the following section.

8 Transmitter Nonlinearities

Although linear amplifiers are generally not available, several different classes of amplifiers exist among non-linear amplifiers such as A, B, AB, C, etc. Typically, the more power efficient amplifiers posses greater nonlinearities. However, these nonlinearities distort non-constant envelope signals, which usually have better bandwidth efficiency. Thus, if a non-constant envelope signal is passed through a nonlinear amplifier, spectral regrowth, intermodulation and the amplifier backoff should be considered.

Spectral regrowth is caused by the pulse shape filtering and nonlinearities of the amplifier. This would generate adjacent channel interference, and reduce the bandwidth efficiency. Intermodulation produces inband interference, hence, increasing the noise floor within the transmitted bandwidth. Backoff is introduced by the amplifier nonlinearities while driving in the saturation region, where the amplifier usually has better power efficiency. Signal degradation caused by transmitter nonlinearities while operating in a more power efficient way forces the transmitter to "backoff" the driving range of the amplifier,

therefore, reduces total power needed per transmitted bit. This results in a less power efficient amplifier operation.

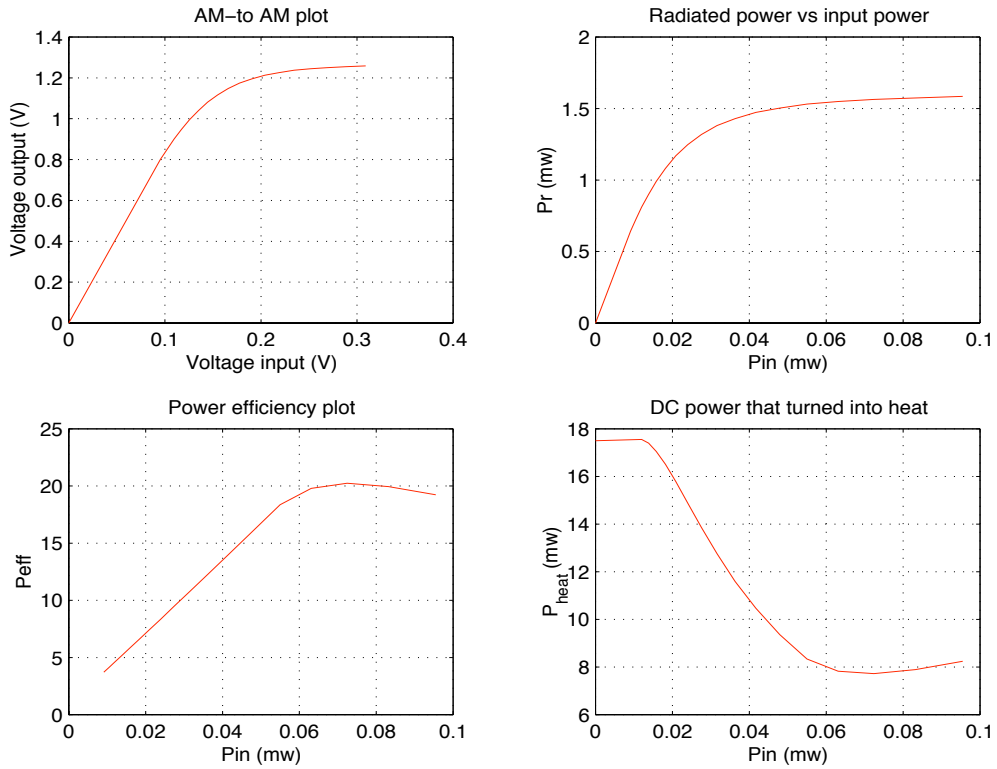

Figure 50: Nonlinear Amplifier

Fig. 50 shows an example of a nonlinear amplifier. The upper left plot is the amplitude-to-amplitude (Am-to-Am) plot for the amplifier. If the power amplifier is driven at a region below 0.12V, the distortion introduced by the amplifier will be small because this region is more linear. From the lower left power efficiency plot and lower right DC power consumption plot (DC power that turned into heat), it can be seen that the amplifier is not very efficient while operating in this more linear region. On the other hand, if the amplifier is driven in the saturation region, the power amplifier is more power efficient, but the degradation of the signal due to nonlinearities will be significantly large. Therefore, the backoff of the amplifier represents a tradeoff between signal distortion and power consumption which can be evaluated by the overall power needed per transmitted bit.

Figs. 51 and 52 show the performance of the nonlinear amplifier when operating in different driving regions. Two data streams with different data rates, 256/30 bits per second(bps) and 9600 bps, are combined into a single carrier and transmitted through a bandwidth of $160kHz$. In the upper plots of both figures (Figs. 51 and 52), DC power consumption is not considered. Signal degradation introduced by transmitter nonlinearities is compared with an ideal linear amplifier. In Fig. 51, the signal degradation for both data in the driving range from $-0.2V$ to $0.2V$ is about 0.5 dB at the bit error rate of 10^{-3}, while the degradation for the driving range of $-0.3V$ to $0.3V$ is about 1.2 dB (see

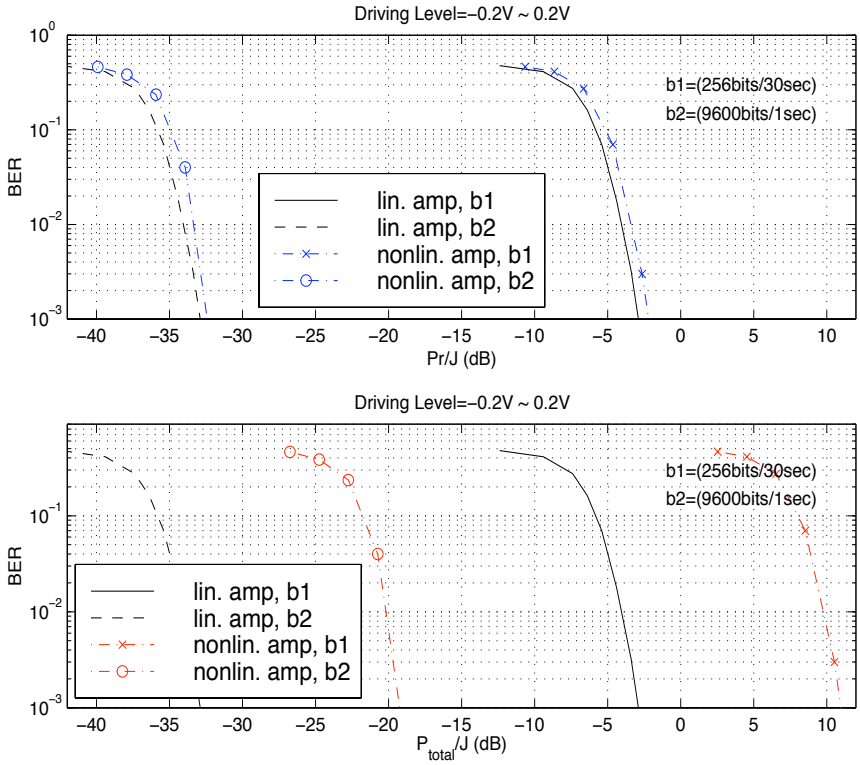

Figure 51: Driving Level=$-0.2V$ to $+0.2V$

Fig. 52).

The lower plots of both figures (Figs. 51 and 52) take into consideration the power that is consumed by the amplifier and transformed into heat. The relationship between power that is drown into the amplifier and power wasted is as follows

$$P_{in} + P_{dc} = P_r + P_{heat}, \tag{70}$$

where P_{in} is the drain power that goes into amplifier from signal source and P_{dc} is the DC power offered by outer source.

In Fig. 53, the overall power needed to transmit a bit for different driving regions are compared for data rates of 256/30 bps. As shown in the plot, the driving range of $\pm 0.3V$ has a lower total power consumption. This is because in the driving range of $\pm 0.3V$, the amplifier is more power efficient. Although the nonlinearities increases as we increase the driving range from $\pm 0.2V$ to $\pm 0.3V$, signal degradation is small and power efficiency dominates the performance.

In the following section, a way of measuring the optimal amplifier backoff and total power needed per transmitted bit is presented.

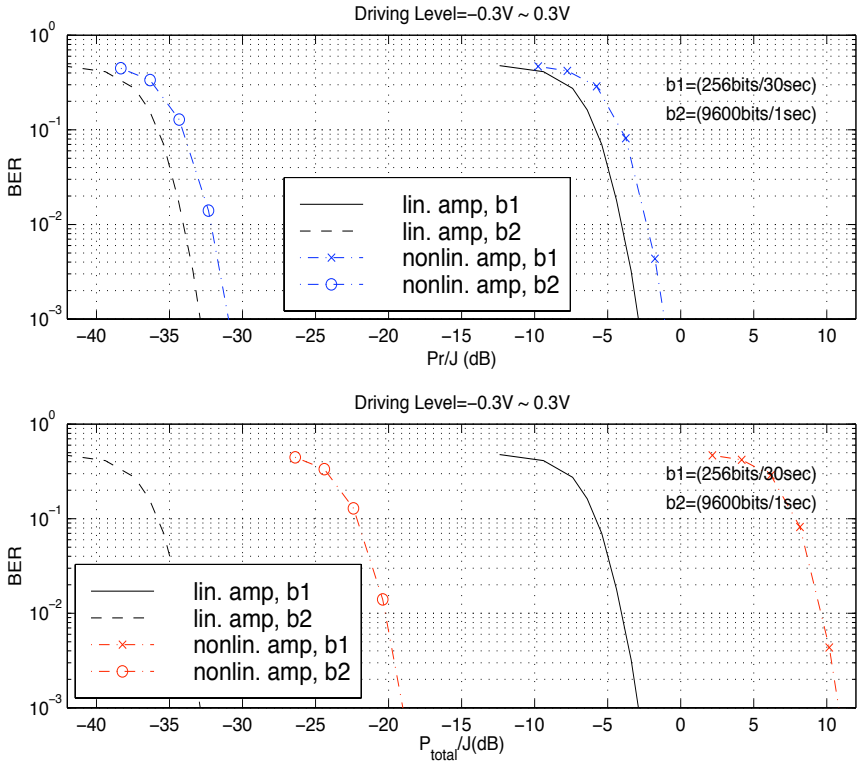

Figure 52: Driving Level=$-0.3V$ to $+0.3V$

9 $\pi/4$-Quadratic-Phase-Shift-Keying ($\pi/4$-QPSK) vs Minimum-Shift-Keying (MSK)

Most mobile radio products are usually designed with power efficient, nonlinear amplifiers, and therefore, it is necessary that the signal to be amplified has a constant envelope or as nearly so as possible. This is because the amplitude fluctuations of the input signal would widen the bandwidth of the output signal (spectral regrowth), and hence, cause increased ACI. Although the non-constant envelope signal has the disadvantage of amplitude fluctuations, it is usually more spectrally efficient, i.e., narrower mainlobe and higher rolloff sidelobes, when compared with a constant envelope signal.

$\pi/4$-QPSK is a modified version of QPSK, which provides greater compatibility with transmitter nonlinearities due to its lower amplitude fluctuations after pulse-shape filtering. In this section, a constant envelope signal structure (MSK) is compared with a nonconstant envelope structure ($\pi/4$-QPSK with raised cosine filter). It is compared through the total signal-to-interference ratio for both of the modulations and the bit error rates.

9.1 $\pi/4$-QPSK

$\pi/4$-QPSK is a form of QPSK modulation in which the QPSK signal constellation is shifted each symbol interval T by 45^o. This restricts the transitions from one symbol to

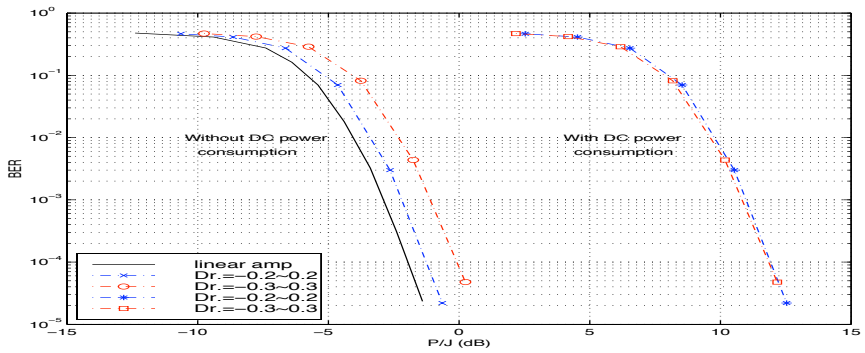

Figure 53: Take the DC power consumption into consideration for different driving levels (256/30 *bits/secs*)

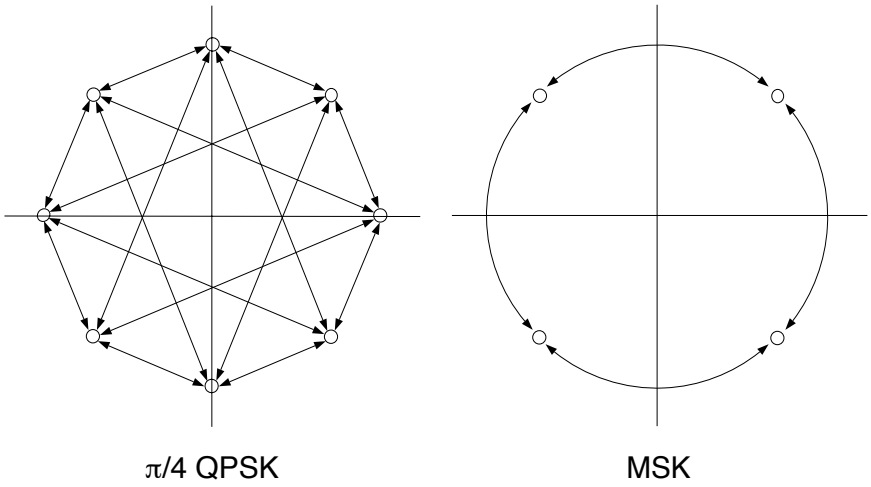

Figure 54: Signal constellation

the next to be $\pm\pi/4$and $\pm 3\pi/4$. By eliminating the $\pm\pi$ transitions of QPSK, the signal after filtering will avoid the origin and thus significantly reduce amplitude variation. Thus the $\pi/4$ QPSK modulation provides the bandwidth efficiency of QPSK, together with a diminished range of amplitude fluctuations. These advantages of $\pi/4$-QPSK led to its adoption for the North American Digital Cellular TDMA standard, Japanese Digital Cellular standard, and the planned new standards for Trans-European Trunked Radio (TETRA) [16].

Fig. 54 shows the signal constellation of $\pi/4$-QPSK. In Fig. 55, the time domain signal (real axis) and its power spectral density are plotted. In the lower plot of Fig. 55, the darker line represents the power spectral density before passing through a nonlinear amplifier. As shown in the plot, the sidelobes rolloff extremely fast after pulse shape filtering. Spectral regrowth is observed after nonlinear amplification (lighter line) which is a major cause for ACI.

9.2 MSK

MSK is a special type of continuous phase frequency shift keying (CPFSK) with a minimum frequency separation (i.e. bandwidth) that allows orthogonal detection. It possesses properties such as a constant envelope and spectral efficiency. These properties make MSK modulation particularly attractive for use in mobile communication systems. For example, Gaussian-filtered MSK (GMSK) modulation has been adopted for GSM, the Pan-European Digital Cellular Standard. Fig. 54 shows the signal constellation of MSK modulation.

In Fig. 56, both the time domain signal (real axis) and the power spectral density are shown. Comparing the main lobe of the $\pi/4$-QPSK with MSK, it is obvious that $\pi/4$-QPSK has a more compact spectrum then MSK before nonlinear amplification. The effects of spectral regrowth and intermodulation distortion caused by transmitter nonlinearities will be discussed in the following subsection.

9.3 Numerical Results

The system to be investigated is an uncoded system with either a $\pi/4$-QPSK non-constant envelope signal or a MSK constant envelope signal, passing through different classes of amplifiers and then an AWGN channel. The bit duration is one bit per second, and two other users are simulated at the adjacent frequencies to create ACI to the desired signal. For $\pi/4$-QPSK, a raised-cosine pulse shaping filter with rolloff factor 0.35 is used. This is a typical rolloff factor that is utilized in the industry. Two types of amplifiers, class AB and F, with different frequency spacing for the adjacent channel users are investigated. Class AB is more linear then class F amplifiers, but it is less power efficient.

In the left plot of Fig. 57, the solid line is the ideal case with a linear amplifier that has 100 percent efficiency, i.e., no power has been converted into heat, and without any ACI. The E_b/N_0 for the ideal case is approximately 7 dB at BER 10^{-3}. As can be seen from the plot, both of the modulations are very inefficient while the driving level is low. Although the amplifier is more linear in this region, most of the power is converted into heat instead of radiated power. For this amplifier, the optimal driving region for $\pi/4$-QPSK is about 0.4V and 0.42V for MSK. Overall, MSK requires lower energy per transmitted bit than $\pi/4$-QPSK for this particular amplifier.

For the right plot of Fig. 57, the adjacent channel power ratio (ACPR[3]) for $\pi/4$-QPSK increases as the amplifier is driven harder into the saturation, while the ACPR for MSK stays constant. This is because the MSK modulation is a constant envelope signal and the amplifier nonlinearities will not increases the ACI. On the other hand, $\pi/4$-QPSK is a non-constant envelope signal and consequently, transmitter nonlinearities increase the signal distortion and cause spectral widening which results in increased ACI. Intermodulation distortion is also caused by transmitter nonlinearities and results in inband interference. Both of the effects are the main reasons that $\pi/4$-QPSK performs worse than MSK.

[3] $$ACPR = 10log\frac{ACI\ power}{signal\ power}$$

With the same frequency spacing for adjacent channel users and an amplifier from class F, both systems perform better in the optimal driving region but worse in the saturation region (see Fig. 58) when compared with class AB amplifier (Fig. 57). The power efficiency of the class F amplifier brings down the total power needed per transmitted bit, but due to the highly nonlinearities while driving in the saturation region, signal distortion degraded the overall system performance. In Fig. 59, adjacent channel users are brought more closer together, and hence, the effect of the ACI is more obvious. As shown in the left plot of Fig. 59, $\pi/4$-QPSK is severely degraded by ACI as the driving range increases. Although the ACI remains the same for MSK for different driving ranges, total power needed per transmitted bit increases after a certain point. This is because the power efficiency drops if we overdrive the amplifier, and thus, increases the total power needed for transmission.

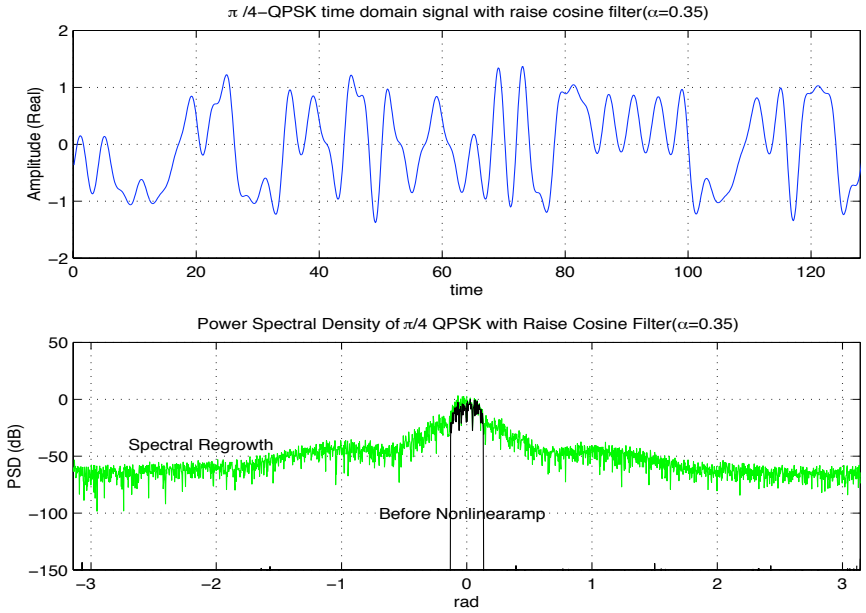

Figure 55: $\pi/4$-QPSK

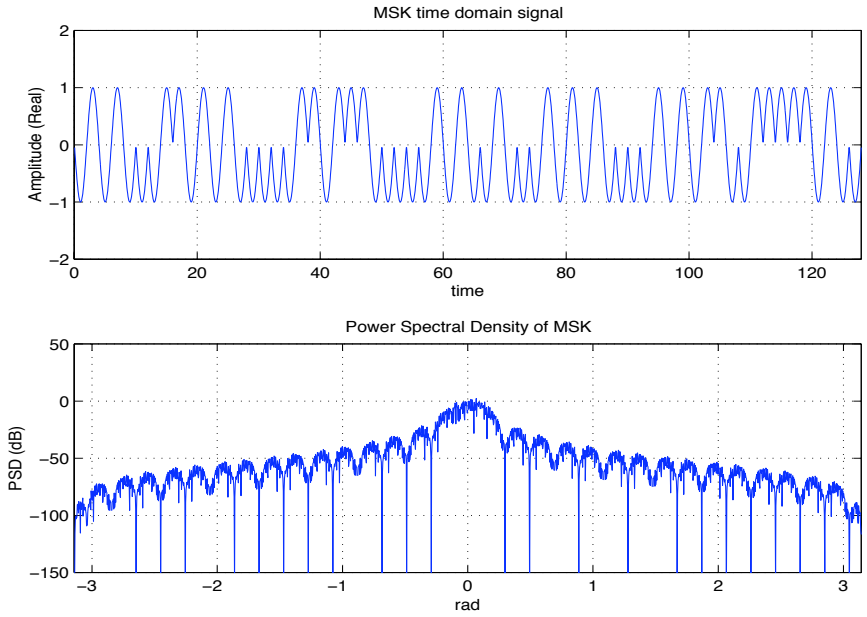

Figure 56: MSK

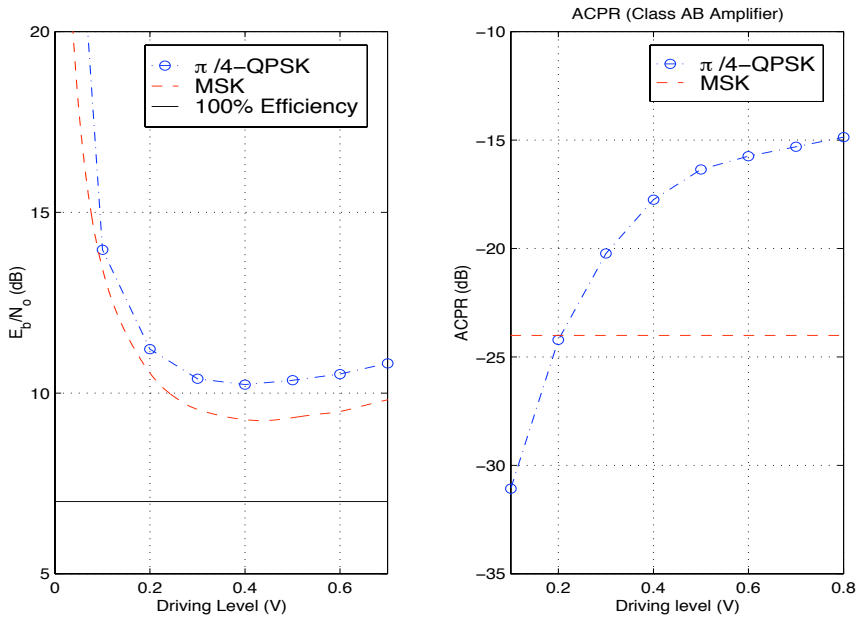

Figure 57: Class AB amplifier with frequency spacing $1.5Hz$ (BER=10^{-3})

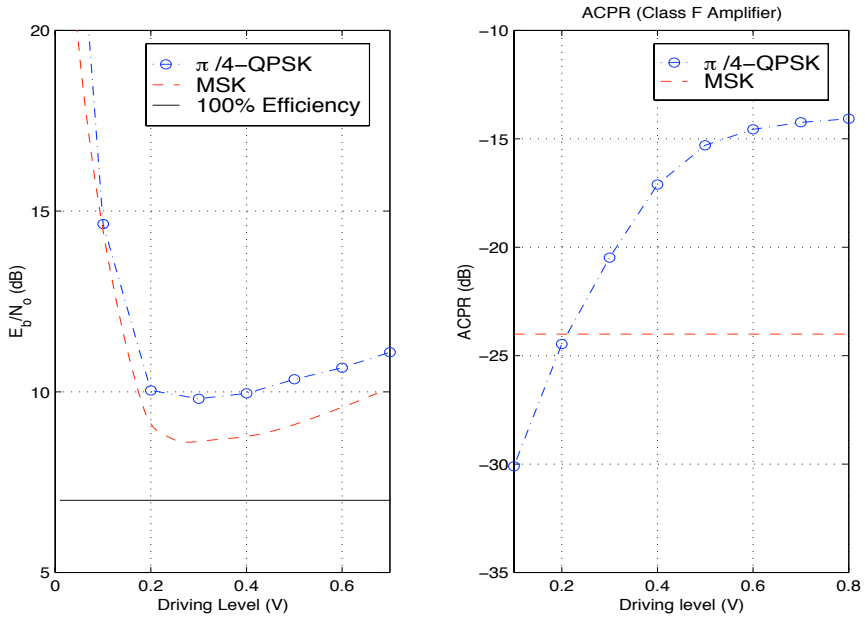

Figure 58: Class F amplifier with frequency spacing $1.5Hz$ (BER=10^{-3})

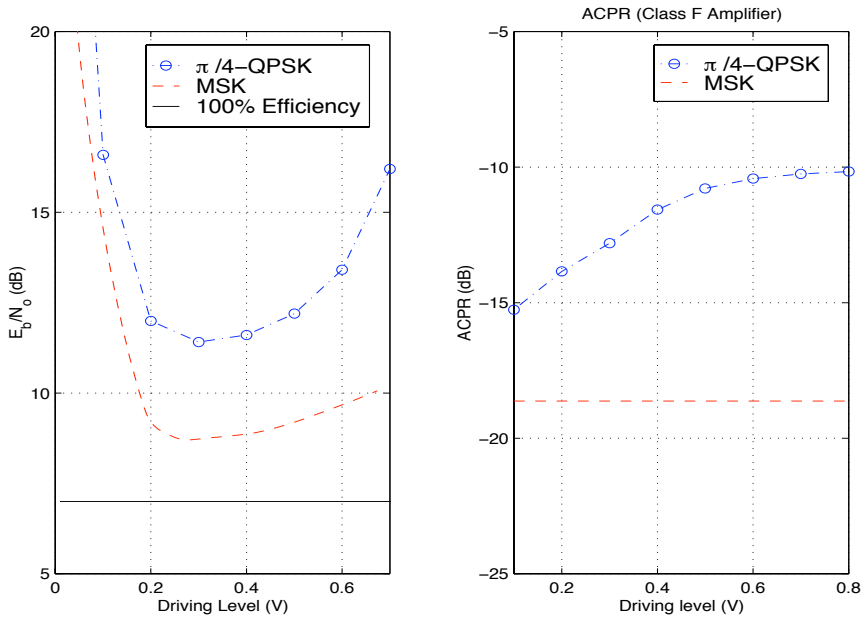

Figure 59: Class F amplifier with frequency spacing $1.08Hz$ (BER=10^{-3})

10 Multiphase Modulation Schemes

In a wireless data communications network, transmitting power is designed to be large enough to guarantee reliable communication between the transmitter and the least capable receiver (the worst link), which is either too far away from the transmitter or under severe shadowing. For a more capable user, the received signal power is usually more than enough to correctly decode the information. Unbalanced QPSK(UQPSK) (Fig.60(a)) can make more efficient use of energy by multicasting a secondary channel for the more capable users without significant degradation of the master link quality. As shown in Fig.61(a), the signal power of the secondary channel is usually a small fraction of the total power, and will be considered as a source of interference by less capable users. Given certain energy and application constraints, this modulation scheme enables the network to dynamically allocate GPS and voice signal power.

Error performance was analyzed for uncoded system with coherent and noncoherent unbalanced DQPSK demodulator over AWGN channel by Pursley *et. al.*[17]. Convolutionally coded system over AWGN channel was also studied under the assumption that the master and secondary channel have the same data rate[18]. In this report we evaluate the performance of convolutionally coded UQPSK with nonlinear amplifier over slow Rayleigh fading channel. More specifically, we are considering 160 kHz channel bandwidth, the basic data stream(GPS) of rate 10bps, and the secondary data stream(voice) of rate 10Kbps.

When pulse shaping filters are used, UQPSK signals no longer have constant envelope and will be severely distorted by nonlinearity when the envelope goes through the origin. We suggest a modified UQPSK modulator which rotates the constellation by $\pi/2$ every symbol period(Fig.60(b)). Since new constellation avoids the origin, as shown in Fig.61, signal is expected to be less distorted.

As shown in Fig.60, both voice and GPS channels are protected with forward error control(FEC) coding, which is a constraint length 5, rate 1/2 convolutional code. Independent random spreading sequences $a_1(t)$ and $a_2(t)$ have spreading factor 6 and 6000, respectively. Square root raised cosine filters of typical roll off factor of 0.35 are used to reduce the inter-channel-interference. The total processing gain W/R_b for GPS channel and voice channel are 42.1dB and 12.1dB, respectively. A solid state nonlinear amplifier model is considered with fifth-order AM-AM characteristic, as described in previous sections, and negligible AM-PM effect.

The effect of nonlinearity on uncoded multicast scheme with $\theta = 15^o$ over AWGN channel is shown in Fig.62. Driving level is defined as the average amplifier input envelope. Driving level 0.1 is in the linear amplification region for the power amplifier, and 0.3 is in the saturation region. It is indicated in Fig.62 that the GPS channel has 0.5dB degradation due to the nonlinearity distortion, while the voice channel, surprisingly, has 1dB improvement in terms of P/J. The justification of the "nonlinearity gain" is that the voice channel gets amplified more than the GPS channel does(about 1.9dB from actual measurement). Since the contribution of the voice signal component is only a small fraction, around 1/10, of the total input signal power at the input of the power amplifier, saturation, which implies low amplification gain, always happens when the GPS channel

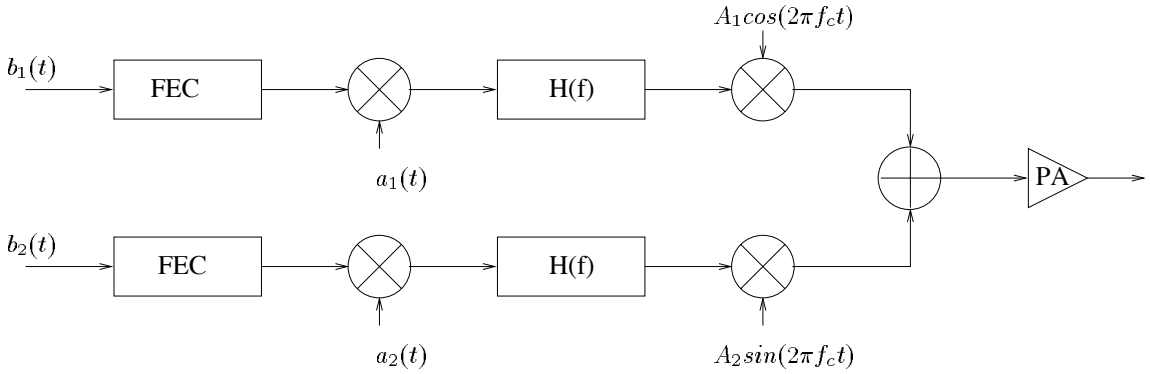

(a) UQPSK

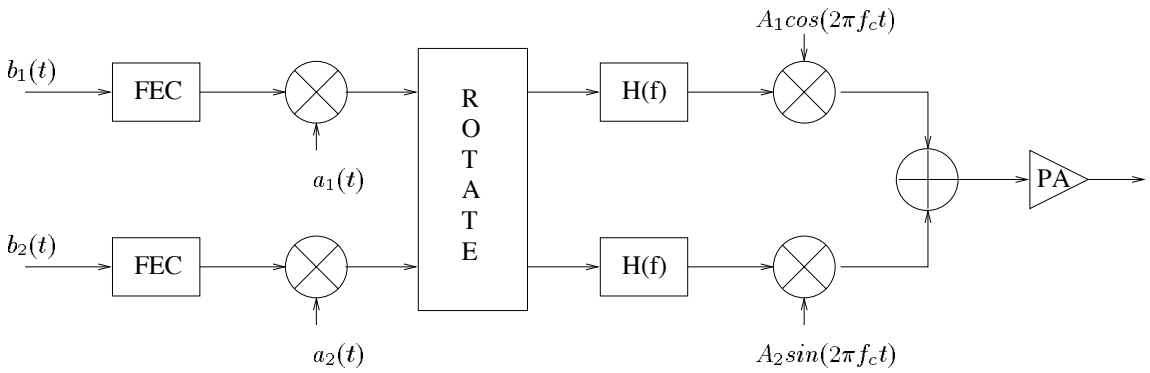

(b) MUQPSK

Figure 60: Multiphase modulation schemes, (a) Unbalanced QPSK(UQPSK) (b) Modified Unbalanced QPSK(MUQPSK)

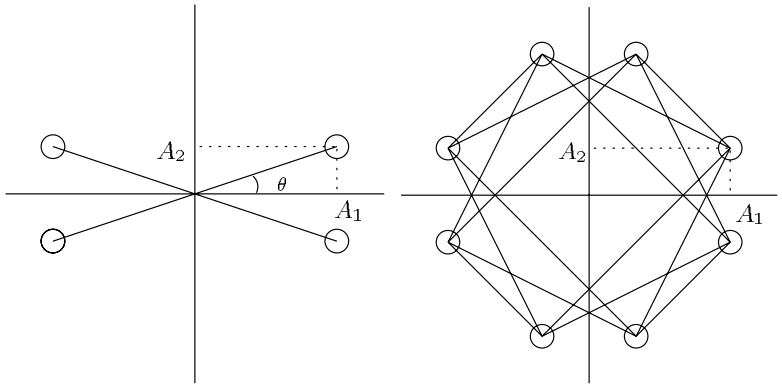

(a) UQPSK (b) MUQPSK

Figure 61: Signal constellations for multiphase modulation schemes, (a) Unbalanced QPSK(UQPSK) (b) Modified Unbalanced QPSK(MUQPSK)

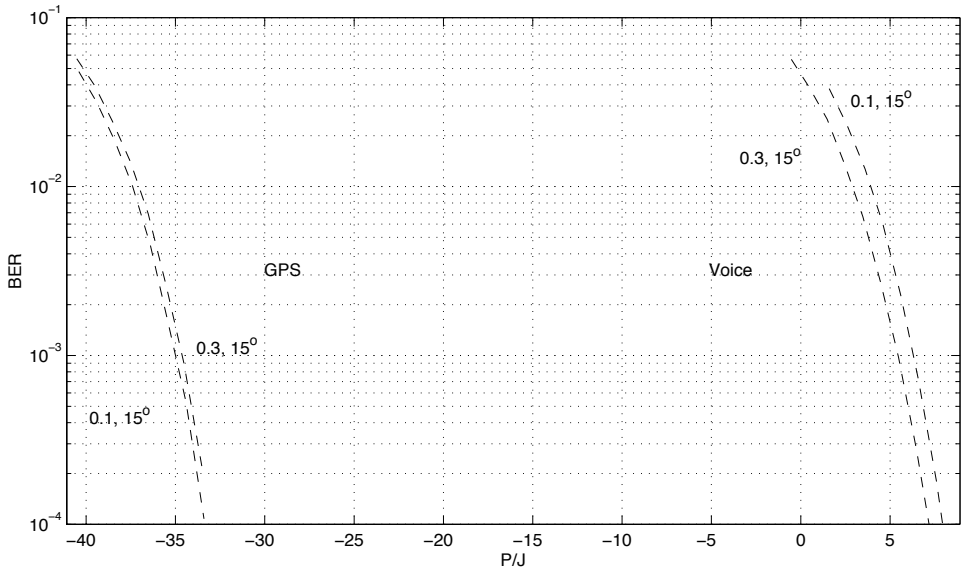

Figure 62: Effect of nonlinearity on BER performance of GPS channel and voice channel of unbalanced QPSK($\theta = 15^o$) over AWGN Channel: drive level 0.1 and 0.3

has large input. It follows that the voice channel gets more gain for large input power, therefore, has larger average amplification than the GPS channel does.

The performance degradation of uncoded GPS channel with UQPSK, which spends a small fraction of power on the additional voice channel, is compared with the BPSK system. Fig.63 shows the BER versus P/J performance curves for three different angles: $\theta = 0^o$(BPSK), $\theta = 15^o$, and $\theta = 45^o$. The analytical BER curve for BPSK over AWGN channel is also plotted for comparison. It is noticed that , when $\theta = 15^o$, there is a 0.3dB loss in signal to noise ratio compared with the $\theta = 0^o$ modulator in both amplifier linear and saturation region. When $\theta = 45^o$, the degradation in performance is 3dB.

Modified unbalance QPSK(MUQPSK) uses signal constellation(Fig.61(b)) that avoids the origin, where nonlinearity severely distorts the signal. Simulation comparison of the error performance of UQPSK and MUQPSK with $\theta = 15^o$ over Rayleigh fading channel is shown in Fig.64. We assume the fading is constant over a chip period and independent fading over each chip can be obtained with a interleaver of sufficiently large size. Analytical error upper bounds for convolutionally coded linear DS/CDMA system over independent Rayleigh fading with maximum ratio combining are plotted for comparison. It is observed that for UQPSK system, the BER curves stay close to the upper bounds for BER above 10^{-4}. It implies that for both GPS and voice channels the interference due to nonlinearity is effectively mitigated by coding and spreading. For the MUQPSK system, GPS channel gains an additional 0.3dB, while voice channel has 2.5dB loss. When the modulator switches the signals on in-phase and quadrature-phase channels for every symbol period, the voice signal, which lies in between two large GPS signals, suffers from the large interference from the adjacent GPS symbols, which results in the 2.5dB loss in error performance.

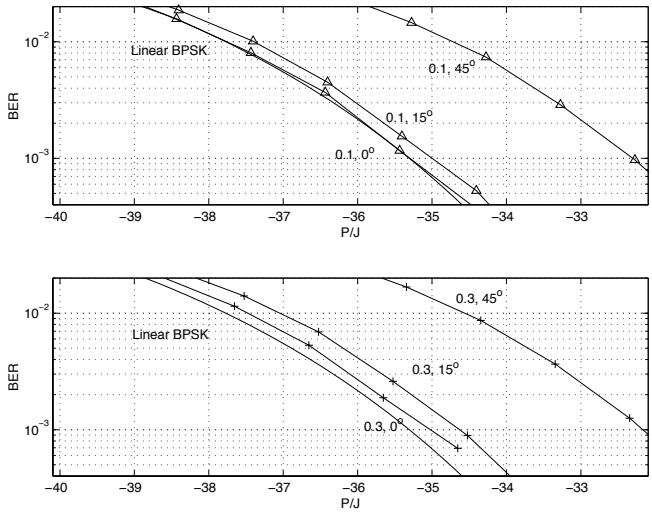

Figure 63: Error performance of uncoded UQPSK GPS branch over AWGN Channel. PA drive level 0.1 and 0.3, $\theta = 0^o$, 15^o, and 45^o

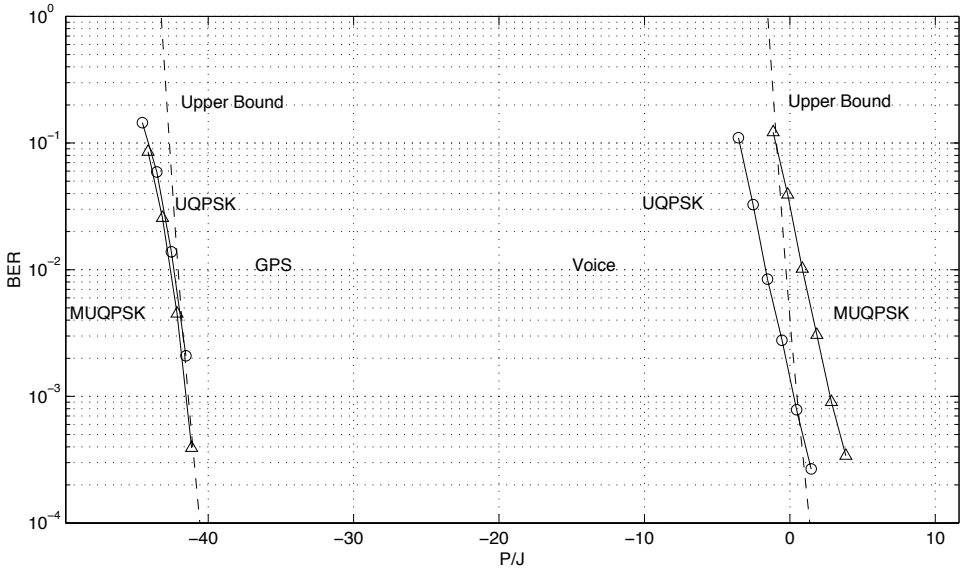

Figure 64: Error performance of convolutionally coded UQPSK and MUQPSK systems with $\theta = 15^o$ over Rayleigh fading Channel. PA drive level 0.3

11 Turbo Combining

Conventionally a data network with automatic repeat request(ARQ) protocol employs a fixed rate forward error correcting(FEC) code and discards erroneous packets if they contain uncorrectable errors. Modified FEC/ARQ schemes use rate adaptive coding techniques, which send incremental redundancy in each retransmission and combine all received packets to make a joint re-decoding[19, 20]. Recent advances in turbo coding techniques, originally proposed by Berrou *et. al.*[21] in 1993, enable us to achieve error performance approaching Shannon limit on AWGN channel. Application of punctured turbo codes for redundancy retransmission in ARQ system has been studied in[22, 23].

This section determines the overall network throughput of an ARQ technique based on turbo coding for direct sequence spread spectrum multiple access systems. Coherent BPSK modulation is assumed. Both AWGN and fully interleaved Rayleigh faded channels are considered. Concatenation of shortened error-correcting-only hard decision Reed-Solomon(RS) codes and punctured turbo codes is employed as the FEC code. We concentrate on the cases where the packet size for all transmissions is the same. Avoiding small redundancy packets reduce the number of retransmissions and, therefore, the overall delay.

One purpose of this paper is to find the optimal choice of RS codes to maximize the network throughput. For different RS code rates, we keep the number of information bits in a packet the same, and vary the codeword length. Two families of shortened RS codes with symbol size 6 and 8 bits are studied for sources with 204 bits(20 ms of 9.6kbps voice data plus 12 bits CRC) and 424 bits(standard ATM cell) information packets.

The inner turbo codes are from a family of rate compatible codes based on a rate 1/4 turbo codes with 4-states constituent code. The interleavers are designed following the S-interleaver construction introduced by Divsalar [24]. The ARQ procedures are as follows. The first transmission is coded with just a RS code. The systematic bits of the turbo code, i.e., the RS codeword, is spread with a random spreading sequence and sent over a BPSK modulated channel. If errors are detected after RS decoding, a negative ACK is sent to the transmitter. The transmitter then sends a parity packet by puncturing every other bit from the first and second constituent encoder parity bits, which together with the first transmission forms a rate 1/2 turbo code block. If the FEC code decoder still can not correct all the errors, the receiver will request the transmission of the bits punctured in second transmission. If the overall rate 1/3 code fails, the parity bits from a third constituent codes will be sent. If more failures occur, the transmitter will re-send the parity packets of constituent codes until a positive ACK is received.

Preliminary results are based on the assumption that the number of users in the network is constant and each user has duty factor 1. We assume that the systems employ average power control and the number of users $M$is large. We define the network load L as M/G, where G is the spreading gain. The overall normalized throughput η is defined as $\frac{M}{GT}\frac{K_{RS}}{N_{RS}} = \frac{L}{T}\frac{K_{RS}}{N_{RS}}$, where K_{RS} is the number of information symbols in a RS codeword, N_{RS} is the length of the codeword, and T is the average number of transmissions required to correctly decode an information packet.

Preliminary results of the proposed system performance over AWGN channel with

different rate of RS codes are shown in Fig.65. As indicated in Fig.65, for certain offered network loaded, optimal choice of RS code rate can be made to maximize the throughput. For example, when $L = 0.5$, the optimal code is RS(54,34) for voice frame and RS(83,53) for ATM cell, respectively; when $L = 3$, turbo coding without RS coding system is the best choice for both data sources. Comparison with average code combining(ACC)[19], which retransmits the same information copy then averages up all received copies, and standard ARQ, is also shown in Fig.66(a). It is observed that the proposed system quadruples the maximum throughput of a standard FEC/ARQ system. Considerable gain over average code combining is also obtained at the cost of more complexity. Average delays of different systems are also shown in Fig.66(b).

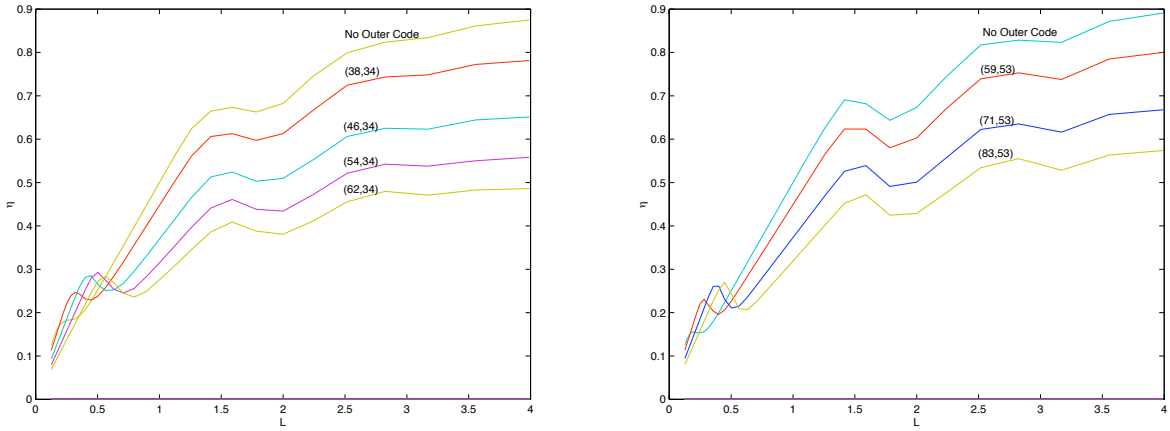

(a) Voice Frame

(b) ATM Cell

Figure 65: Total network throughput versus offered load of the ARQ technique with shortened Reed-Solomon outer codes and rate compatible turbo inner codes for DS/SSMA system over AWGN channel

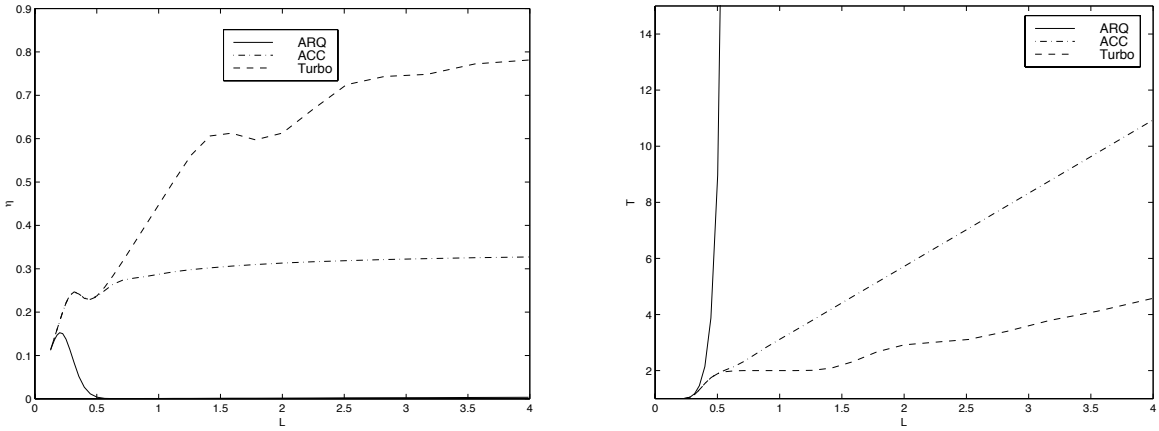

(a) Network Throughput

(b) Average Number of Transmissions

Figure 66: Comparison of conventional ARQ, average code combining, and turbo coded ARQ techniques with (38,34) shortened Reed-Solomon outer code for DS/SSMA system over AWGN channel: (a) Network throughput vs. offered load; (b) Average number of transmissions vs. offered load

12 Code Combining for FHMA/MFSK Packet Radio Networks

A packet radio network is a collection of terminals which can communicate with each other via radio links [25]. The goal in designing such a network is to maximize the throughput in the presence of multiple access interference(MAI). Many papers have treated the throughput of frequency-hopped multiple access networks with conventional hybrid automatic-repeat-request(ARQ) protocols [25, 26, 27, 28].

Traditional hybrid ARQ protocols employ forward-error-correcting and error-detecting coding to correct and detect errors in the received packets. When errors are detected in a packet after error-correction, the packet is discarded. this design strategy makes sense when the link quality is high and there are only few errors. When a terminal is under severe interference, however, repeated transmission of a packet does not combat the channel effectively. Modified ARQ systems[29, 30, 31, 32] have been studied to *combine* two or more copies of one information block to get better network throughput over noisy channels.

In this section, code combining for FHMA/MFSK system is studied for two different channel models; namely, nonfading multiple access interference (MAI) channels and slow Rayleigh fading MAI channels. The network model of the packet radio network studied in this report is detailed in [25]. For a network to be in the class we study in this project, it must be homogeneous in the sense that the probability distribution of the interference is the same at each receiver. A fully connected satellite multiple-access network is one example in this class.

Average code combining (ACC) was analyzed and shown to achieve throughput that is more than twice that of the conventional FHMA systems for the nonfading MAI channel by Bigloo *et al.*[33]. Optimal choice of codes that maximize system throughput is suggested from simulation results on nonfading and fading MAI channels. Since average code combining of L copies of the same packet is equivalent to a soft-decision repetition code with rate $1/L$, we propose an alternative adaptive code combining scheme, convolutional code combining(CCC), which gives better gain for certain network configurations and channel conditions. In subsection A, the performance of conventional ARQ system is analyzed for comparison purpose. The performance of ACC and CCC systems is then examined in details in subsection B and C.

12.1 Conventional ARQ systems

In the FHMA/MFSK system in our mind, each (63,k) Reed-Solomon symbol is modulated onto one 64FSK or two 8FSK signals, respectively. Each MFSK signal is transmitted on one hop. At the receiver, a square-law detector makes hard decision on which symbol is transmitted and then feeds demodulation output to an error-correcting Reed-Solomon decoder. If the received Reed-Solomon word is correct or is in the error-correcting capacity of the code, information bits will be decoded; otherwise, a retransmission request is sent to the transmitter. This procedure is repeated until the information packet is decoded correctly. Throughout this report, we assume that the demodulator output symbol

errors are independent and the probability of undetected error of Reed-Solomon code is negligible. A baseline system diagram is shown in Fig.67.

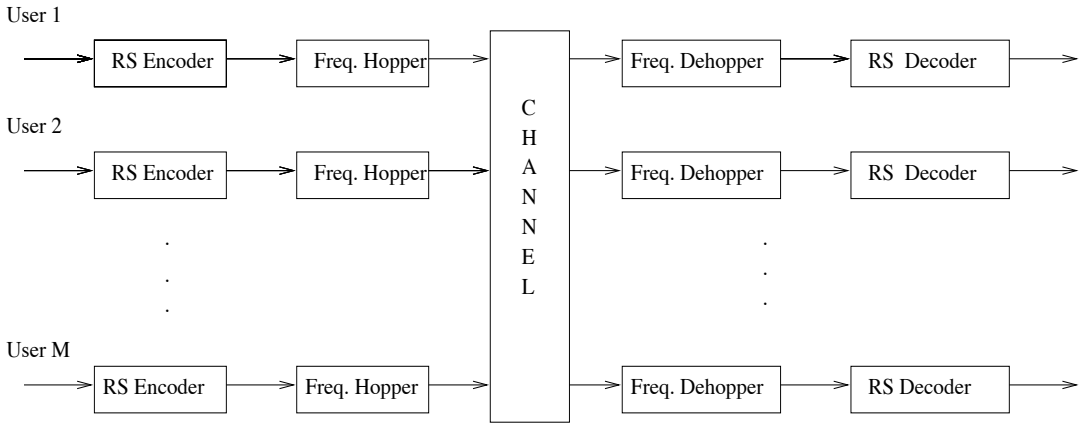

Figure 67: Block Diagram of a Frequency-Hopped Spread-Spectrum Multiple-Access System

The normalized throughput is defined as the average number of information symbols per channel use. Lower bounds of the throughput of a FHMA/8FSK(64FSK) system with 100 frequency slots is shown in Fig.68 as a function of total number of users over nonfading MAI channel. As expected, the throughput increases linearly with respect to the number of users when the MAI is small. However, when the number of user is large enough to cause too many errors for Reed-Solomon code to correct, system throughput starts to decrease drastically. Fig.68(a) shows that (63,43) code achieves maximum throughput of 0.095 when 20 users are in presence, (63,27) code achieves maximum throughput of 0.122 at 34 users, and (63,23) code performs best at 37 users with throughput 0.120. Notice that there is a tradeoff between the error correcting capacity and code rate. Optimal code, which achieves maximum throughput given certain number of users, has low rate when interference level is high and has high rate when interference level is low.

Fig.68(b) shows that for system with 64FSK modulation, (63,43) code achieves maximum throughput of 0.17 when there are 30 users, (63,27) code achieves maximum throughput of 0.22 at 60 users, and (63,23) code has a peak throughput at 0.21 for a total number of users of 65. The (63,27) code is the best in terms of maximum system throughput. The penalty for the system with 64FSK, which can support much more users than the system with 8FSK modulation, is a larger bandwidth expansion. For each Reed-Solomon code symbol, a system using 64FSK needs 64 tones while with 8FSK only 16 tones are needed.

Throughput performance with respect to the number of users in the presence of slow Rayleigh fading is presented in Fig.69 and 70. For the case where symbol energy to noise density ratio, γ_s, is 10 dB, the throughput of FHMA/8FSK systems have maximum value of 0.045, which is achieved for (63,23) code with 20 users; for 64FSK system, the throughput can reach at most 0.092 with (63,23) code at 40 users. This performance is not surprising since the high symbol error rate of FSK demodulator output causes too many Reed-Solomon code decoding failures. For the case of γ_s of 20 dB, since most errors are

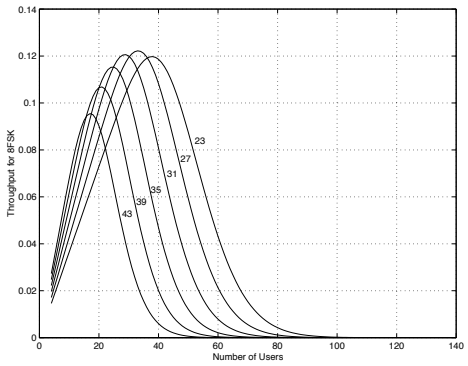

(a) 8FSK

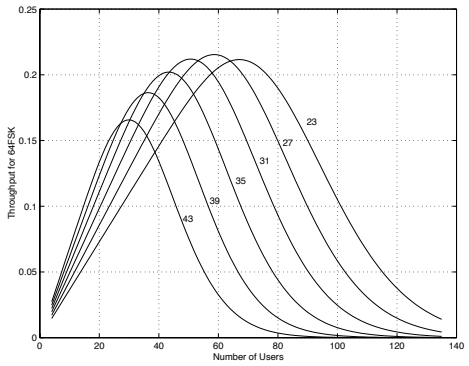

(b) 64FSK

Figure 68: Throughput for FHMA system with 100 subbands, noncoherent detection over nonfading MAI channel

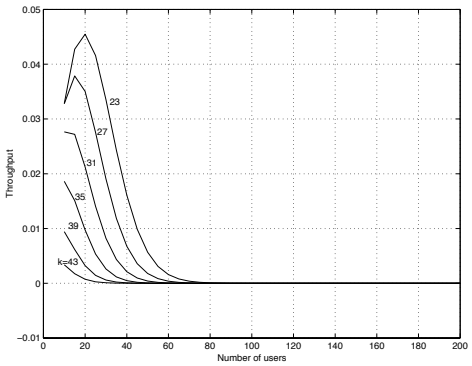

(a) 8FSK

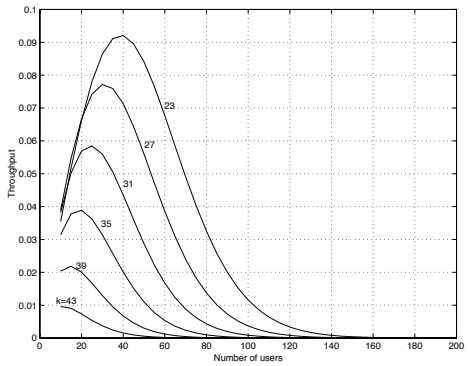

(b) 64FSK

Figure 69: Throughput for FHMA system with 100 subbands over Rayleigh fading MAI channel,γ_s=10dB

caused by multiple access interference other than background noise system throughput is only slightly worse than that of nonfading MAI channel without background noise. Maximum throughput for 8FSK is 0.11 and that for 64FSK is 0.2. For higher symbol energy noise density ratio, system performance is basically the same as the 20 dB case.

12.2 Average Code Combining

In this subsection, a hybrid ARQ scheme with average code combining is described[33]. When decoding failure occurs in Reed-Solomon decoder, a retransmission request is sent to the transmitter as in the conventional ARQ scheme. However, instead of discarding

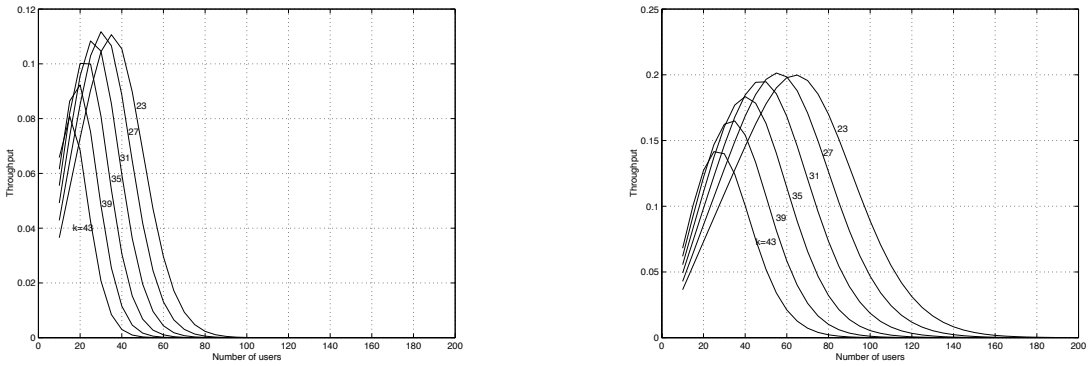

(a) 8FSK (b) 64FSK

Figure 70: Throughput for FHMA system with 100 subbands over Rayleigh fading MAI channel,γ_s=20dB

the erroneous packet, we keep the M outputs of the bank of square-law detectors. When l copies of the same packet are received, for each symbol, we average the outputs over l copies and obtain a new set of M squared-envelope decision variables. Then the decision logic choose jth symbol as output which corresponds to the square-law combiner that has the largest decision value. The effect of average code combining is the same as a FHMA system with diversity l, which is known to provide good antijamming capability.

The lower bound of throughput has been calculated based on simulations over nonfading MAI channels. Fig.71(a) shows the throughput for a system with 8FSK modulation. Compared with the conventional ARQ systems, the peak throughput increases from 0.12 to 0.23, which is achieved with (63,39) code at 85 users. For large number of users, e.g., more than 140, throughput of codes of high rate start to drop, while (63,23) codes still maintain a throughput of 0.15 for 200 users (twice the processing gain). Fig.71(b) shows that the throughput for a code combining system with 64FSK modulation increases linearly with the number of users for even more than 200 users. The highest throughput shown is around 0.7 compared with the maximum throughput of 0.22 for uncombined cases.

The lower bounds of throughput over fading MAI channels are obtained via the similar approach. Fig.72(a) shows that when γ_s is 5dB, the system maximum throughput is improved by 55% to 0.07 for 8FSK modulated system. Similarly for 64FSK the best throughput, 0.164(Fig.72(b)), has 78% improvement over uncombined system.

Fig.73(a) shows a maximum throughput of 0.11 at 30 users with (63,27) Reed-Solomon code for 8FSK and γ_s 20 dB. It is interesting to observe that the throughput doesn't change with the number of users and maintain a level of 0.07 in a large range of n for most of the codes. Fig.73(b) shows that the maximum throughput of the 64FSK systems is 0.2 at 50 users with (63,27) and (63,23) codes. All codes show a dependence of throughput after the peak around 50 users and keep a throughput of 9.14 around 100 users and throughput

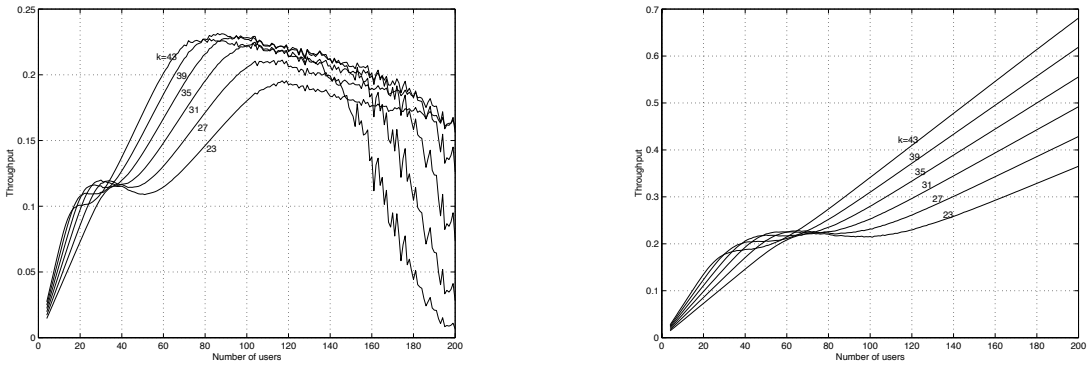

(a) 8FSK (b) 64FSK

Figure 71: Throughput for FHMA/MFSK systems with 100 subbands, noncoherent detection over nonfading MAI channel

0.14. The saddle-shaped curves decrease sharply after 150 users except for (63,27) and (63,23) codes which show a longer level period. Performance for γ_s of 40 dB cases are almost the same as 20 dB cases as shown in Fig.74.

Compare the performance of average code combining schemes with that of conventional retransmission schemes over fading channels, we found that the maximum throughput for high SNR cases does not have much improvement. The maximum number of users that system can tolerate, however, is increased significantly. For example, the throughput of a conventional system employing (63,39) code in 64FSK system decreases below 30% of peak value when there are 60 users in the network and γ_s is 20 dB. A similar system with average code combining can maintain throughput of 30% of the maximum value for up to 180 users. It means that when the networks are overloaded, the conventional systems break down quickly after a small threshold, while ACC system decrease the effective throughput per user gracefully for a relatively longer period.

12.3 Convolutional Code Combining

The use of feed-forward convolutional code with hard decision decoding in code combining has been studied on BSC and Gaussian channels[34, 30, 31, 29]. In this project, we are considering FHMA/MFSK system with RS-Convolutional concatenated coding structure under severe MAI interference, where the communication systems are overloaded. The convolutional code combining (CCC) system block diagram is shown in Fig.75.

Before describing the coding structure, we are going to describe a few considerations we had in the design process. First of all, we do not want to lower the transmission rate when there are moderate number of users, therefore we are only interested in systematic inner codes, which encode the Reed-Solomon codeword but leave it intact, i.e., available for uncoded transmission. As a well known fact, systematic feed-forward convolutional code is inferior to non-systematic ones in terms of minimum distance. However, Forney[35]

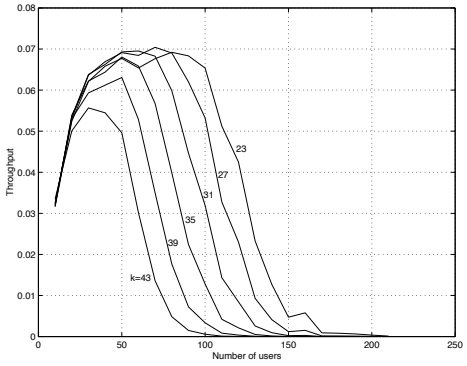

(a) 8FSK

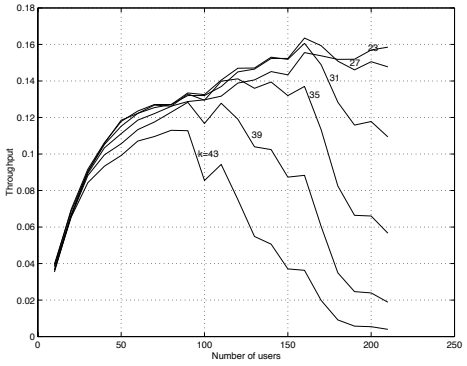

(b) 64FSK

Figure 72: Throughput for FHMA/MFSK systems with 100 subbands, noncoherent detection over slow Rayleigh fading MAI channel with $\gamma_s = 10$ dB

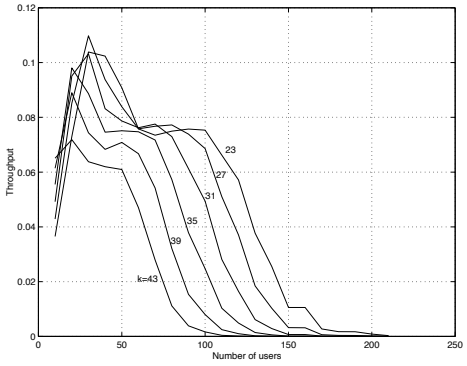

(a) 8FSK

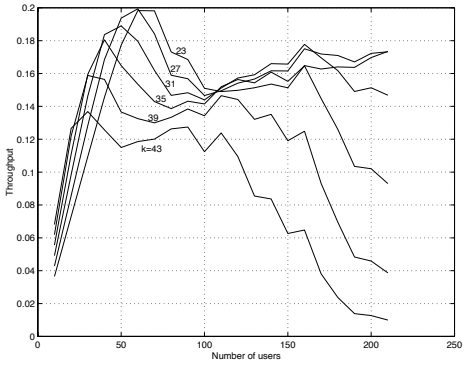

(b) 64FSK

Figure 73: Throughput for FHMA/MFSK systems with 100 subbands, noncoherent detection over slow Rayleigh fading MAI channel with $\gamma_s = 20$ dB

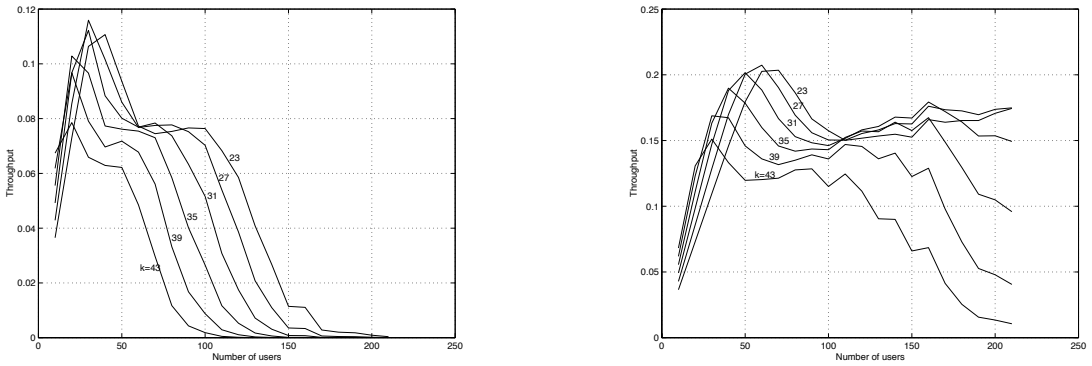

(a) 8FSK (b) 64FSK

Figure 74: Throughput for FHMA/MFSK systems with 100 subbands, noncoherent detection over slow Rayleigh fading MAI channel with $\gamma_s = 40$ dB

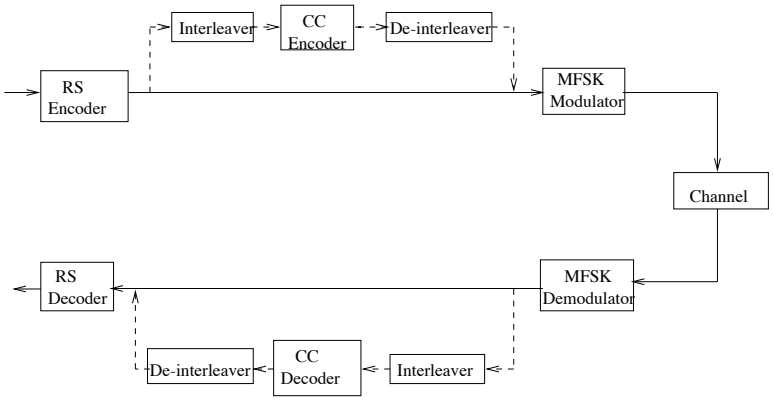

Figure 75: Convolutional code combining FHMA/MFSK system

showed that for any feed-forward code there always exist an *equivalent* systematic code with feedback that can be implemented with the same number of physical states. In this report, little effort has been made to find such equivalent codes, which is not hard for the rate $1/n$ codes considered here. Instead, we assume their existence and used the best feed-forward code to simulate the performance.

In the system we are going to describe, one Reed-Solomon codeword is modulated with MFSK and sent through the FHMA system with one MFSK signal per hop, the receiver attempts to decode the received word with hard-decision Reed-Solomon decoder. If decoding failure occurs, the square-law detector output envelopes are saved for next decoding attempt and ARQ is sent. When transmitter receives an ARQ, it encodes the information packet with a rate 1/2 systematic convolutional code and send the parity check copy through the channel. After receiving both information and parity check packets, a soft-decision Viterbi and error-correcting Reed-Solomon concatenated decoder is used to

correct errors. If there are still errors in the decoded block, both copies of the packets are saved for future decoding, and ARQ is sent to the transmitter. Then the transmitter sends the second parity check packet from a rate 1/3 convolutional code which contains the rate 1/2 code. The process keeps on going with decreasing code rate until a correct packet is decoded.

It should be noticed in Fig.75 that double interleaving is employed. Convolutional codes are very good at correcting random errors produced by a binary memoryless channel, but do not perform well in the presence of burst errors, which is the case of the system we are considering. To break burst errors produced by MFSK, interleaving is necessary between MFSK demodulator and Viterbi decoder. Since the first transmission is going to pass through the channel without any interleaving, a double interleaving structure is used for parity check packets.

To make use of soft decision Viterbi algorithm, we need to generate likelihood value for each individual bit. Bit-by-bit maximum *a posteriori*(MAP) soft-output algorithm[36] is used with noncoherent MFSK demodulator.

Throughput lower bounds are obtained using the symbol error probability by simulations. Throughput of CCC system over nonfading MAI channel is shown in 76. Fig.76(a) shows a peak throughput of 0.32 at 140 users with (63,43) RS code and four states soft-decision convolutional codes. It is observed that the throughput of all codes except for (63,23) codes are still increasing when the number of users in the system exceed 140. Due to the limited simulation time, we are unable to provide more data for the time being. Comparison with ACC systems for 8FSK indicates that the throughput of CCC system is always higher, especially in the cases where the number of users are larger than 100. Fig.76(b) shows that the 32 states convolutional codes have a minor throughput improvement over 4 states code. 64FSK systems are apparently inferior to the ACC systems.

Throughput of CCC systems for 20 dB and 40 dB are shown in Fig.77 and 78. Significant gain is again observed over ACC system for 8FSK systems for both 20 dB and 40 dB cases. More important, no cutoff point is noticed in CCC systems for at least 140 users. As shown in Fig.77(c) and 77(d), CCC system with 64FSK modulation works even worse than uncombined case for γ_s =20 dB. However, since no simulation has been conducted for rate lower than 1/5, i.e., lower bound could be loose, it would be more fair to draw conclusion after more data have been obtained. When γ_s =40dB, CCC with 64FSK works slightly better than ACC system in terms of cutoff number of users and maximum throughput. Notice that, in CCC system, maximum throughput is mostly achieved by high rate Reed-Solomon code, while low rate codes are usually better in ACC and uncombined case.

12.4 Summary of Code Combining Studies of FHMA/MFSK networks

In this report, the throughput of uncombined system and ACC system are shown for a variety of number of users, Reed-Solomon codes, and average symbol energy noise density ratio. Optimal choice of codes is suggested from simulation results. ACC is shown to be a robust method to combat high background noise level in fading channel.

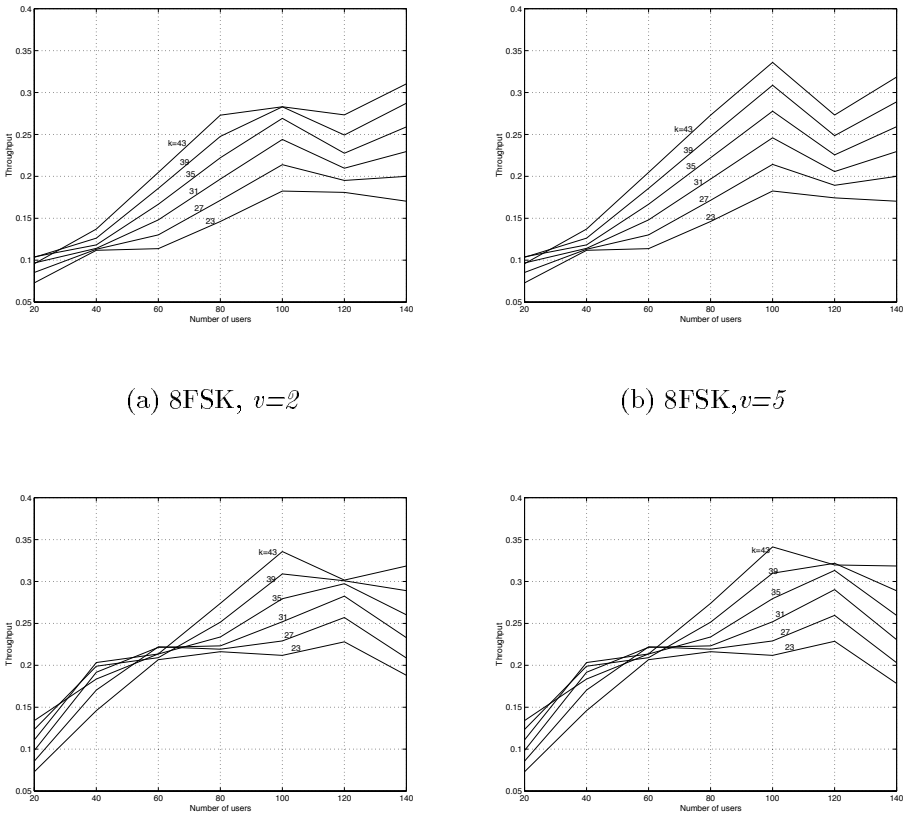

(a) 8FSK, v=2 (b) 8FSK,v=5

(c) 64FSK, v=2 (d) 64FSK,v=5

Figure 76: Throughput for FHMA/MFSK systems with 100 subbands, noncoherent detection over nonfading MAI channel, CCC

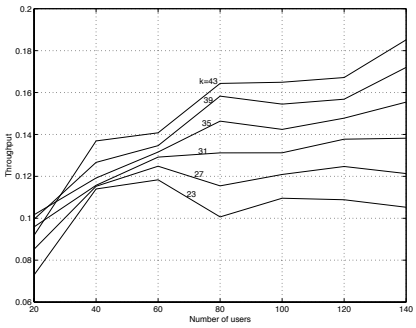

(a) 8FSK, *v=2*

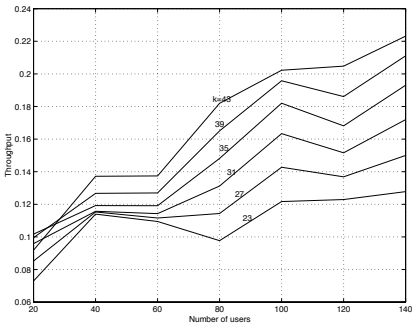

(b) 8FSK,*v=5*

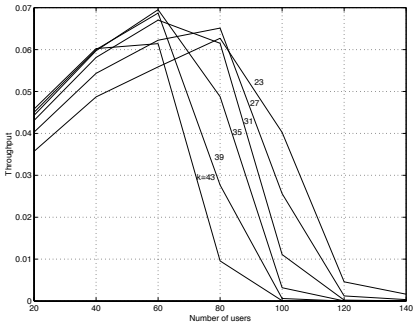

(c) 64FSK, *v=2*

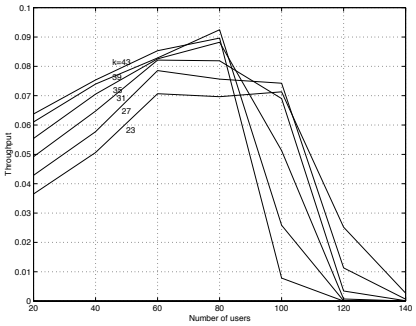

(d) 64FSK,*v=5*

Figure 77: Throughput for FHMA/MFSK systems with 100 subbands, noncoherent detection over slow Rayleigh fading MAI channel, $\gamma_s = 20$ dB CCC

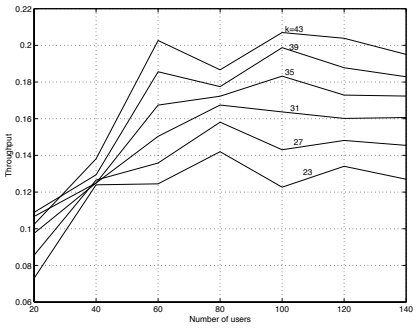

(a) 8FSK, *v=2*

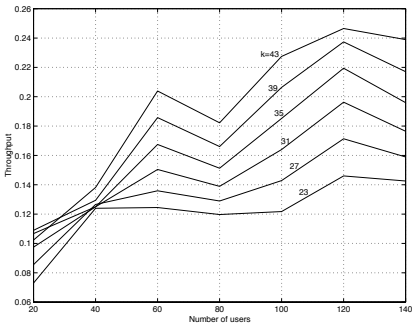

(b) 8FSK,*v=5*

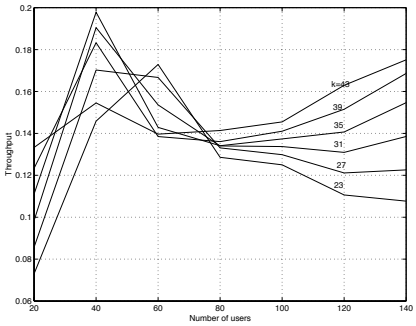

(c) 64FSK, *v=2*

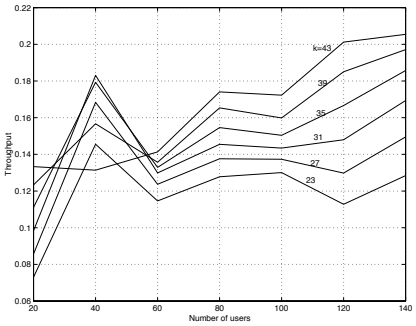

(d) 64FSK,*v=5*

Figure 78: Throughput for FHMA/MFSK systems with 100 subbands, noncoherent detection over slow Rayleigh fading MAI channel, $\gamma_s = 40$ dB CCC

A new code combining system utilizing rate 1/n systematic feed-back convolutional codes is proposed for the channels under consideration. Significant maximum throughput improvement is observed for systems with 8FSK modulation scheme with both channel models. In addition, the CCC system consistently maintains high throughput for less than 140 users (maximum number of users simulated), while the ACC system has very few codes that can maintain a relatively large throughput when the number of users is more than 100. The 64FSK systems which employ CCC, however, are generally inferior to those that employ ACC.

Since 8FSK system uses only a quarter of the bandwidth used by 64FSK system, this study indicates that CCC should be used in the situation that user suffers from fading and bandwidth is also of concern. Another interesting observation is that the set of Reed-Solomon codes that gives better performance in CCC system generally has larger rate than the optimal codes in ACC systems.

For future research, in the case where Reed-Solomon code is employed in packet radio networks, inner codes which perform well under severe interference are desired to construct more efficient code combining system. Since interleaving spreads bit errors randomly into Reed-Solomon code symbols, nonbinary inner codes which match Reed-Solomon symbol size, like Dual-K codes, are of great interests in the future. Simplification of the numerical evaluation of several key equations is desired to get more solid analysis and insight into the desired structure of the inner codes. Since we assumed the existence of systematic convolutional codes with feed-back that perform as well as the best feed-forward codes, it would be interesting to actually find these codes via conversion algorithm or code search.

13 Notes on Walsh Function Modulated Waveform

13.1 Introduction

Walsh functions are used as part of the signaling code set in IS95 code-division multiple-access (CDMA) cellular radio. Six bits of data are used to select one of sixty-four 64-bit Walsh-Hadamard functions. At the receiver the 64-bit symbols are converted back to 6 information bits. This procedure is equivalent to the use of a block error-correcting code superimposed on the basic modulation [37]. It appears to be useful in some applications to employ this scheme on 20 bits of data to select one of 2^{20}=10485761048576-bit Walsh-Hadamard functions to be transmitted. To do this, an efficient procedure must be found to generate the appropriate 2^{20}-bit Walsh-Hadamard pattern for any given 20-bit information pattern. Two hardware variations of a simple scheme are presented in this section. An inverse process must occur at the receiver; that is, given a 2^{20}-bit pattern, the receiver must determine the most likely 20-bit information string used to select that pattern. This task is facilitated through use of the fast Hadamard transform.

13.2 Digitally Modulated Pulse Waveforms

In this section, we show that when forming digitally modulated pulse waveforms, the resulting spectrum factors into the product of the discrete Fourier transform (DFT) of the digital modulation and the appropriate transform of the pulse waveform. This factorization allows the effects of the choice of digital modulation and the choice of pulse waveform to be addressed separately.

We first construct a waveform to be transmitted as a weighted sum of L shifts of a fixed pulse waveform $p(t)$ as

$$s(t) = \sum_{m=0}^{L-1} w(m)p(t - T_c).$$

It can be shown that for the continuous case where $p(t)$ is finite duration and possesses a Fourier transform, $P_F(f)$, the Fourier transform of $s(t)$ is

$$S_F(f) = W_F(f)P_F(f)$$

where

$$W_F(f) = \sum_{m=0}^{L-1} w(m)e^{-j2\pi fT_c}.$$

For the continuous case where $p(t)$ is periodic with period $T_p = LT_c$ and possesses a Fourier series representation $P_{FS}(k)$, the Fourier series representation of $s(t)$ is

$$S_{FS}(k) = LW(k)P_{FS}(k)$$

where

$$W(k) = \frac{1}{L}\sum_{m=0}^{L-1} w(m)e^{-j2\pi km/L}.$$

Finally, for the sampled case where the sample rate is an integer multiple, R, of the chip rate the discrete Fourier transform $S_D(k)$ of $s(t)$ can be written as

$$S_D(k) = LW(k)P_D(k)$$

where

$$W(k) = \frac{1}{L}\sum_{m=0}^{L-1} w(m)e^{-j2\pi km/L}.$$

For the sampled case the $p(t)$ waveform need not be periodic.

If $p(t)$ is not periodic, then a time interval T_P is chosen to include a region of time where $p(t)$ has negligible energy and is of sufficiently long duration to avoid time overlap (depending on the operations to be performed) caused by periodicity forced by use of the DFT.

In all cases the spectrum of the constructed waveform factors into the product of what is essentially the discrete Fourier transform of the weight values and the Fourier transform of the chip waveform. This factoring provides advantages in both signal design and signal processing because the selection of the weighting values and the selection of the pulse waveform can be considered independently.

13.3 Walsh Functions

(Much of the material in this section is based on [38].) Walsh divided the unit interval into $N = 2^n$ equal intervals and showed how to define a complete orthonormal set of two valued (± 1) functions having zero crossings only at the points of division. These (Walsh) functions are analogs to the sine and cosine functions used in a Fourier series. The values of the Walsh functions on the sub-intervals can be written as vectors of ± 1 values, or in binary form where $+1$ maps to 0 and 1 maps to 1. Note that multiplication using ± 1 on the integers is isomorphic with binary addition modulo-2; that is, arithmetic in the Galois field GF(2) containing only the elements 0 and 1. In the example matrices given below the sign is a shorthand notation for a 1 value.

13.3.1 Sequency Ordered Walsh Functions

Walsh ordered his functions in terms of the number of zero crossings per interval. Harmuth [39] defines the term sequency to be one-half the number of sign changes per interval. The sequency, s_i, of the i-th Walsh function is

$$s_i = \begin{cases} 0 & i = 0, \\ i/2 & i \ even, \\ (i+1)/2 & i \ odd. \end{cases}$$

The Walsh functions as originally ordered are denoted $\mathrm{wal}_w(i,t)$. The digital representation is written as $\mathrm{wal}_w(i)$. The sequency ordered digital Walsh function values for

$N = 8$ are

$$\begin{bmatrix} \text{wal}_w(0) \\ \text{wal}_w(1) \\ \text{wal}_w(2) \\ \text{wal}_w(3) \\ \text{wal}_w(4) \\ \text{wal}_w(5) \\ \text{wal}_w(6) \\ \text{wal}_w(7) \end{bmatrix} = \begin{bmatrix} 1 & 1 & 1 & 1 & 1 & 1 & 1 & 1 \\ 1 & 1 & 1 & 1 & - & - & - & - \\ 1 & 1 & - & - & - & - & 1 & 1 \\ 1 & 1 & - & - & 1 & 1 & - & - \\ 1 & - & - & 1 & 1 & - & - & 1 \\ 1 & - & - & 1 & - & 1 & 1 & - \\ 1 & - & 1 & - & - & 1 & - & 1 \\ 1 & - & 1 & - & 1 & - & 1 & - \end{bmatrix}$$

13.3.2 Dyadic ordered Walsh Functions

Paley [40] ordered the Walsh functions in dyadic space. The Walsh functions, when ordered in the Paley manner are denoted $\text{wal}_p(i)$. The Paley ordered Walsh functions for $N = 8$ are

$$\begin{bmatrix} \text{wal}_p(0) \\ \text{wal}_p(1) \\ \text{wal}_p(2) \\ \text{wal}_p(3) \\ \text{wal}_p(4) \\ \text{wal}_p(5) \\ \text{wal}_p(6) \\ \text{wal}_p(7) \end{bmatrix} = \begin{bmatrix} 1 & 1 & 1 & 1 & 1 & 1 & 1 & 1 \\ 1 & 1 & 1 & 1 & - & - & - & - \\ 1 & 1 & - & - & 1 & 1 & - & - \\ 1 & 1 & - & - & - & - & 1 & 1 \\ 1 & - & 1 & - & 1 & - & 1 & - \\ 1 & - & 1 & - & - & 1 & - & 1 \\ 1 & - & - & 1 & 1 & - & - & 1 \\ 1 & - & - & 1 & - & 1 & 1 & - \end{bmatrix}$$

13.4 Hadamard Ordered Walsh Functions

The set of digital Walsh function vectors for a given value of N is identical to the set of vectors composing the N-th order Sylvester-Hadamard matrix. The digital Walsh functions when ordered as the rows of a Sylvester-Hadamard matrix (also referred to as a Walsh-Hadamard matrix) are sometimes said to be in *natural* order and are denoted at $\text{wal}_h(i)$. The natural ordered digital Walsh functions for $N = 8$ are

$$\begin{bmatrix} \text{wal}_h(0) \\ \text{wal}_h(1) \\ \text{wal}_h(2) \\ \text{wal}_h(3) \\ \text{wal}_h(4) \\ \text{wal}_h(5) \\ \text{wal}_h(6) \\ \text{wal}_h(7) \end{bmatrix} = \begin{bmatrix} 1 & 1 & 1 & 1 & 1 & 1 & 1 & 1 \\ 1 & - & 1 & - & 1 & - & 1 & - \\ 1 & 1 & - & - & 1 & 1 & - & - \\ 1 & - & - & 1 & 1 & - & - & 1 \\ 1 & 1 & 1 & 1 & - & - & - & - \\ 1 & - & 1 & - & - & 1 & - & 1 \\ 1 & 1 & - & - & - & - & 1 & 1 \\ 1 & - & - & 1 & - & 1 & 1 & - \end{bmatrix}$$

13.5 Properties of the Hadamard Matrix

A Hadamard matrix $\mathbf{H}$ of order N is an $N \times N$ matrix of $+1$ and 1 elements such that $\mathbf{H}\mathbf{H}^T = N\mathbf{I}$ where ^{T} denotes matrix transpose and $\mathbf{I}$ is the $N \times N$ identity matrix. If $\mathbf{H}_N$

is a Hadamard matrix of order N then

$$\mathbf{H}_N = \begin{bmatrix} \mathbf{H}_{N/2} & \mathbf{H}_{N/2} \\ \mathbf{H}_{N/2} & -\mathbf{H}_{N/2} \end{bmatrix}$$

The matrices formed this way starting with $\mathbf{H}_1 = [1]$ have orders that are integer powers of two and are called Sylvester-Hadamard matrices. The first four Sylvester-Hadamard matrices are:

$$N = 1: \quad \mathbf{H}_1 = \begin{bmatrix} 1 \end{bmatrix} \qquad N = 2: \quad \mathbf{H}_2 = \begin{bmatrix} 1 & 1 \\ 1 & - \end{bmatrix}$$

$$N = 4: \quad \mathbf{H}_4 = \begin{bmatrix} 1 & 1 & 1 & 1 \\ 1 & - & 1 & - \\ 1 & 1 & - & - \\ 1 & - & - & 1 \end{bmatrix} \qquad N = 8: \quad \mathbf{H}_8 = \begin{bmatrix} 1 & 1 & 1 & 1 & 1 & 1 & 1 & 1 \\ 1 & - & 1 & - & 1 & - & 1 & - \\ 1 & 1 & - & - & 1 & 1 & - & - \\ 1 & - & - & 1 & 1 & - & - & 1 \\ 1 & 1 & 1 & 1 & - & - & - & - \\ 1 & - & 1 & - & - & 1 & - & 1 \\ 1 & 1 & - & - & - & - & 1 & 1 \\ 1 & - & - & 1 & - & 1 & 1 & - \end{bmatrix}$$

The Sylvester-Hadamard matrix plays a major role in the generation and use of Walsh functions, the Reed-Muller error correcting code, and binary linear maximal sequences. As previously noted, the binary equivalent of a Hadamard matrix can be obtained by replacing the +1 values with 0 and the 1 values with 1. Henderson [41] showed that the binary Hadamard matrix can be written as the product of two simpler matrices using modulo-2 arithmetic.

Let n be an integer. Construct a $2^n \times n$ matrix $\mathbf{B}_{2^n}$ by setting its rows equal to the binary bits representing the integers from 0 through $2^n - 1$. The binary Hadamard matrix of order $N = 2^n$ is then formed as the product

$$\mathbf{H}_N = \mathbf{B}_N \mathbf{B}_N^T$$

To illustrate, the binary version of $\mathbf{H}_8$ is formed as

$$\begin{bmatrix} 0 & 0 & 0 & 0 & 0 & 0 & 0 & 0 \\ 0 & 1 & 0 & 1 & 0 & 1 & 0 & 1 \\ 0 & 0 & 1 & 1 & 0 & 0 & 1 & 1 \\ 0 & 1 & 1 & 0 & 0 & 1 & 1 & 0 \\ 0 & 0 & 0 & 0 & 1 & 1 & 1 & 1 \\ 0 & 1 & 0 & 1 & 1 & 0 & 1 & 0 \\ 0 & 0 & 1 & 1 & 1 & 1 & 0 & 0 \\ 0 & 1 & 1 & 0 & 1 & 0 & 0 & 1 \end{bmatrix} = \begin{bmatrix} 0 & 0 & 0 \\ 0 & 0 & 1 \\ 0 & 1 & 0 \\ 0 & 1 & 1 \\ 1 & 0 & 0 \\ 1 & 0 & 1 \\ 1 & 1 & 0 \\ 1 & 1 & 1 \end{bmatrix} \begin{bmatrix} 0 & 0 & 0 & 0 & 1 & 1 & 1 & 1 \\ 0 & 0 & 1 & 1 & 0 & 0 & 1 & 1 \\ 0 & 1 & 0 & 1 & 0 & 1 & 0 & 1 \end{bmatrix}$$

13.6 Generating Walsh-Hadamard Code Words

Several methods can be used to generate the Walsh functions. For small values of N (e.g., $N = 8$) table lookup is perhaps the simplest. For larger values of N (e.g., $N = 2^{20}$) an algorithm is the more efficient method to generate the desired bits.

A particularly simple hardware implementation is obtained by adapting Henderson's factoring method. The rows of $\mathbf{B}_N$ determine the rows of $\mathbf{H}_N$ while the columns of $\mathbf{B}_N^T$ determine the columns of $\mathbf{H}_N$. The i-th row of $\mathbf{H}_N$ is generated by taking the binary representation of i and forming the modulo-2 dot product of that value with the contents of a binary counter incrementing from 0 through $2^n - 1$ as the process progresses. The counter values determine the bit position. A circuit for performing this task is shown in Figure 79. The operation denoted as exclusive-or (modulo-2 addition) is also referred to as generating parity (an even number of 1 bits yields a zero while an odd number of 1 bits yields a one). An input of n data bits outputs 2^n code word bits.

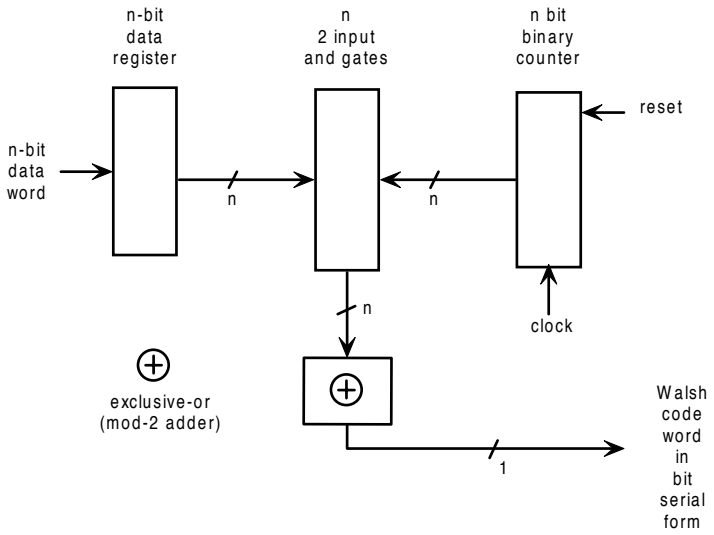

Figure 79: Hadamard matrix row generator, one bit at a time.

A simple modification of this circuit to allow generating the i-th row of $\mathbf{H}_N$ 2^m bits at a time is shown in Figure 80. This circuit uses the basic logic of Figure 79 for the most significant $n - m$ data bits and also for the 2^m hard-wired values of the lower m bits (0 through $2^m - 1$). The $n - m$ bit result is exclusive-or'd with the individual value results to form the desired m bits. The connection from the $n - m$-bit exclusive-or to the individual exclusive-or devices on the lower right is "flow-through". Every time the counter is incremented, an additional 2^m bits in the Walsh-Hadamard code word are produced. In many applications it should be feasible to replace much of the m-bit logic with table lookup hardware, or as a minimum much of the gate level logic for the 2^m fixed values can be combined.

13.7 The Fast Hadamard Transform

The Hadamard matrix possesses the same basic iterative structure that allows fast discrete Fourier transform (DFT) algorithms to be written. Many, if not all, integer powers of two DFT algorithms can be converted into fast Hadamard transforms by setting the twiddle

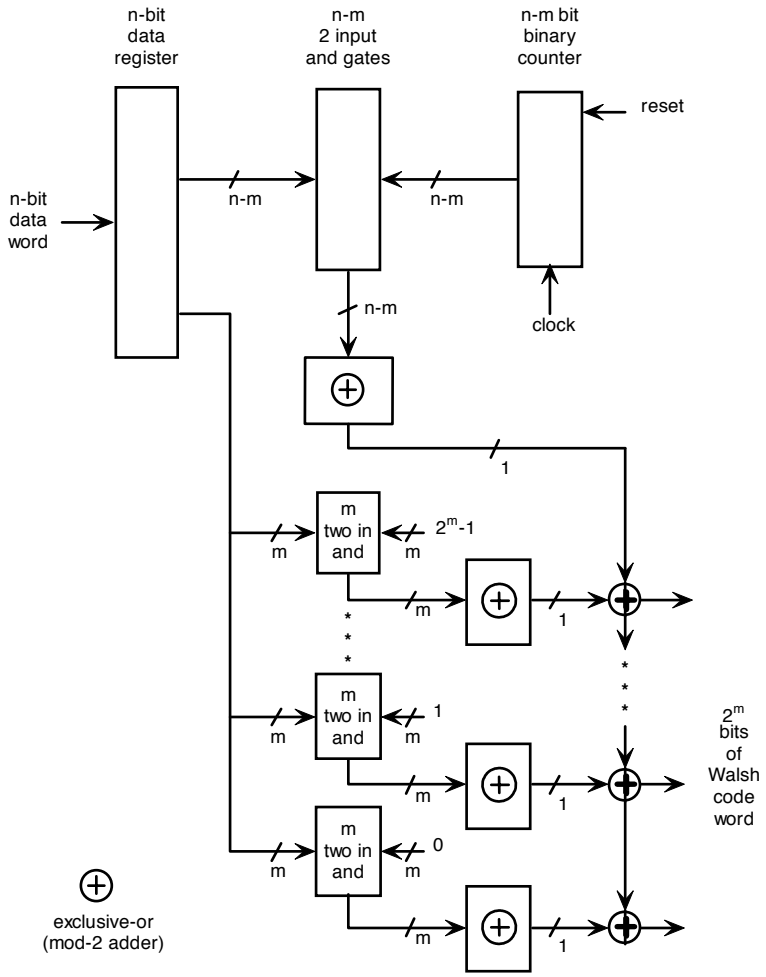

Figure 80: Hadamard matrix row generator, 2^m bits at a time.

factor values equal to one [42]. Because all multiplications are by ± 1, the required hardware/software is very simple in comparison to that required for the DFT. Sorrenson and Burris write in [42] "Since there are no twiddle factors, the complexity of the Hadamard transform, unlike that of the FFT, cannot be improved by using higher radix or split-radix algorithms." It is not clear what Sorenson and Burris meant by complexity. While the computational efficiency of the FHT cannot be improved upon in terms of the number of add/subtract operations, there is the chance for a performance increase by using a higher radix algorithm depending on the hardware involved.

For example, the Motorola 68020 has a number of registers that can act as accumulators, and since instruction fetch is pipelined, memory fetch/stores can be overlapped with register operations. Consider taking the FHT of 2^{20} values. An in-place radix-2 algorithm has 20 layers and moves 2^{20} values to and from memory at each layer. Because of the pipeline nature of the 68020, the required adds/subtracts take no additional processor time. A radix-4 algorithm has only 10 layers. As before, the arithmetic can be performed in conjunction with memory accesses. The net result is that on this computer a radix-4 algorithm can be written that will execute in half the time required by a radix-2 algorithm.

Figure 81 shows the signal flow graph for a decimation in time FHT for $N = 8$. This diagram was adapted from the decimation in time DFT signal flow graph shown in Figure 8-8 of [42]. The dashed lines represent paths where values are multiplied by 1. The algebraic values associated with the nodes at each stage are listed in Table 15. The table entry positions physically match the node locations in the signal flow graph. Examining the ± 1 weight values assigned to the components of the final values it is seen that the values are in the normal Hadamard order. No additional rearrangement is necessary. The transform is in-place.

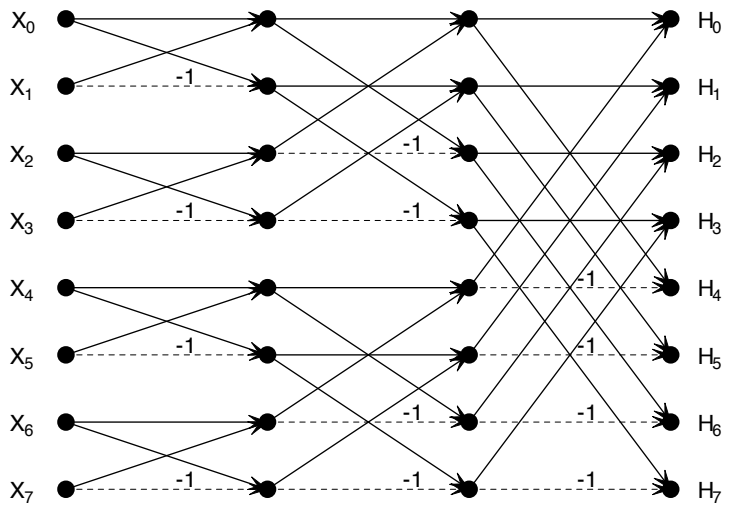

Figure 81: Decimation in time fast Hadamard transform signal flow diagram.

As the computation proceeds from left to right, the calculated values have the potential to increase in magnitude by a factor of 2 at each layer. Because the data of interest may

Table 15: Values at the nodes of the N=8 FHT.

X0	X0+X1	X0+X1+X2+X3	X0+X1+X2+X3+X4+X5+X6+X7
X1	X0-X1	X0-X1+X2-X3	X0-X1+X2-X3+X4-X5+X6-X7
X2	X2+X3	X0+X1-X2-X3	X0+X1-X2-X3+X4+X5-X6-X7
X3	X2-X3	X0-X1-X2+X3	X0-X1-X2+X3+X4-X5-X6+X7
X4	X4+X5	X4+X5+X6+X7	X0+X1+X2+X3-X4-X5-X6-X7
X5	X4-X5	X4-X5+X6-X7	X0-X1+X2-X3-X4+X5-X6+X7
X6	X6+X7	X4+X5-X6-X7	X0+X1-X2-X3-X4-X5+X6+X7
X7	X6-X7	X4-X5-X6+X7	X0-X1-X2+X3-X4+X5+X6-X7

be buried in the noise and may be less than a quanta in magnitude, each level should not simply be scaled by two. Doing so may result in a zero output. One possible scaling procedure is to scale by 2 every second layer. That way the noise variance stays constant (assuming i.i.d. noise) and the signal portion grows more slowly. In any case the number of bits that has to be retained grows as the signal flows from input to output.

13.8 Deciding Which Hadamard Row Was Received

In this example, bit synchronization between a transmitter and receiver is assumed. The maximum likelihood decoder is a replica cross-correlator. The matching of the basic digit shape and of the modulating sequence can be treated separately. This section only considers the gain from matching to the digital Hadamard code.

The following discussion assumes that Walsh functions in the Hadamard ordering are used to transmit twenty data bits per code symbol. The code symbols each contain 2^{20} bits. The reception is shifted to baseband and digitized. Samples are generated for both the in-phase (I) and quadrature (Q) channels. The Hadamard transform of the I and Q components is formed and the magnitude of each component calculated. The component with the largest magnitude is determined and its index is taken as the 20 data bits that were transmitted.

Using a radix-4 Hadamard transform, there are 10 processing layers. Each layer requires 2^{20} memory read and write operations. Suppose that the word size is sufficient so that overflow is not a concern (8-bit samples would require a minimum of 28 bits at the output if no scaling were done). Furthermore, assume a processor architecture that allows the I and Q components to be processed in parallel. The total number of data moves is $2^{20} \times 2 \times 10$ which is approximately 21×10^6. If 60 ns cycle time memory is used, then the amount of time required for data movement is approximately 1.26 seconds. The bit rate is then $10/1.26 = 15.9$ bits per second. Use of a radix-16 algorithm (assuming memory accesses completely overlap calculation times) would increase speed by a factor of 4.

Suppose that the bit SNR at the A/D converter is S dB. The SNR of the processed waveform that is used to determine the 20 data bits is $S + 60$ dB, a very large SNR gain. Of course, this accounts only for the improvement from the use of the Hadamard code.

13.9 A Program to Generate the Walsh Hadamard Matrix

Below is a small program that generates the N-th order Walsh-Hadamard matrix using the same process as was used in the circuit design contained in Figure 80. Following the listing is a sample output for $N = 32$.

```
/*   File name: hadcalc.c
 *
 *   Quick demonstration program to generate the Sylvester form of the
 *   Hadamard matrix of size 2^n by 2^n.  This is also called the
 *   Walsh-Hadamard matrix.
 *
 *   The procedure uses two counters.  The outer counter contains the
 *   index of the row currently being constructed.  The inner counter
 *   contains the index of the column currently being constructed.  The
 *   current element is determined by bitwise anding the contents of the
 *   two counters and determining the parity of the result.  If the number
 *   of ones in the and is even the bit is a zero.  If the number of ones
 *   in the and is odd the bit is a one.
 *
 *   Values are generated a row at at time.
 *
 *   Using a value of n=6 generates the IS95 64-ary orthogonal symbol set.
 *
 *   21May98 .. initial version .. Kurt Metzger
 */

#include <stdio.h> #include <stdlib.h>

void main() {
   unsigned n, outer_counter, inner_counter, and, bit, N;

   printf("enter n (log2 of the number of values per row): ");
   scanf("%d", &n);
   if (n == 0) {
      printf("n must be > 0\n");
      exit (1);
   }
   if (n > 32) {
      printf("n must be less than 33\n");
      exit (1);
   }
   N=1;
   while(n--) N <<= 1;
   printf("Hadamard matrix with %d elements per row\n", N);
   for (outer_counter = 0; outer_counter < N; outer_counter++) {
      printf("%04d  ", outer_counter);
      for (inner_counter = 0; inner_counter < N; inner_counter++) {
         and = inner_counter & outer_counter;  /* and the two counters */
         bit = 0;
         while (and != 0) {             /* count the number of 1's */
            bit += (and & 1);
            and >>= 1;
         }
         printf("%01d", bit & 1);       /* print bit */
      }
      printf("\n");
   }
}
```

Hadamard matrix with 32 elements per row

```
0000   00000000000000000000000000000000
0001   01010101010101010101010101010101
0002   00110011001100110011001100110011
0003   01100110011001100110011001100110
0004   00001111000011110000111100001111
0005   01011010010110100101101001011010
0006   00111100001111000011110000111100
0007   01101001011010010110100101101001
0008   00000000111111110000000011111111
0009   01010101101010100101010110101010
0010   00110011110011000011001111001100
0011   01100110100110010110011010011001
0012   00001111111110000000011111110000
0013   01011010101001010101101010100101
0014   00111100110000110011110011000011
0015   01101001100101100110100110010110
0016   00000000000000001111111111111111
0017   01010101010101011010101010101010
0018   00110011001100111100110011001100
0019   01100110011001101001100110011001
0020   00001111000011111111000011110000
0021   01011010010110101010010110100101
0022   00111100001111001100001111000011
0023   01101001011010011001011010010110
0024   00000000111111111111111100000000
0025   01010101101010101010101001010101
0026   00110011110011001100110000110011
0027   01100110100110011001100101100110
0028   00001111111100001111000000001111
0029   01011010101001011010010101011010
0030   00111100110000111100001100111100
0031   01101001100101101001011001101001
```

References

[1] P. Bello, "Characterization of randomly time-variant linear channels," *IEEE Transactions on Communications*, vol. CS-11, pp. 360–393, December 1963.

[2] A. G. Longley and P. L. Rice, *Prediction of tropospheric transmission loss over irregular terrain, a computer method*, ESSA Technical Report ERL 79-ITS 67, U.S. Department of Commerce, Boulder, CO, July 1968.

[3] M. N. Lustgarten and J. A. Madison, "An empirical propagation model(EPM-73)," *IEEE Transactions on Electromagnetic Compatibility*, vol. EMC-19, no. 3, , August 1977.

[4] A. P. B. P. L. McQuate, J. M. Harman, *Tabulations of propagation data over irregular terrain in the 230-9200 MHz frequency range, Part I: Gunbarrel Hill receiver site*, ESSA Technical Report ERL 65-ITS 58, U.S. Department of Commerce, Boulder, CO, December 1968.

[5] M. E. Johnson, M. Miles, P. McQuate, and A. Barsis, *Tabulation of VHF propagation data obtained over irregular terrain at 20, 50, and 100 MHz, Part III: Ohio data*, ESSA Technical Report IER 38-ITSA-38-3, U.S. Department of Commerce, Boulder, CO, December 1967.

[6] A. G. Longley and R. K. Reasoner, *Comparison of propagation measurements with predicted values in the 20 to 10,000 MHz Range*, ESSA Technical Report ERL 148-ITS 97, Department of Commerce, Boulder, CO, January 1970.

[7] T. K. Y. Okumura, E. Ohmori and K. Fukuda, "Field strength and its variability in vhf and uhf land mobile service," *Review -Electrical Communication Laboratory*, vol. 16, pp. 825–873, September-October 1968.

[8] D. Cox, "Delay-doppler characteristics of multipath propagation at 910Mhz in a suburban mobile radio environment," *IEEE Transactions on Antennas and Propagation*, vol. 20, pp. 625–635, September 1972.

[9] M. Hata, "Code combining – a maximum-likelihood decoding approach for combining an arbitrary number of noisy packets," *IEEE Transactions on Vehicular Technology*, vol. VT-29(3), pp. 317–325, 1980.

[10] D. Cox, "910 Mhz urban mobile radio propagation: Multipath characteristics in new york city," *IEEE Transactions on Communications*, vol. 21, pp. 1188–1194, November 1973.

[11] F. J. MacWilliams and N. J. Sloane, *The Theory of Error-Correcting Code*, North-Holland, 1978.

[12] A. J. Viterbi, *CDMA: Principles of Spread Spectrum Communications*, Addison Wesley, 1995.

[13] J. G. Proakis, *Digital communications*, McGraw-Hill, 1989.

[14] T. C. Nolan and W. E. Stark, "A Recursive Method for Calculating Error Probabilities for a Reed-Solomon Codeword," *Proceedings of the IEEE Vehicular Technology Conference*, 1998.

[15] C. C. Chao and R. J. McEliece, "A Markov chain model for the burst error statistics of viterbi decoding," in *Proceedings 1990 International Symposium on Information Theory and Its Applications*, pp. 391–394, Haiwaii,USA, 1990.

[16] K. Pahlavan and A. H. Levesque, *Wireless Information Networks*, Wiley-Interscience, New York, 1995.

[17] M. B. Pursley and J. M. Shea, "Phase-shift-key modulation for multimedia multicast transmission in mobile wireless networks," in *Proceedings - IEEE Military Communications Conference MILCOM*, volume 1, pp. 210–214, Washington, DC, 1996, IEEE Communications Society.

[18] M. B. Pursley and J. M. Shea, "Convoutionally encoded phase-shift-key modulation for multimedia multicast transmissions in mobile wireless networks," in *Proceedings - IEEE Military Communications Conference MILCOM*, volume 1, pp. 978–982, Montery, CA, 1997, IEEE Communications Society.

[19] D. Chase, "Code combining – a maximum-likelihood decoding approach for combining an arbitrary number of noisy packets," *IEEE Transactions on Communications*, vol. COM-33, no. 5, pp. 385–393, May 1985.

[20] J. Hagenauer, "Rate-compatible punctured convolutional codes (RCPC codes) and their applications," *IEEE Transactions on Communications*, vol. 36, no. 4, pp. 389–400, April 1988.

[21] C. Berrou, A. Glavieux, and P. Thitimajshima, "Near Shannon limit error-correcting coding and decoding: Turbo codes," in *Proceedings of the 1993 IEEE International Conference on Communications*, pp. 1064–1070, May 1993.

[22] K. R. Narayanan and G. L. Stuber, "A novel ARQ technique using the turbo coding principle," *Communications Letters*, vol. 1, pp. 49–51, March 1998.

[23] D. N. Rowitch and L. B. Milstein, "Rate compatible punctured turbo (RCPT) codes in a hybrid FEC/ARQ system," in *Proceedings of the 1997 IEEE Global Telecommunications Mini- Conference*, volume 4, pp. 55–59, Phoenix, AZ, November 1997.

[24] D. Divsalar and F. Pollara, "Turbo codes for pcs applications," in *Proceedings of the 1995 IEEE International Conferences on Communications*, volume 1, pp. 54–59, Seattle, WA, June 1995.

[25] M. Pursley, "Frequency-hop transmission for satellite and terrestrial packet radio networks," *IEEE Transactions on Information Theory*, vol. IT-32, no. 5, pp. 652–667, September 1985.

[26] E. Geraniotis and J. W. Gluck, "Coded FH/SS communications in the presence of combined partial-band noise jamming, Rician nonselective fading, and multiuser interference," *IEEE Journal on Selected Areas in Communications*, vol. SAC-5, no. 2, pp. 194–214, February 1987.

[27] S. Kim and W. E. Stark, "Optimum rate Reed-Solomon codes for frequency-hopped spread-spectrum multiple-access communication systems," *IEEE Transactions on Communications*, vol. 37, no. 2, pp. 138–144, February 1989.

[28] K. Yang and G. L. Stuber, "Throughput analysis of a slotted frequncy-hop mulitple-access network," *IEEE Journal on Selected Areas in Communications*, vol. 8, no. 4, pp. 588–602, May 1990.

[29] P. S. Sindhu, "Retransmission error control with memory," *IEEE Transactions on Communications*, vol. COM-25, no. 5, pp. 473–479, May 1977.

[30] Y. Wang and S. Lin, "Modified selective-repeat type-IIhybrid arq system and its performance analysis," *IEEE Transactions on Communications*, vol. COM-31, no. 5, pp. 593–608, May 1983.

[31] J. J. Metzner and D. Chang, "Efficient selective repeat arq strategies for very noisy and fluctuating channels," *IEEE Transactions on Communications*, vol. COM-33, no. 5, pp. 409–416, May 1985.

[32] S. Lin and P. S. Yu, "Hybrid arq scheme with parity retransmission for error control of satellite channels," *IEEE Transactions on Communications*, vol. COM-30, no. 7, pp. 1701–1719, July 1982.

[33] A. M. Y. Bigloo and T. A. Gulliver, "A slotted frequency-hopped multiple-access network with packet combining," *IEEE Transactions on Communications*, vol. 14, no. 9, pp. 1859–1865, December 1991.

[34] S. Kallel, "Analysis of a type IIhybrid arq scheme with code combining," *IEEE Transactions on Communications*, vol. COM-38, no. 8, pp. 1133–1137, August 1990.

[35] G. D. Forney, Jr., "Convolutional codes i: Algebraic structure," *IEEE Transactions on Information Theory*, vol. IT-16, no. 6, pp. 720–738, November 1970.

[36] V. W. Cheng and W. E. Stark, "Performance of trellis coded direct-sequence spread-spectrum multiple-access with noncoherent reception in a fading environment," in *Proceedings of the IEEE Conference on Personal, Indoor and Mobile Radio Communications*, pp. 1125–1130, October 1996.

[37] A. Viterbi, *CDMA Principles of Spread Spectrum Communications*, Addison–Wesley, Reading, Massachusetts, 1995.

[38] N. Ahmed and K. Rao, *Orthogonal Transforms for Digital Signal Processing*, Springer–Verlag, Berlin, 1975.

[39] H. Harmuth, *Transmission of Information by Orthogonal Functions*, Springer–Verlag, Berlin, second edition, 1972.

[40] M. Maquis, *Applied Walsh Analysis*, Heyden, London, 1981.

[41] K. Henderson, "Some notes on the walsh function," *IEEE Transactions on Electronic Computers*, pp. 50–52, February 1964.

[42] S. Mitra and J. Kaiser, *Handbook for Digital Signal Processing*, Wiley, New York, 1993.